

IMPLANTATION AND ACTIVATION OF ULTRA-SHALLOW BORON IN GERMANIUM

By

BRADLEY R. YATES

A DISSERTATION PRESENTED TO THE GRADUATE SCHOOL
OF THE UNIVERSITY OF FLORIDA IN PARTIAL FULFILLMENT
OF THE REQUIREMENTS FOR THE DEGREE OF
DOCTOR OF PHILOSOPHY

UNIVERSITY OF FLORIDA

2012

© 2012 Bradley R. Yates

To Mom

ACKNOWLEDGMENTS

The culmination of this project is an exciting time for me and many thanks need to be extended for all of the help that I have received along the way. While I am earning the degree from the University of Florida, it seems like the majority of this work was completed at other institutions. I have travelled and sent samples around the world, but this work would not have been completed if it was not for those closest giving me their support.

To begin, I would like to thank my mother, family, and friends for always being there for me during my academic career. The support received was probably not outwardly recognized, but its effect was important nonetheless. I would also like to acknowledge all of the help that my advisor, Dr. Kevin Jones, has given me along the way. Foolishly, I had turned down his initial offer to join his group just to plead with him one year later for admittance. For this, I will always be grateful. I also appreciate all of the help given to me by Dr. Mark Law, Dr. Toshi Nishida, Dr. Gerald Bourne, Dr. Luisa Amelia Dempere and Dr. Rajiv Singh for sitting on my supervisory committee. I also need to thank Dr. John Talbott for his support of my academic endeavors; this will never be forgotten and I will be sure to pay it forward.

I would also like to thank all of the members of the group that have helped me along the way. Everyone from Pat Whiting with his seemingly never-ending supply of academic memes to Nick Rudawski with his imitations of those that shall go unmentioned; every instance of 'gives credence to the notion' in this document was written with Nick in mind. All of my interactions here at the University of Florida have been positive and have been instrumental in achieving this goal.

I would also like to thank the countless collaborators that have helped me with this project. All of the folks at CAPRES have been undoubtedly a large part of this work and cannot go unmentioned; Peter Nielsen, Dirch Petersen, Rong Lin, and Ole Hansen have all assisted with acquiring data as well as writing manuscripts. I would also like to acknowledge Lucia Romano of the University of Catania and Barney Doyle of Sandia National Laboratories for their assistance with ion beam analysis. Alex Kontos of Varian Semiconductor/Applied Materials, Rob Elliman at Australian National University, and Russell Gwilliam of the University of Surrey are also acknowledged for their help with all of the ion implants used for this project. Dr. Ignacio Martin-Bragado and Jose Luis Gomez-Sellis at IMDEA have provided simulations for this work and their efforts are greatly appreciated.

The project would not have been possible without the funding provided by Intel. I also would like to acknowledge the Major Analytical Instrumentation Center and the Nanoscale Research Facility at the University of Florida and the Advanced Materials Processing and Analysis Center at the University of Central Florida for the use of their facilities in completing this work.

TABLE OF CONTENTS

	<u>page</u>
ACKNOWLEDGMENTS.....	4
LIST OF TABLES.....	9
LIST OF FIGURES.....	10
LIST OF ABBREVIATIONS.....	14
ABSTRACT	15
CHAPTER	
1 INTRODUCTION	17
1.1 Technological Motivation	17
1.2 Objective and Statement of Thesis	18
1.3 Background Information.....	18
1.3.1 Ion Implantation, Amorphization and Solid Phase Epitaxial Growth	18
1.3.2 Activation of B in Ge	23
1.3.3 Diffusion of B in Ge.....	29
1.3.4 Activation and Diffusion of B in Si.....	30
1.3.5 Summary	32
2 EXPERIMENTAL TECHNIQUES.....	39
2.1 Materials Processing.....	39
2.1.1 Ion Implantation.....	39
2.1.2 Dicing Saw	40
2.1.3 Thermal Processing.....	40
2.2 Electrical Characterization	43
2.2.1 Four Point Probe	43
2.2.2 Hall Effect.....	44
2.2.3 Micro Hall Effect & Micro Four Point Probe	47
2.3 Structural Characterization	49
2.3.1 Transmission Electron Microscopy	49
2.3.1.1 TEM Sample Preparation	51
2.3.2 Secondary Ion Mass Spectrometry.....	53
2.3.3 Rutherford Backscattering Spectrometry	55
2.3.4 Nuclear Reaction Analysis.....	56
2.3.5 Elastic Recoil Detection.....	57
2.4 Summary	58
3 ACTIVATION OF ULTRA-SHALLOW BORON IMPLANTS IN GERMANIUM	71

3.1	Activation of B ⁺ Implants in Ge	71
3.2	Experimental Details	73
3.3	Characterization of Residual Implanted Dose	75
3.4	Hall Effect Characterization	76
3.5	Nuclear Reaction and Channeling Analyses	79
3.6	Summary	81
4	EFFECT OF IMPLANT ENERGY ON B ACTIVATION	89
4.1	Low Energy B ⁺ Implantation in Ge	89
4.2	Experimental Details	89
4.3	Effect of Increased B ⁺ Implant Energy	90
4.4	Role of Implant Energy	93
4.5	Summary	97
5	THERMAL STABILITY OF BORON ACTIVATION IN GERMANIUM	106
5.1	Activation Stability of B in Ge	106
5.2	Experimental Details	107
5.3	Isothermal Annealing	108
5.4	Activation Thermal Stability Between 400-600°C	112
5.5	High Temperature Anneals	116
5.5.1	B Concentration Profile Following High T Annealing	117
5.5.2	Reduction of Active Carriers Following High T Annealing	119
5.5.3	Significance of the Lack of B Diffusion	119
5.6	Theory for B Inactivity	121
5.7	Simulation of Activation Behavior	126
5.8	Summary	128
6	IMPLANT-RELATED DAMAGE IN GE	147
6.1	Introduction	147
6.2	Experimental Details	149
6.3	Projected Range Damage	150
6.4	End of Range Damage	153
6.5	Discussion	154
6.6	Summary	155
7	CONCLUSIONS AND FUTURE WORK	164
	APPENDIX: EFFECT OF IMPLANT CONDITIONS ON B ACTIVATION	168
A.1	Variable Implantation Conditions	168
A.2	Experimental Methods	168
A.3	Results and Discussion	169
A.4	Summary	171
	LIST OF REFERENCES	176

BIOGRAPHICAL SKETCH.....	188
--------------------------	-----

LIST OF TABLES

<u>Table</u>	<u>page</u>
3-1 Channeling yields and corresponding substitutional B fractions as measured by channeling analysis using nuclear reactions along three axes ($\langle 100 \rangle$, $\langle 110 \rangle$, and $\langle 111 \rangle$) and Hall effect measurements after annealing 400°C for 60s.....	83
5-1 Inactive B determined from micro Hall effect and the corresponding displaced Ge obtained from RBS characterization for c-Ge samples annealed for various times.	130

LIST OF FIGURES

<u>Figure</u>	<u>page</u>
1-1 Schematic of the ion-solid interactions during ion implantation.	34
1-2 Evidence of the channeling tail in c-Ge..	35
1-3 Schematic displaying the amorphization process in Ge.	36
1-4 Evidence of transient B diffusion in Ge.....	37
1-5 Typical B concentration profile following transient enhanced diffusion in Si.	38
2-1 Schematic of four point probe configuration used to determine sheet resistance, R_S	60
2-2 Sample geometry for a four point probe measurement	60
2-3 Illustration of the electrons passing through a solid in the presence of a magnetic field.	61
2-4 Schematic of the van der Pauw contact scheme	61
2-5 Illustration of the contact scheme typically used for Hall effect measurements.	62
2-6 Leakage current into the n-type substrate can dominate a measurement if the metallurgical junction is not sufficient.	62
2-7 Decreased horizontal length scale of measurement probes reduces the junction leakage.....	63
2-8 Current paths near contacts for M4PP measurements under the influence of a magnetic field.	64
2-9 The presence of a cleaved boundary gives rise to a resistance difference, $\Delta R_{BB'}$, between B and B' during micro Hall effect measurements.....	65
2-10 Schematic diagram of a TEM.	66
2-11 Representation of typical damage layer produced by FIB milling	67
2-12 Typical data produced from c-RBS experiment.	68
2-13 Illustration of a nuclear reaction between a proton and a B atom as it produces an α -particle	69

2-14	Representation of α particle counts produced by analyzing B atoms in different confirmations	69
2-15	Experimental setup of an ERD experiment.....	70
3-1	The effect of B ⁺ backscattering for implantation into Ge and Si.	84
3-2	Percent of B ions backscattered as a function of implant energy.	85
3-3	Electrical characteristics as a function of B ⁺ fluence implanted at 2 keV into crystalline and preamorphized Ge, respectively, after annealing at 400°C for 1h.	86
3-4	HR-XTEM micrographs of a crystalline Ge sample B ⁺ implanted at 2 keV to $5.0 \times 10^{15} \text{ cm}^{-2}$ as-implanted in c-Ge	87
3-5	B concentration profiles of a pre-amorphized Ge sample B ⁺ -implanted at 2 keV to doses of 5.0×10^{13} or $5.0 \times 10^{15} \text{ cm}^{-2}$ as-implanted (dashed line) and after annealing at 400 °C for 1 h (solid line) as measured using SIMS.	88
4-1	SRIM simulations depicting the shift in the B concentration profile produced with increasing implant energy. ⁷⁸	99
4-2	Measured sheet resistance of samples B ⁺ implanted at 2, 4, and 6 keV to fluences ranging from 5.0×10^{13} to $5.0 \times 10^{15} \text{ cm}^{-2}$ after annealing 400°C 60s....	100
4-3	Measured sheet number of samples B ⁺ implanted at 2, 4, and 6 keV to fluences ranging from 5.0×10^{13} to $5.0 \times 10^{15} \text{ cm}^{-2}$ after annealing 400°C 60s....	101
4-4	Measured drift mobility of samples B ⁺ implanted at 2, 4, and 6 keV to fluences ranging from 5.0×10^{13} to $5.0 \times 10^{15} \text{ cm}^{-2}$ after annealing 400°C 60s....	103
4-5	Measured percentage of electrically active B at variable implant energies. A 35 keV implant corresponds to an R_p of 90 nm	103
4-6	Measured percentage of electrically active B in Si at variable implant energies.....	104
4-7	Vacancies created per incoming B ion as a function of implant energy as simulated by SRIM. ⁷⁸	105
5-1	Sheet resistance data obtained for samples implanted at 2 keV with a fluence of $1.0 \times 10^{15} \text{ cm}^{-2}$ and subsequently annealed at 400°C for various times	131
5-2	Sheet resistance line scan acquired across c-Ge sample annealed at 400°C for 30s.	132
5-3	Sheet number data obtained for samples implanted at 2 keV with a fluence of $1.0 \times 10^{15} \text{ cm}^{-2}$ and subsequently annealed at 400°C for various times	133

5-4	Drift mobility for a c-Ge samples implanted at 2 keV with a fluence of $1.0 \times 10^{15} \text{ cm}^{-2}$ and subsequently annealed at 400°C for various times.	134
5-5	RBS channeling spectra for c-Ge samples implanted at 2 keV to a fluence of $1.0 \times 10^{15} \text{ cm}^{-2}$ and subsequently annealed at 400°C for various times	135
5-6	Sheet resistance data obtained for samples implanted at 2 keV with fluences ranging from 5.0×10^{13} to $5.0 \times 10^{15} \text{ cm}^{-2}$ and subsequent annealing at 400°C and 600°C for 60s.....	136
5-7	Change in sheet resistance for 2, 4, and 6 keV B ⁺ implants to fluences ranging from 5.0×10^{13} to $5.0 \times 10^{15} \text{ cm}^{-2}$ between annealing at 400°C and 600°C for 60s.....	137
5-8	Electrical activation characteristics as a function of anneal temperature for samples B ⁺ implanted at 2, 4, and 6 keV to a fluence of $5.0 \times 10^{15} \text{ cm}^{-2}$ into c-Ge and PA-Ge.	138
5-9	HR-XTEM images of samples B ⁺ implanted at 2 keV to a fluence of $5.0 \times 10^{15} \text{ cm}^{-2}$ into c-Ge after annealing for 60s at 400°C A) at 500°C B) at 600°C C) and D) into PA-Ge after annealing for 60s at 400°C	139
5-10	Sheet resistance for samples B ⁺ implanted at 6 keV to a fluence of $5.0 \times 10^{15} \text{ cm}^{-2}$ into c-Ge and PA-Ge.	140
5-11	Sheet number for samples implanted at 6 keV to a fluence of $5.0 \times 10^{15} \text{ cm}^{-2}$...	140
5-12	B concentration profiles for samples B ⁺ implanted at 6 keV to a fluence of $5.0 \times 10^{15} \text{ cm}^{-2}$ into c-Ge as-implanted, annealed at 650°C for 10s, and annealed 800°C for 10s.	141
5-13	B concentration profiles for samples B ⁺ implanted at 6 keV to a fluence of $5.0 \times 10^{15} \text{ cm}^{-2}$ into PA-Ge as-implanted, annealed at 650°C for 10s, and annealed 800°C for 10s.	141
5-14	HR-XTEM micrograph of a pit formed in Ge following thermal processing. The presence of the native oxide surrounding the pit is evident.	142
5-15	SIMS characterization of a sample B ⁺ implanted at 35 keV to a fluence of $2.0 \times 10^{15} \text{ cm}^{-2}$ following various thermal treatments. The horizontal shift in the chemical profile of the uncapped sample annealed at 600°C is evident.	143
5-16	Simulation displaying the cumulative vacancy population as a function of radial distance from an implanted B ion at 2 keV.....	144
5-17	Kinetic Monte Carlo simulations displaying the substitutional and interstitial boron concentrations following annealing at 400°C for 60s for a 2 keV B ⁺ implant.....	145

5-18	Kinetic Monte Carlo simulations displaying the substitutional and interstitial boron concentrations following B ⁺ implantation at 2 keV to a fluence of $5.0 \times 10^{13} \text{ cm}^{-2}$ and annealing at 400°C	146
6-1	Bright field XTEM image taken with $g_{220}(3g)$ diffraction condition of projected range damage created by a 2 keV B ⁺ implant to a fluence of $1.0 \times 10^{15} \text{ cm}^{-2}$ following annealing at 500°C for 2 h times ranging from 2 to 36h.....	157
6-2	HR-XTEM image of projected range damage created by a 2 keV B ⁺ implant to a fluence of $1.0 \times 10^{15} \text{ cm}^{-2}$ following annealing at 500°C for 24 h.....	158
6-3	Defect orientations of projected range damage in Ge.	159
6-4	XTEM images of projected range damage created by a 2 keV B ⁺ implant to a fluence of $1.0 \times 10^{15} \text{ cm}^{-2}$ following annealing at 500°C.....	160
6-5	Bright field PTEM images taken with $g_{220}(3g)$ diffraction condition of projected range damage created by a 2 keV B ⁺ implant to a fluence of $1.0 \times 10^{15} \text{ cm}^{-2}$ following annealing at 500°C for 2 h and 12 h.	161
6-6	XTEM images taken with $g_{220}(3g)$ diffraction condition of EOR damage created by a 1 MeV Ge ⁺ implant to a fluence of $2.0 \times 10^{15} \text{ cm}^{-2}$ following annealing at 330°C for various times.	162
6-7	EOR damage created by a 1 MeV Ge ⁺ implant to a fluence of $2.0 \times 10^{15} \text{ cm}^{-2}$ as a function of annealing time at 330°C.	163
A-1	Measured sheet resistance (R_s) after annealing at 400 °C for 60 s as a function of beam current.....	172
A-2	Measured sheet number (n_s) and percent electrical activation as a function of beam current implanted at 2 keV to a fluence of $5.0 \times 10^{14} \text{ cm}^{-2}$ into crystalline Ge after annealing at 400 °C for 60s.	173
A-3	Measured drift mobility (μ_D) as a function of beam current implanted at 2 keV to a fluence of $5.0 \times 10^{14} \text{ cm}^{-2}$ into crystalline Ge after annealing at 400 °C for 60s.....	174
A-4	HR-XTEM micrograph of an as-implanted crystalline Ge sample B ⁺ implanted at 2 keV to $5.0 \times 10^{14} \text{ cm}^{-2}$ at a beam current of 6.4 mA.....	175

LIST OF ABBREVIATIONS

4PP	Four point probe
α -Ge	Amorphous Ge
c-Ge	Crystalline Ge
CMOS	Complementary metal oxide semiconductor
ERD	Elastic recoil detection
FIB	Focused ion beam
HR-XTEM	High-resolution transmission electron microscopy
IBA	Ion beam analysis
M4PP	Micro four point probe
MHE	Micro Hall effect
NRA	Nuclear reaction analysis
n_s	Sheet number
PA-Ge	Preamorphized Ge
q	Elementary charge, 1.602×10^{-19} C
RBS	Rutherford backscattering
R_p	Projected range
R_s	Sheet resistance
TEM	Transmission electron microscopy
SIMS	Secondary ion mass spectrometry
SPEG	Solid phase epitaxial growth
SRIM	Stopping range of ions in matter
μ_D	Drift mobility
V_H	Hall voltage

Abstract of Dissertation Presented to the Graduate School
of the University of Florida in Partial Fulfillment of the
Requirements for the Degree of Doctor of Philosophy

IMPLANTATION AND ACTIVATION OF ULTRA-SHALLOW BORON IN GERMANIUM

By

Bradley R. Yates

December 2012

Chair: Kevin S. Jones

Cochair: Mark E. Law

Major: Materials Science and Engineering

The physical scaling associated with integrated circuits is exhausting the properties of Si and requires that advanced materials be used for future device generations. Ge is widely regarded as a possible replacement for Si due to its enhanced mobility and reduced contact resistance. Due to the extensive use of $\text{Si}_x\text{Ge}_{1-x}$ in current devices, the implementation of Ge into future devices could be considered a mere evolution from Si rather than a revolutionary change. However, the information regarding technologically relevant ultra-shallow dopant implants into Ge and their associated activation behavior is currently sparse and must be fully understood prior to implementation into future devices.

The activation behavior of ultra-shallow B^+ implants in Ge has been investigated using micro Hall effect and micro four point probe techniques. It has been observed that the activation behavior of ultra-shallow B^+ implants are anomalous in that the electrically active dopant fraction is independent of the implanted B^+ fluence for both crystalline and pre-amorphized Ge. Ion beam analysis techniques have been employed which have confirmed that a small fraction of B is located substitutionally and the substitutional fraction does not increase appreciably with thermal processing for

temperatures $\leq 600^{\circ}\text{C}$. Activation is observed to increase with increasing B^+ energy which is attributed to the effect of the surface proximity and its associated effect on vacancy annihilation.

The activation behavior is further explained through the largely immobile B atoms which have a distinctly low probability of recombining with a vacant site due to the overwhelmingly large population of interstitials created during implantation as simulated by SRIM. The excess interstitial population increases competition for B recombination on a vacant lattice site and thereby reduces B activation. B^+ implantation at increased energy increases the number of vacancies created and reduces the effect of the surface on vacancy annihilation which explains the observed increase in activation.

The observed activation behavior in this work is a strong departure from what has been observed previously for B in Si. The results suggests that previous activation and dopant solubility models implemented for activation in Si do not apply for shallow B^+ implantation in Ge.

CHAPTER 1 INTRODUCTION

1.1 Technological Motivation

The semiconductor industry has evolved tremendously over the preceding half century. One of the industry pioneers, Gordon Moore, originally claimed that the number of components in an integrated circuit will double every year, but has since been taken to mean a doubling every 1.5-2 years and is known as Moore's Law.¹ In an attempt to maintain the pace dictated by Moore's Law, the semiconductor industry is faced with physically scaling down the size of components built on integrated circuits. However, silicon, whose natural abundance and stable native oxide has propelled it as the traditional workhorse of the semiconductor industry, is reaching its physical scaling limits. To continue the scaling, the industry has recently chosen to shift away from planar processing towards three-dimensional device structures. However, the need for advanced semiconducting materials for future device generations still looms on the horizon.

Germanium is regarded as one of the possible replacement materials for Si in future device generations due to its enhanced electron and hole mobility in comparison to Si.² Ge was studied extensively several decades ago and the first transistor was actually constructed from Ge. The recent implementation of high- κ gate dielectric has circumvented the issues regarding the unstable native oxide of Ge.

In order for Ge to be realized as a replacement for Si in future generation devices, further fundamental understanding of the activation behavior of B must be realized. At present, there is a significant dearth of information available regarding technologically relevant ultra-shallow B⁺ implants in Ge. The few reports available only

mention a single implant or anneal condition with little analysis of the general activation behavior.

1.2 Objective and Statement of Thesis

There is significant technological motivation to understand the electrical activation behavior of ultra-shallow B⁺ implants in Ge. The research discussed in this document seeks to understand the electrical characteristics of implanted B in Ge as well as the effects the ion implantation process has on the substrate. The following aspects will be given significant attention. The activation behavior of ultra-shallow ion implanted behavior will be investigated using micro Hall effect and micro four point probe techniques. Ion beam analysis will be used to provide further evidence of activation results. The thermal stability of B activation in Ge will be investigated for a wide range of annealing times and temperatures. The formation and evolution of implant-related damage and its effect on activation will also be investigated.

1.3 Background Information

1.3.1 Ion Implantation, Amorphization and Solid Phase Epitaxial Growth

Ion implantation involves the use of an accelerated beam of charged particles directed towards a solid in order to effect change on the surface properties of the material. It has been used extensively by the semiconductor industry for several decades in order to alter the electrical properties of the material by altering the chemical composition of the near-surface regions. It is the preferred method for introducing high concentrations of dopant atoms in precise locations. A substantial benefit of ion implantation is its ability to self-align the placement of the dopant. For example, implantation over a masked substrate will not allow for incorporation of dopant below the masked region while implanting dopant where the surface is bare. Its self-aligning

capabilities enable the accurate and highly repeatable control of dopant profiles which have proven invaluable for the processing of semiconductor devices.³⁻⁶

During ion implantation, a gaseous source of the intended dopant is ionized, accelerated and mass-separated based on its mass to charge ratio. The ionization process will create a series of ions with the same atomic mass, but with varying charge based on the number of electrons removed. The desired ion charge is typically chosen based on the fraction of the total beam to create the highest number of ions per second or in simpler terms, beam current. Once the desired charge is separated from the beam, it is steered towards the substrate where it eventually comes to rest or is implanted in the target.

The dopant of mass, m , is ionized to obtain a charge, q , and is accelerated by a potential difference, V . The accelerating voltage can vary from a few eV to several hundred MeV, but is typically near the 1-100 keV range for typical semiconductor applications. The accelerating voltage imparts kinetic energy and dictates the ion velocity using the classical mechanics equation:

$$\frac{1}{2}mv_{ion}^2 = qV_{acc} = E_{kin} \quad (1-1)$$

Once the accelerated ion impacts the surface, a series of ion-solid interactions is set in motion. As the ion reaches the target surface, it is likely that the ion will displace target atoms through sputtering or the accelerated ion may be rejected from the solid through backscattering. For sputtering, the fraction of ions sputtered increases increasing ion mass or namely the ratio of atomic mass of the ion and the target; the opposite is true for ion backscattering. Once the ion enters the solid, the ion slows through a combination of electronic (elastic) and nuclear (inelastic) scattering

processes. Near the surface, the ion slows primarily through electronic interactions between the charge associated with the ion and the electronic clouds of target atoms. As the ion travels further in to the solid, it is continually slowed by electronic means and begins to lose a larger fraction of its kinetic energy through nuclear collisions. Electronic stopping is dominant for ion travel near the surface where the ion is generally slowed while nuclear stopping begins to dominate as the ion travels deeper into the solid as the ions are travelling at a slower velocity. The probability of nuclear scattering increases as the energy and velocity of the incoming ion is decreased. Due to this, nuclear stopping dominates near the end of the ion range while electronic stopping is more prominent near the surface; however, both mechanisms are active throughout the entire ion range. The energy lost to the ion-solid interactions are described by:

$$-\frac{dE}{dx} = N(S_n(E) + S_e(E)) \quad (1-2)$$

where dE/dx is the energy lost through the depth of the sample, S_n is the nuclear stopping power, S_e is the electronic stopping power, and N is the number of atoms in the solid per unit volume.

Both elastic and inelastic scattering mechanisms are important for loss of ion energy, but nuclear collisions are the primary source of ion stopping and radiation damage to the lattice. The displaced target atoms, or knock-on atoms, have kinetic energy which is subsequently lost through nuclear collisions with other host atoms. This pyramid process is known as a cascade and creates a number of vacancy and interstitial (Frenkel) pairs in the target material. Once all kinetic energy is lost by electronic and nuclear means, the ion becomes implanted in the target. A schematic representation of the ion-solid interaction is shown in Figure 1-1.

The implanted ion comes to rest in the solid at a controllable depth for a given set of implantation conditions. The total distance travelled through the solid is called the ion range, R , while the perpendicular distance travelled from the surface is termed the projected range, R_p . These definitions hold true for single ions; however, an implanted fluence for semiconductor applications, to a rough approximation, is typically over 5.0×10^{12} ions. The implantation process is largely statistical in which two identical ions implanted at identical conditions into the same substrate can have radically different paths through the target. For given conditions, the average projected range of an implanted dose creates a Gaussian distribution of dopants with respect to depth in the sample. The peak of the profile is the average R_p for a given set of implant conditions.

A side effect of the ion implantation process is the introduction of implant-related damage to the material. The point defects created during the implantation process have been shown to have deleterious effects on dopant activation, dopant diffusion, and device leakage.⁷⁻¹⁵ For a low fluence, isolated point defects may form in the crystal lattice. Upon annealing these point defects may coalesce to form extended defects which are referred to as sub-amorphization defects or the occurrence of defects when ion implantation damage is insufficient to create an amorphous layer.¹⁶

As the ion fluence is increased, a proportionally larger amount of Frenkel pairs are created and damaged regions may coalesce. The damage accumulation is assumed to be linear with implanted fluence until a certain value is obtained. A critical threshold of damage imparted to the crystalline lattice exists which upon reaching, the crystal relaxes to an amorphous state which renders the lattice devoid of any long-range order. The transition to an amorphous solid is deemed a first order phase transition.¹⁷

The critical fluence required for amorphization is deemed the amorphization threshold and varies for different ion species. The amorphization process is directly dependent on the creation of point defects and therefore dependent on ion mass and energy, ion beam current, implant angle, substrate temperature, etc., where heavier ions create denser damage cascades and the amorphization occurs at a reduced fluence.^{18,19} The amorphization threshold can be determined by alternate means, namely through the accumulation of vacancies created during the implantation process called the threshold damage density. In doing so, the amorphization threshold can be described in terms of damage created to allow for better prediction of the amorphous layer depth independent of the implanted species.²⁰

The formation of an amorphous layer has been shown to be advantageous for semiconductor processing. The amorphization of the semiconductor prior to dopant implantation, or preamorphization, has several advantages over dopant implantation alone following a subsequent annealing step. Following annealing, preamorphization enables increased dopant activation, a reduction of implant damage, and shallower dopant concentration profiles. Self-implants allow for amorphization with a reduced implant fluence which decreases implantation time and are typically used prior to the dopant implant. The amorphization threshold for Ge has been well-studied and occurs at a fluence of approximately $5.0 \times 10^{13} \text{ cm}^{-2}$ for a 120 keV Ge⁺ implant at room temperature.^{20,21} This amorphization threshold corresponds to a threshold damage density of approximately $3.0 \times 10^{20} \text{ keV/cm}^3$.²²

In addition, amorphization allows for shallower dopant profiles in comparison to implants into crystalline substrates. When crystalline substrates are irradiated, ions

have a tendency to channel down open crystallographic axes. These pathways allow for deeper penetration into the solid than the same implant into a randomly ordered or amorphous solid. In doing so, a channeling tail is created which effectively increases the dopant depth into the solid. The channeling tail is evident in a plot of a B implant into crystalline and preamorphized Ge as shown in Figure 1-2.

During annealing, the amorphous layer regrows from the crystalline seed below through a process called solid phase epitaxial growth (SPEG) Figure 1-3 displays a schematic of the introduction of an amorphous Ge (α -Ge) layer and the subsequent regrowth of that layer from the crystalline (001) Ge below. During this process, an increased fraction of dopant atoms are incorporated into substitutional sites rendering them electrically active. The SPEG process allows for approximately an order of magnitude increase in electrical activation in Ge.^{23,24} During regrowth, the SPEG process allows for a reduction of point defects upon regrowth due to the direct rearrangement of bonds as the crystalline interface advances through the amorphous layer; however, the region just beyond the amorphous-crystalline interface is highly damaged and is often the source of point defects responsible for extended defect formation known End of Range (EOR) damage. The EOR defects are denoted as being defects that occur when implantation damage is sufficient to produce an amorphous layer.¹⁶

1.3.2 Activation of B in Ge

Germanium is a rather resistive material with intrinsic Ge having a resistivity on the order of 50 Ω -cm.²⁵ However, the introduction of a minute concentration of dopant atoms can alter the resistivity of the material drastically by several orders of magnitude. Herein lies the beauty of semiconducting materials. However, the mere presence of

dopant atoms in the lattice is sufficient to effect change to the electrical properties of the material. For a dopant to be electrically active in Ge, it must be located on a substitutional lattice site. The process of finding a lattice site is typically completed by pairing with a vacant lattice site or replacing an interstitial from its site through a kick-out mechanism. Once situated on a substitutional site, the B atom has acts as an acceptor in which it accepts an electron from the Ge crystal to complete the fourth of its covalent bonds to the lattice and binds a hole which can be ionized to aid in conduction of the lattice. A semiconductor that is doped with an impurity that acts an acceptor is considered to be p-type.

By increasing the number of B atoms situated on substitutional sites, the conductivity of the crystal is affected positively. The conductivity, σ , of a material is defined by:

$$\sigma = qp\mu_h + qn\mu_e \quad (1-3)$$

where q is the fundamental charge, p and n are the concentrations of holes and electrons, and μ_h and μ_e are the hole and electron mobilities, respectively. For B implantation in Ge, the acceptor concentration far outweighs any intrinsic electron contribution. The conductivity then becomes:

$$\sigma = qp\mu_h \quad (1-4)$$

Upon first inspection of this equation, it appears that by increasing the concentration of active dopants, the conductivity of the material will decrease. To a first approximation, this is true; however, there is a finite limit on the number of B atoms that can be incorporated in solution with Ge.^{26,27} The maximum chemical solubility of B in Ge is reported to be approximately $5.5 \times 10^{18} \text{ cm}^{-3}$ as determined from diffusion experiments.²⁸⁻

³⁰ From these experiments, it has been shown that B atoms in Ge are relatively immobile for all practical thermal treatments. For example, Uppal *et al.* implanted B⁺ at 20 keV to a fluence of $6.0 \times 10^{14} \text{ cm}^{-2}$ and annealed for 3 h in the range of 675-800°C following which no significant diffusion was observed.³⁰

Despite the low solubility of B in Ge, the ion implantation process often allows for an active concentration of carriers above the reported solubility limit.^{23,31} In effect, the non-equilibrium ion implantation process introduces a metastable increase in the solubility of B atoms.

The activation of B in Ge following ion implantation was studied several decades ago and has just recently regained interest due to Si reaching its physical scaling limits. For low fluence implants implanted to a high energy, it has been shown that a large fraction of implanted B ions are substitutional and active immediately following implantation and prior to any annealing step.^{32,33}

Recently, the investigations into the activation of high fluence B⁺ implants in Ge have been underway.^{23,31} Specifically, several authors have shown that preamorphization allows for an increased fraction of the implanted dopant as compared to dopant implants alone. In some cases, electrical solubility was reported to concentrations as high as $5.5 \times 10^{20} \text{ cm}^{-3}$ and additional authors have reported similar values.^{24,31,34,35} It was observed that the preamorphization energy and subsequent depth of the resulting amorphous layer has an effect on activation where a shallow amorphous layer allowed for dynamic annealing during B⁺ implantation.³⁵ Dynamic annealing occurs when B ions traverse the amorphous crystalline interface and allows for regrowth of the amorphous layer during dopant implantation. To prevent dynamic

annealing, the preamorphization implant must be sufficiently deep to not allow for a significant fraction of B ions to interact with the amorphous crystalline interface.

However, the maximum active concentration allowed by B⁺ implantation in crystalline Ge without a preamorphization step is not as well documented. The electrical solubility for B⁺ implants into c-Ge vary by approximately an order of magnitude. Satta *et al.*³⁴ has determined the maximum activation to be $1.2 \times 10^{19} \text{ cm}^{-3}$ while other authors have reported values in excess of $1.0 \times 10^{20} \text{ cm}^{-3}$.^{24,36} It has been speculated that that electrical solubility of B⁺ implants in Ge is directly related to the damage imparted into the crystal lattice during the implantation process.²³ For 35 keV B⁺ implants, it has been shown that increasing the fluence to $2.8 \times 10^{16} \text{ cm}^{-2}$ yields similar activation values as produced by using a preamorphizing implant. Conversely, implanting B⁺ at liquid nitrogen temperature reduces the dynamic annealing and subsequently increases the damage production which enables similar activation values as preamorphized Ge for reduced fluences.²³ It has been elucidated that sub-microscopic amorphous pockets form with increasing B⁺ fluence which increase the activation upon annealing.^{23,24,37} The wide range of reported electrical solubilities of B⁺ implants into c-Ge raises questions on whether electrical solubility arguments used for activation in Si apply, as the literature does not suggest a single solubility value for Ge.

There have been reports of the formation of a B-Ge cluster which renders implanted B atoms inactive.^{34,37-39} These reports were observed in crystalline Ge only and not when a preamorphization implant is used. The inactive cluster has been shown to affect approximately 50% of the implanted fluence.³⁷ The inactive complex was studied by Impellizzeri *et al.* with Rutherford backscattering spectrometry to determine

the ratio of the number of displaced Ge atoms to the inactive B atoms. From this investigation, it was determined that the B-Ge cluster has the stoichiometry of 8:1 (Ge:B).³⁷ Bisognin *et al.* investigated the same sample set with high-resolution X-ray diffraction and determined that each inactive B atom has a positive volume expansion of $14.8 \pm 1.7 \text{ \AA}^3$ which they conclude is due to the formation of a B-Ge cluster with a stoichiometry of 8:1.³⁹

A few studies have investigated the thermal stability of B activation in Ge and have found that the activation shows little change with additional annealing.^{23,34,40} Bruno *et al.* investigated the change in sheet resistance for samples implanted at 35 keV to various fluences as a function of annealing temperature between 400 and 600°C. A slight decrease in sheet resistance was reported for c-Ge while a slight increase was observed for PA-Ge samples.²³ Although fewer data points were presented, similar behavior was reported by other authors.^{34,40} For all reports regarding the thermal stability of B implants in Ge, no anomalous activation behavior was discussed and activation was reported as being remarkably stable across the investigated annealing range.

Electrical data for samples annealed at high temperature (>600°C) is not available in great quantities which is likely due to the surface desorption of the native Ge oxide.⁴¹ Satta *et al.* studied the sheet resistance of both P and B implants in Ge following flash lamp annealing. Results showed little change in activation with flash lamp annealing for 20 ms at high temperature as opposed to an anneal at 500°C for 1h.⁴² The lack of sheet resistance variation observed could be attributed to the short time spent at high temperature.

It has been reported that the activation of high energy B⁺ implants in Ge exhibits full activation if implanted to a concentration below the electrical solubility and subjected to an anneal at 360°C for 1h.³¹ If the concentration of implanted B exceeds the electrical solubility, the dopants are rendered electrically inactive.³¹ Experiments investigating the thermal stability of B activation have shown that the activation is remarkably stable showing very little change with annealing for temperatures up to 550°C for 1h.²³

However, there is a significant lack of information regarding the activation of ultra-shallow B⁺ implants in Ge. Satta *et al.* reported values for sheet resistance for 6 keV B implants in Ge. From these values, the electrical solubility was determined to be $1.2 \times 10^{19} / \text{cm}^3$ and $2.4 \times 10^{20} / \text{cm}^3$ for crystalline and preamorphized Ge, respectively.³⁴ However, these values were obtained by measuring sheet resistance and not directly measuring the active concentration.^{43,44} Other reports encompass only a few data points and follow a similar procedure.^{40,45} To accurately characterize the activation behavior, the carrier density and drift mobility should be measured directly using the Hall effect.

However, prior to this work, only two reports have investigated the activation following B implantation in Ge using the Hall effect. Hellings *et al.* implanted B⁺ to a fluence of $8.0 \times 10^{14} / \text{cm}^2$ at 2.4 keV into preamorphized Ge and determined that nearly 75% of the dopant was rendered active upon annealing for 5 min at 550°C.⁴⁶ However, this was a systematic study of ultra-shallow junction formation and no other B activation values were provided. Bennett *et al.* used a single 500 eV B⁺ implant to a fluence of

$1.0 \times 10^{15} / \text{cm}^2$ into PA-Ge and determined the maximum solubility to be $2.0 \times 10^{20} / \text{cm}^3$ using a differential Hall effect technique.⁴⁷

It is clear that further information regarding the activation of ultra-shallow B⁺ implants in Ge is sparse at this present time. The available literature on this subject is sparse which creates discrepancies when comparing results from different experiments. The literature presently available does not allow for a comprehensive understanding of B activation in Ge.

1.3.3 Diffusion of B in Ge

It has been established that B diffuses through an interstitial mediated mechanism in Ge. The high formation energy of an interstitial in Ge limits the ability for B to diffuse. It is well-established that B does not appreciably diffuse under typical processing conditions.^{28–30,34,35} However, recent reports have given evidence that excess interstitial populations may spur B diffusion to lengths greater than those observed under equilibrium conditions.

It has been reported by Napolitani *et al.* that a transient diffusion component exists for B following implantation. Figure 1-4 displays the transient B diffusion behavior observed. In this work, a Ge⁺ implant was used to create a band of damage in close proximity to a B-doped layer. Following annealing, it was evidenced that the B-doped layer exhibited a diffusion behavior which slowed with increasing annealing temperature. The decreased diffusion was attributed to the removal of implant damage with increasing annealing temperature.⁴⁸ This behavior is similar to, but with a much smaller magnitude of the well-researched transient enhanced diffusion behavior of B in Si which will be discussed in the following section.

In addition, there have been other reports of abnormal diffusion of B in Ge; however, these were observed under extreme conditions such as during proton irradiation^{49–52}, diffusion through thick amorphous Ge layers⁵³, or following oxygen precipitation after implantation.⁵⁴ While these reports provide insight to the interstitial-mediated mechanism of B diffusion in Ge, they are not directly relevant to conventional integrated circuit processing. Fortunately, under typical processing conditions, it is well-agreed that diffusion is not a concern for B⁺ implants in Ge.^{28,34,35}

1.3.4 Activation and Diffusion of B in Si

In silicon, the most common p-type dopant is boron due to its high dopant solubility.⁵⁵ As such, the activation and diffusion properties of ion implanted B in Si have been studied extensively over the last several decades.⁵⁶ Similar to what has been reported previously for B⁺ implants in Ge, activation in Si has been approached by invoking an electrical solubility limit above which dopants are inactive. However, the behavior of B in Si is dominated by the dopant interaction with point defects present in the crystal through the ion implantation process.

Following implantation, damage to the crystalline lattice can vary from excess point defects to the complete amorphization of the surface region depending on the implant conditions. Upon annealing, these excess point defects strongly affect the activation and diffusion of B in Si. In the case of non-amorphizing implants, excess interstitials coalesce to form defects near the projected range. In the case of amorphizing implants, the region just beyond the amorphous-crystalline interface is heavily defective as it should be assumed to be just below the damage level required to transition to the amorphous state which spurs the formation of extended defects.

The activation of B in Si is largely influenced by interactions with excess interstitials present in the lattice.⁵⁷ Upon defect dissolution, a wave of excess interstitials migrates through the crystal where they interact with B atoms to form electrically inactive B-interstitial complexes commonly referred to as BICs.^{58–60} The formation of BICs can restrict the activation of B in Si to a level well below the solubility.^{58,61,62} B activation in Si undergoes a ‘reverse annealing’ phenomenon where the sheet resistance of the sample which upon annealing, increases before decreasing towards a reduced value.^{13,63} The increase in sheet resistance is attributed to cluster formation while the reduction is due to cluster dissolution and an increase in B solubility with increasing temperature.

Similar to the activation behavior of B in Si, diffusion is also influenced by dopant-defect interactions. It has been widely observed that during annealing, implanted B exhibits diffusion is typically much faster than what is predicted by equilibrium diffusion models.^{64–66} It has also been observed that this diffusivity enhancement decreases with annealing time and hence is called transient enhanced diffusion or TED.^{7,8,57,64,65,67}

Figure 1-5 displays the enhanced diffusion of a B-doped layer following an Si implant at 40 keV to a fluence of $1.0 \times 10^{15} / \text{cm}^2$ and annealing at 810°C for 15 min as adapted from Stolk *et al.*⁶⁸ This amorphizing implant created a band of highly defective band of Si that is rich in excess interstitials. The observed observed diffusion is typical for TED in Si and is much more significant than that observed in Ge.

The enhanced diffusion has been shown to be due to interstitials released from extended defect dissolution kicking out B and allowing it to diffuse through the lattice. TED has also been observed in the absence of extended defects.⁶⁹ The transient

nature of the enhanced diffusion is created by the reduction of excess interstitials available during the annealing process.⁷⁰ Several techniques have been adapted to reduce the excess interstitial concentration in Si as well as its effects on activation and diffusion. The use of co-implantation with C or F to sequester interstitials through a so-called point defect engineering mechanism has been successful in reducing TED.^{71–73} In addition, vacancy engineering involves a high energy (a few MeV) implant to introduce an excess concentration of vacancies near the surface with excess interstitials driven further into the bulk due to forward momentum transfer. The excess vacancies invoke recombination with excess interstitials and have been shown to reduce TED in Si.^{74–77}

1.3.5 Summary

Ion implantation is the preferred method for dopant incorporation into semiconductor devices due to its ability to efficiently locate well-defined dopant quantities has earned. However, ion implantation is a non-equilibrium process that introduces damage to the lattice. The damage to the crystalline lattice can vary from excess point defects to the complete amorphization of the surface region depending on the implant conditions

The activation and diffusion behavior of B in Si and Ge have been reviewed. For B in Ge, It has been established that B does not diffuse any appreciable amount in Ge under normal processing conditions. Complete activation has been observed with the electrical solubility limit as high as $5.5 \times 10^{20} / \text{cm}^3$ following a preamorphization implant. An inactive B-Ge cluster with the stoichiometry 1:8 was reported to occur for implants into crystalline Ge in which approximately half of the dose is rendered inactive. B

activation has been reported to be remarkably stable with no significant change during annealing.

In contrast, B in Si is susceptible to anomalous transient diffusion labeled TED which is characterized by diffusion far in excess of equilibrium values that decreases with time. TED is due to the excess interstitial population produced during extended defect dissolution diffusing and subsequently kicking out B from their lattice site allowing them to diffuse through the lattice. TED decreases as the extended defects evolve and the excess interstitial population decreases. Similarly, B activation in Si is controlled by the release of excess interstitials from extended defects forming interacting with B atoms to form inactive BICs. It has been shown that BIC formation and dissolution is a thermal process and that activation of 100% of the B concentration can be achieved given proper annealing conditions up to a certain temperature-dependent dopant solubility.⁵⁵

It should be noted that both the activation and diffusion behavior of B in Si as compared to Ge are widely different. The activation behavior of B in PA-Ge is reported to fully activate following an anneal at 360°C for 1h and maintain its activation with increased annealing. In contrast, the activation and diffusion behavior of B in Si is dependent on dopant-defect interactions and as such, varies as a function of annealing and subsequent defect environment.

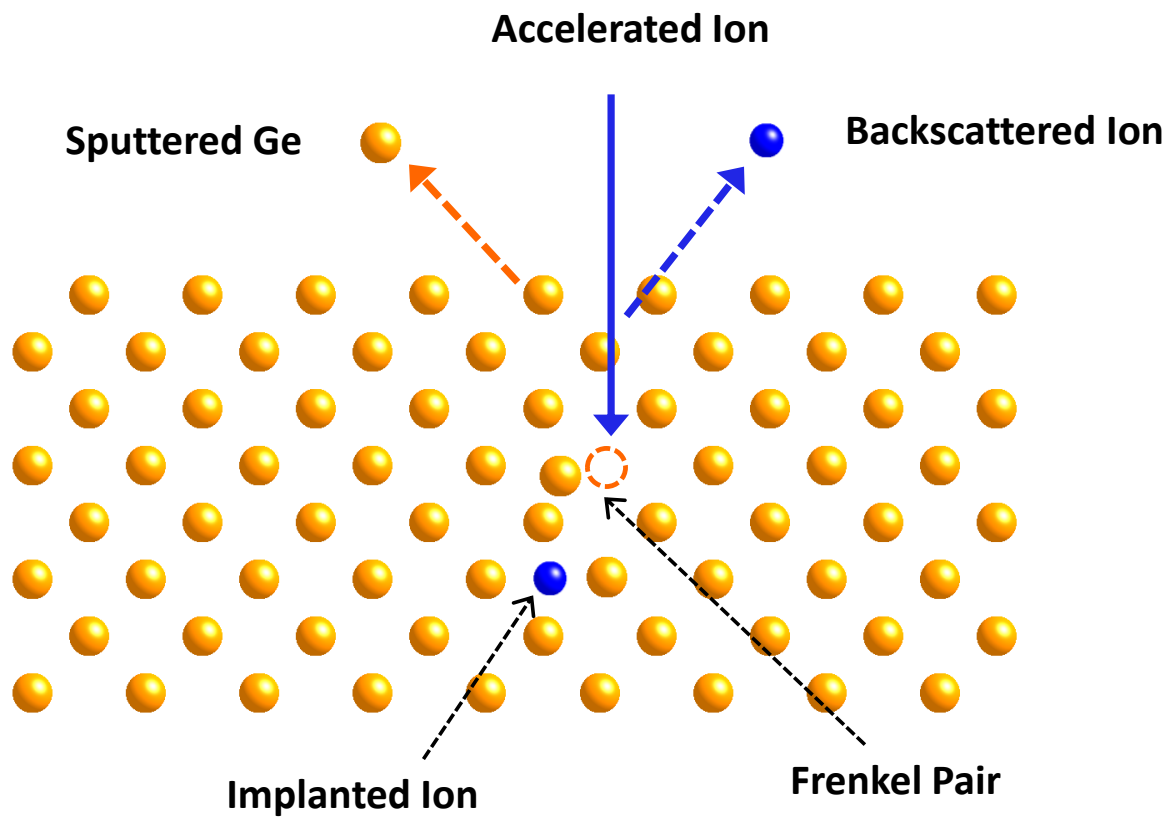


Figure 1-1. Schematic of the ion-solid interactions during ion implantation.

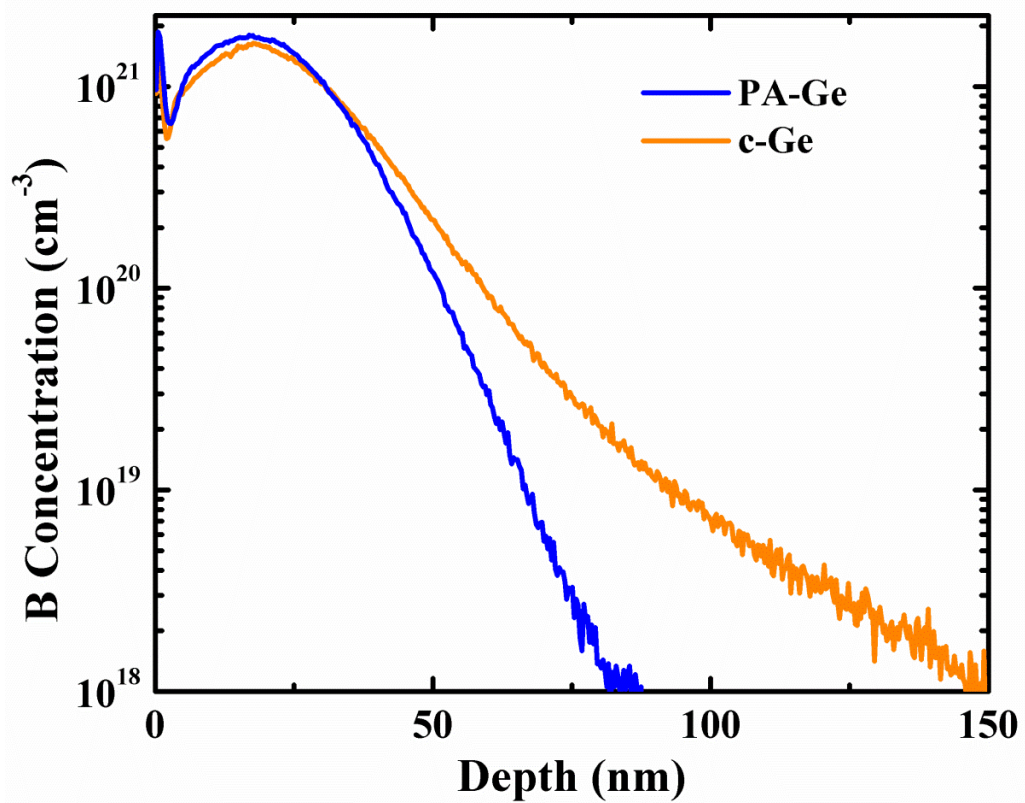


Figure 1-2. Evidence of the channeling tail in c-Ge. Concentration profiles resulting from a B⁺ implant at 6 keV to a fluence of $5.0 \times 10^{15} \text{ cm}^{-2}$ into c-Ge and PA-Ge.

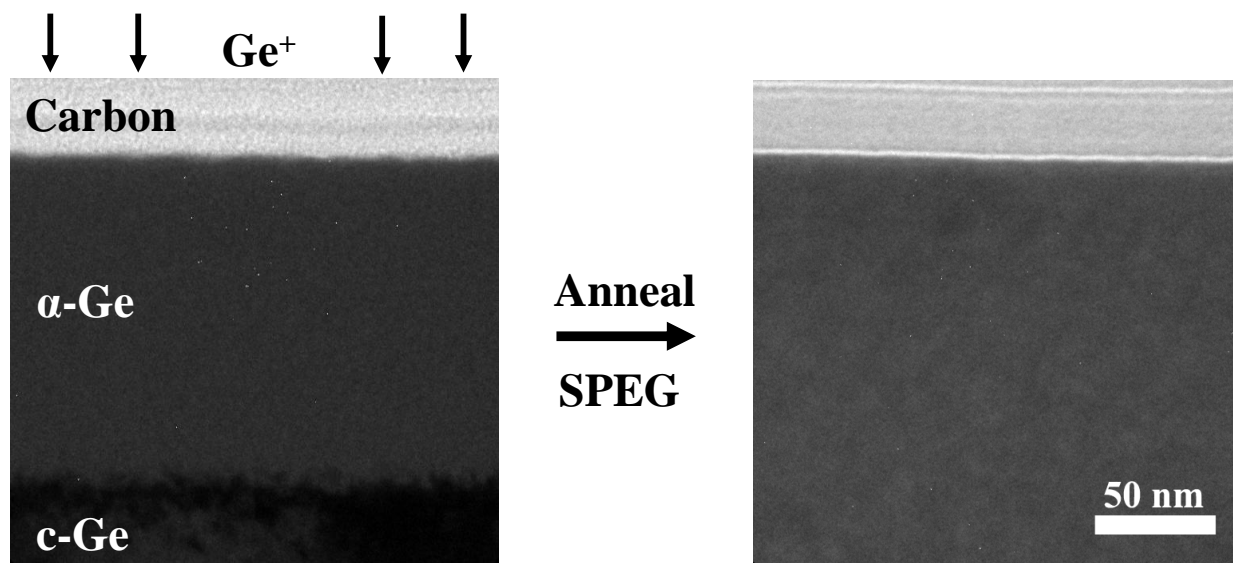


Figure 1-3. Schematic displaying the amorphization process in Ge. Crystalline Ge (c-Ge) is self-implanted at 120 keV to a fluence of $2.0 \times 10^{14} \text{ cm}^{-2}$ to amorphize surface layer. Sample is annealed and amorphous layer is regrown.

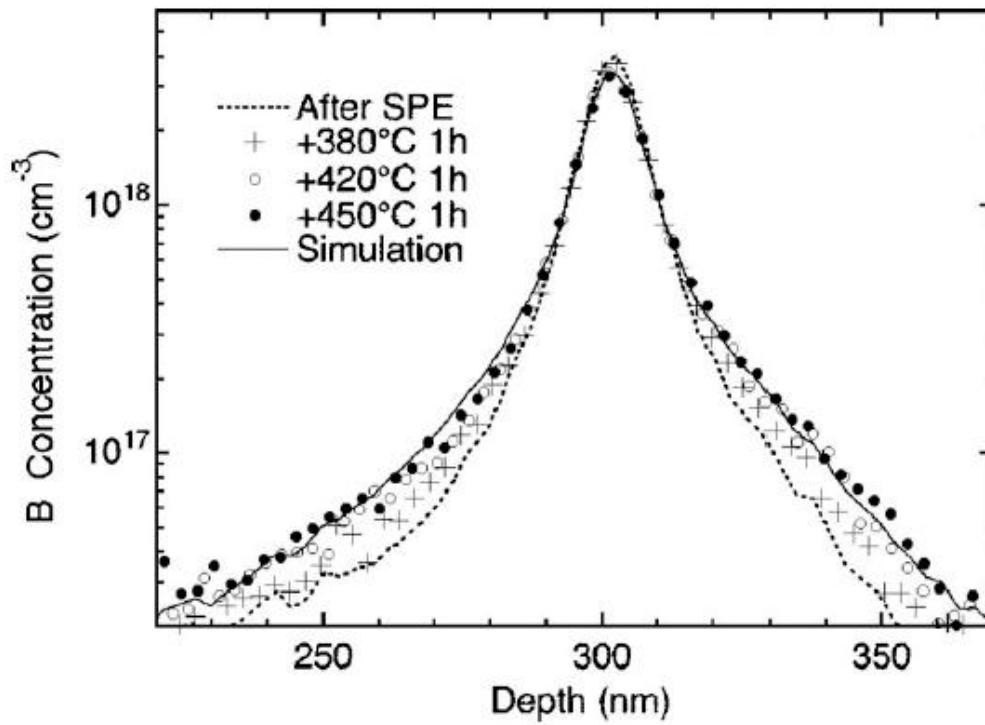


Figure 1-4. Evidence of transient B diffusion in Ge. Reprinted with permission from E. Napolitani, G. Bisognin, E. Bruno, M. Mastromatteo, G.G. Scapellato, S. Boninelli, D. De Salvador, S. Mirabella, C. Spinella, A. Carnera, and F. Priolo, *Appl. Phys. Lett.* **96**, 201906. Copyright 2010. American Institute of Physics.

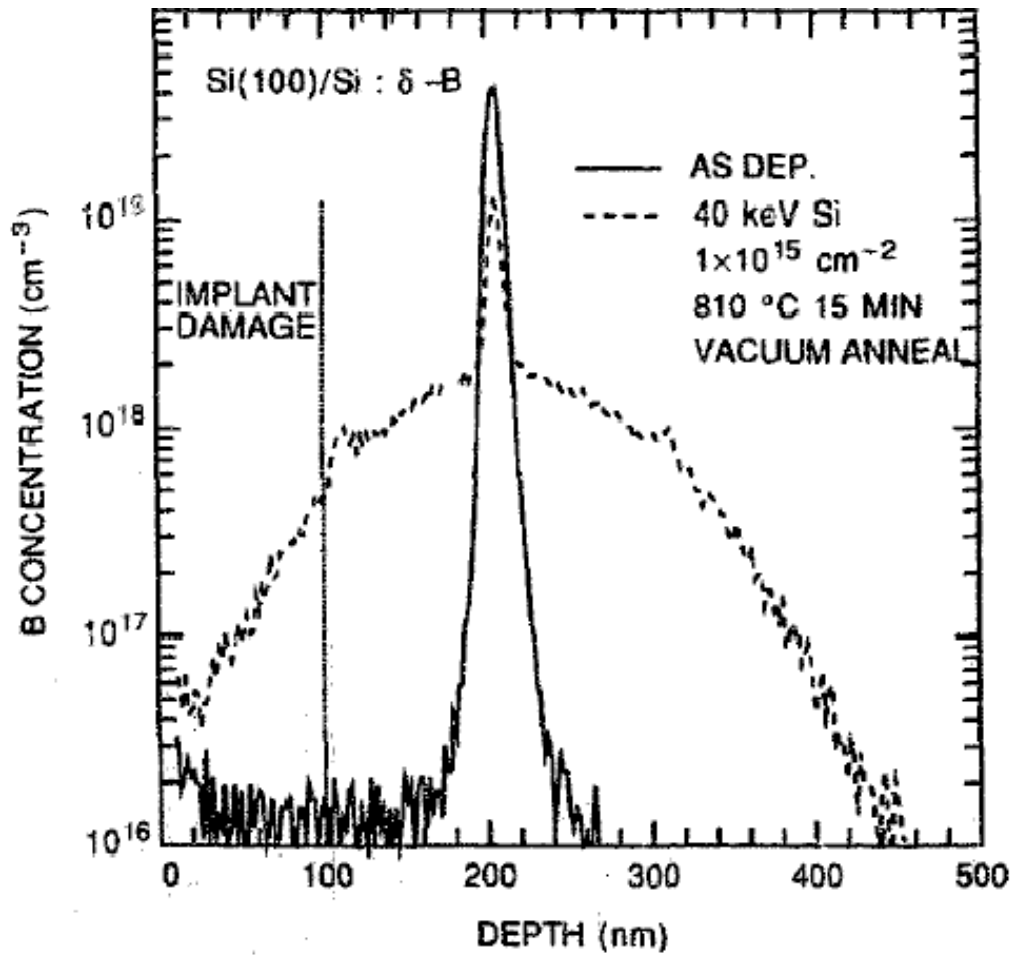


Figure 1-5. Typical B concentration profile following transient enhanced diffusion in Si. Reprinted from Stolk *et al* "Implantation and transient boron diffusion: the role of the self-interstitial", *Nucl. Instrum. Methods Phys. Res. B.*, **96**, 187-195. Copyright (1995), with permission from Elsevier.

CHAPTER 2 EXPERIMENTAL TECHNIQUES

This chapter serves to outline the various methods used to process and characterize the samples used for the experiments in this work. It is not intended to be a thorough explanation for the layman, but rather a brief introduction and explanation of the experimental details to assist the reader in understanding the steps taken in this work.

2.1 Materials Processing

2.1.1 Ion Implantation

In this work, ion implantation was used for the introduction of all dopant atoms into the Ge lattice. It was also used to induce the formation of an amorphous layer prior to dopant implantation by using a self-implant with a fluence above the amorphization threshold of Ge; commonly referred to as a preamorphization implant. All implants were completed using commercial ion implantation tools under high beam current conditions.

Boron implants were completed using fluences ranging from 5.0×10^{13} - 5.0×10^{15} cm^{-2} at energies ranging from 1-6 keV. The corresponding projected range of the implants varied from 4.0 to 16.5 nm as simulated by SRIM.⁷⁸ Ge amorphization was completed using self-implants with a fluence of 2.0×10^{14} Ge^+/cm^2 at 120 keV which amorphized the substrate to a depth of approximately 100 nm as verified by transmission electron microscopy. The preamorphization conditions were chosen to encompass the peak of the implanted dopant concentration profile for all investigated B^+ implant conditions. The inclusion of the B profile within the amorphous layer was done to reduce dynamic annealing and regrowth during B^+ implantation.³⁵

2.1.2 Dicing Saw

Group IV semiconductors are notably brittle which makes sample preparation difficult. Sectioning of wafers into research samples is typically completed using a high-speed wire saw or diamond-coated wire blade. The blade thickness is on the order of 100 μm and the blade speed is approximately 25 krpm. The high speed blade enables the dicing of brittle semiconductors into small samples, but creates kerf or chips along the edge of the samples. Kerf can be reduced by changing dicing parameters such as blade type or spindle speed, but can never be removed.

Edge kerf is a major problem for samples to be characterized using the micro Hall effect as a clean edge is of utmost importance. To circumvent this issue, samples were diced with the implanted surface down and programming the saw to not cut the last 50 μm of the wafer. In doing so, the wafer was not diced completely, but rather, the dicing was used to simulate a deep scribe to enable a clean cleave of the remaining 50 μm of material. The technique enables the manufacture of small samples with edges that are much sharper and cleaner than capable by dicing or cleaving alone.

2.1.3 Thermal Processing

Following ion implantation, thermal processing is necessary to activate the implanted dopant and to remove any residual implant or regrowth-related defects from the crystal lattice.⁷⁹ Activation, dopant diffusion, defect evolution and solid phase epitaxial growth (SPEG) are all thermally activated processes that follow an Arrhenius behavior. With all of the processes occurring simultaneously, it is necessary to find an ideal combination of temperature and time, or thermal budget, that produces the best combination of favorable material properties. For example, while a high temperature anneal for a long time may provide the best dopant activation,⁵⁵ it will also increase

dopant diffusion or may allow for the formation of extended defects that will be detrimental to device properties. It is this balancing act that has warranted the advancement of annealing technology towards temperatures in excess of the melting temperature, T_m , for ultra-fast times with femtosecond laser pulses.⁸⁰

For Si device processing, the primary focus towards these thermal budgets was driven by reducing transient enhanced diffusion (TED) which is a non-equilibrium diffusion process that is driven by dopant-defect interactions during annealing.^{57,67,81} TED is characterized by dopant concentration profiles that extend to much greater depths than those created immediately after implantation or even those expected from typical diffusion processes.

In addition, equilibrium diffusion of B in Ge is not significant which reduces the need for extreme thermal processing techniques.^{28–30} Although TED of B is not an important concern with Ge, rapid thermal annealing at increased temperature for shorter times allows for decreased processing times which is more relevant for industry as they reduce the total time required to process a device. The reduced time devoted to processing each has a direct economic benefit.

In this work, samples were thermally processed using two methods: standard furnace annealing and rapid thermal annealing. Standard furnace anneals were completed in a quartz tube furnace which is characterized by a heating coil that is wrapped around a 48" long quartz tube to adjust the temperature. The method is categorized as having a long sample ramp up and cool down period which is on the order of several minutes. Tube furnace anneals were completed with N₂ flowing at a rate of approximately 1 L/min to reduce surface oxidation. The sample was placed in a

pre-heated quartz boat and inserted to the center of the tube. The temperature was not measured directly at the sample, but rather the temperature of the boat was monitored with a thermocouple prior to beginning the annealing process. Due to the long duration of tube furnace anneals, for those anneals completed at 500°C or higher, samples were capped with SiO₂ to resist surface desorption.

In contrast to the long anneals completed with standard annealing, rapid thermal annealing (RTA) employs the use of high-powered incandescent tungsten lamps to control the temperature. The lamps are placed above and below the sample on the outside of an ambient-controlled quartz chamber which allows for rapid heating and cooling with rates on the order of 100°C/s. The sample is placed on a carrier wafer which is then placed on a quartz tray that is only in contact with the wafer by three small pins to reduce thermal conductivity. Due to quartz being transparent to the radiation produced by the lamps, RTA anneals are considered a cold wall process because only the sample and carrier wafer are heated during processing. The lack of chamber heating reduces chamber contamination and allows for short down times between processing runs.

Samples were processed in an N₂ ambient with actual annealing times on the order of 60 s with a ramp rate of approximately 50°C/s. The processing temperature was monitored in real-time with the use of a thermocouple sandwiched between two carrier wafers rather than bonding the thermocouple directly to the carrier wafer. The carrier wafer sandwich was employed to reduce the risk of carrier wafer breakage during processing. During processing, the thermal stress of quick ramp rates is significant and capable of fracturing large samples which is exacerbated by bonding the

thermocouple to the wafer. The temperature of the sample is not directly measured, but error in the actual processing temperature is believed to be due less than $\pm 3\%$. Due to the short duration of the anneals, no special surface preparation was employed for RTA anneals at or below 600°C . Above this temperature, an SiO_2 capping layer was employed to reduce Ge surface desorption.⁴¹ An AG Heatpulse 4100 was used for all RTA anneals in this work.

2.2 Electrical Characterization

2.2.1 Four Point Probe

A four point probe (4PP) test is a quick and simple testing procedure that is capable of producing the electrical resistivity of semiconducting materials. As the name suggests, the test is conducted with four equidistant probes through which two of the probes a current is passed and through the two remaining probes a voltage is sensed. There are three probe configurations used for 4PP measurements, but the most common is the 'C' configuration in which current is passed between 1 and 4 with voltage sensed between 2 and 3. This type 'C' probe configuration is displayed in Figure 2-1.

In this configuration, the electrical resistivity can be easily acquired if a few geometrical measurements are reasonably well known or if a few assumptions are made. As seen in Figure 2-2, for a sample with an area, A , length, L , resistivity, ρ , is related to the resistance, R , by the following equation:

$$R = \rho \frac{L}{A} \quad (2-1)$$

By separating sample thickness, t , and width, w , from the area term and combining the resistivity and thickness values, the resistance can be defined by a sheet resistance, R_s . In doing so, the resistance can be described independent of sample thickness which is

advantageous when describing doped layers created through an implantation process in which layer thicknesses are not always known. The relation between resistivity and sheet resistance is as follows:

$$R = \rho \frac{L}{A} = \frac{\rho}{t} \times \frac{L}{w} = R_S \frac{L}{w} \quad (2-2)$$

The units of sheet resistance are ohms (Ω), but it is typically represented as ohms/square (Ω/sq) to delineate between bulk resistance.

Assuming an equidistant probe spacing of s and a sample size in which $L, w \gg s$, and $t \ll s$, the sheet resistance is then measured from:

$$R_S = \frac{\pi}{\ln(2)} \frac{V}{I} = \frac{\rho}{t} \quad (2-3)$$

where I is the current applied through contacts 1 and 4, V is the voltage sensed between contacts 2 and 3, and t is the thickness of the conducting layer. However, as mentioned previously, for ion implanted samples, the thickness of the conducting layer is not always readily apparent. In addition, the reporting of sample resistivity may obscure the true electrical behavior of the conducting layer because it is a function of thickness; ie, a thin layer with the same R_S as a thick layer will be much more conductive in comparison. Therefore, sheet resistance is typically reported instead of resistivity values for ion implanted substrates.

2.2.2 Hall Effect

Although four point probe yields a quick and simple measure of sheet resistance, further characterization needs to be completed to fully comprehend the electrical behavior of implanted dopant atoms. The sheet resistance does not yield any information regarding the total number of electrical carriers or active dopants, commonly referred to as sheet number (n_S), or the drift mobility (μ_D) of charge carriers in the

semiconductor. The sheet resistance is related to the sheet number and drift mobility by::

$$R_S = \frac{1}{\int_{surf}^t q\mu_D n_S dt} \quad (2-4)$$

where R_S is related to the integral of the elementary charge q , μ_D , and n_S from the surface to the depth of the implanted layer t . Hall effect characterization enables the determination of whether any change in R_S is governed by n_S or μ_D and is crucial for full understanding of the electrical characteristics of the implanted layer.

The Hall effect enables the characterization of n_S or μ_D by measuring the electrical properties of a semiconductor in the presence of a magnetic field.⁸² The governing principle behind the Hall effect is the Lorentz force which states that when an electron with the elementary charge, q , is driven by an electric field to a velocity, v , in a direction perpendicular to an applied magnetic field, B , it experiences a force equal to $(-qv \times B)$ acting normal to both directions. Conversely, the same is true for holes where the charge is reversed. By applying a force to the charge carriers as they flow through the semiconductor, the path of the carriers is bent towards one side of the sample which creates a measurable electrical potential denoted the Hall voltage, V_H . An example of the Lorentz force in an n-type semiconductor is shown in Figure 2-3.

Typical Hall effect measurements are conducted on square samples 1cm on a side with contacts placed at the corners. For p-type Si or Ge samples, the use of InGa eutectic is an excellent contact material. The corner contact configuration also enables the characterization of the sheet resistance through the van der Pauw technique.^{83,84} For both Hall and van der Pauw techniques, electrical contacts should be less than $1/10^{\text{th}}$ the length of the sample and placed near the corner to reduce measurement

error.^{85–90} An illustration of the typical contact placement is given in Figure 2-4. The R_s can be calculated by measuring characteristic resistances through pairs of parallel contacts. For example passing a current through contacts 1 and 2 creates a measurable potential in contacts 3 and 4.(Figure 2-5) The characteristic resistance for this measurement is denoted $R_{12,34}$ and is calculated by dividing the measured potential by the applied current. The sheet resistance of the sample can be calculated by the following equation:

$$\exp\left(\frac{-\pi R_{12,34}}{R_s}\right) + \exp\left(\frac{-\pi R_{23,41}}{R_s}\right) = 1 \quad (2-5)$$

where the $R_{12,34}$ and $R_{23,41}$ values are measured which allows for the calculation of sheet resistance.

For Hall measurements completed in the van der Pauw configuration, a defined current on the order of 1 mA is passed through a pair of diagonal contacts (contacts 1 and 3 in Figure 2-5) in the presence of a perpendicular magnetic field on the order of 1 tesla which is typically produced by an electromagnetic magnet. The magnetic field deflects the carriers which creates the Hall voltage which is measured through the other pair of diagonal contacts (contacts 2 and 4 in Figure 2-5). The process is completed iteratively for all contact combinations and measured values averaged to minimize measurement noise.

The magnitude of the Hall voltage, V_H , is relates both the applied current and magnetic field through the following relation:

$$|V_H| = \frac{IB}{qn_H} \quad (2-6)$$

where I is the applied current, B is the applied magnetic field, q is the elementary charge of the carrier, and n_H is the Hall sheet carrier density. From the V_H measurement in which all terms are well-known, it is possible to calculate the Hall sheet carrier density. Similar to sheet resistance which is independent of thickness, the sheet carrier density (or sheet number) is the number of electrically active carriers in the sample independent of sample thickness and is given in the units of (cm^{-2}). Once n_H is known, the Hall mobility can be calculated from the following equation:

$$\mu_H = \frac{1}{qn_H R_S} \quad (2-7)$$

Due to the complex band structure of Ge, and the presence of neutral and ionized impurities creating scattering sites, a correction factor needs to be applied to the Hall values obtained to determine the true drift mobility and sheet number.^{91,92} The Hall scattering factor, r_H , relates Hall values to sheet number and drift mobility value by:

$$n_S = n_H \times r_H \quad (2-8)$$

$$\mu_D = \mu_H / r_H \quad (2-9)$$

where n_S is the sheet carrier density and μ_D is the drift mobility. The scattering factor can be determined through simulation or determined empirically.^{44,93–96} The measurements completed in this work were corrected using a scattering factor of 1.21 as determined empirically by Mirabella *et al.* for high dose B^+ implantation into Ge.³¹

2.2.3 Micro Hall Effect & Micro Four Point Probe

The length scales associated with modern and future IC devices are ever decreasing which creates issues with device metrology.⁹⁷ The narrow band gap of Ge (0.66 eV) compared to that of Si (1.21 eV)²⁵ in conjunction with the shallow and box-like ion profiles creates an environment primed for junction leakage from the implanted

layer.^{98–103} The increased leakage current is significant for next-generation devices, but also for device metrology which has driven the need for advanced metrology techniques. An example of leakage current affecting a Hall effect measurement is displayed in Figure 2-6.

A micro Hall effect and micro four point probe tool is a characterization method that is capable of measuring the electrical characteristics of ultra-shallow profiles. Its operation is very similar to that of conventional 4PP and Hall effect characterization in that four contacts are used, but with the a few caveats. The probe spacing is on the order of 20 μm as opposed to 1 mm which works to reduce or eliminate any influence from junction leakage. In essence, by decreasing the horizontal probe spacing, the vertical characterization depth is also decreased as seen in Figure 2-7.¹⁰⁴ By decreasing the probe spacing to the μm -scale, the techniques have earned the names micro four point probe (m4PP) and the micro Hall effect (MHE).

For 4PP characterization, the conversion from conventional to m4PP is rather straightforward in that the only change to the experimental method is that not only is C configuration used, but configuration A and B is also used to reduce measurement error. With reduced probe spacing, characterized volume shifts further towards the surface and leakage current effects are reduced.^{104–107}

However, the conversion of Hall effect measurements to the μm -scale are not as straight-forward. As opposed to the traditional van der Pauw configuration used for conventional Hall effect measurements, MHE measurements utilize the same in-line probes used for M4PP samples.¹⁰⁸ For conventional Hall effect measurements, the use of in-line contacts would not be feasible as the measurement relies on the deflection of

the current to create the Hall voltage. In order for MHE measurements to utilize in-line probes, it relies on the presence of an insulating boundary such as a cleaved edge. In addition to the influence of a magnetic field, the cleaved edge alters the current flow near the injection point which is detectable using the contact probes in the B-B' configuration as seen in Figure 2-8. The cleaved edge creates a resistance difference, $\Delta R_{BB'}$, measured between the B and B' probe configurations. Figure 2-9 gives evidence of the measurable resistance difference near the edge which is non-existent a mere 60 μm from the edge. Once the $\Delta R_{BB'}$ term is measured, the Hall sheet resistance, R_H can be extracted from the following equation:

$$\Delta R_{BB'} = \frac{2R_H}{\pi} \left[3\arctan\left[\frac{s}{2y_0}\right] - 3\arctan\left[\frac{3s}{2y_0}\right] \right] \quad (2-10)$$

where s is the probe spacing and y_0 is the distance from the sample edge. Once R_H is known, the drift mobility and sheet number can be calculated from:

$$\mu_D = \frac{\mu_H}{r_H} = \frac{ZR_H}{r_H R_s B} \quad (2-11)$$

$$n_S = \frac{r_H B}{qR_H} \quad (2-12)$$

where the constants are the same as those used in conventional Hall effect calculations.

In this work, all samples were characterized using a CAPRES microRSP M-150 at CAPRES in Kgs. Lyngby, Denmark.

2.3 Structural Characterization

2.3.1 Transmission Electron Microscopy

The transmission electron microscope (TEM) is an indispensable tool for studying semiconductors. It provides valuable information regarding ion implantation processing

of semiconductors and produces corroborating information for electrical data. A TEM relies on a high energy electron beam that is highly focused through a series of electromagnetic lenses towards an electron transparent specimen. Figure 2-10 shows a schematic diagram of a TEM. The interaction of the accelerated electron beam with the thin sample is capable of providing a wealth of information regarding the crystal orientation, chemical composition, and microstructural imaging to be brief. The significant advantage of TEM characterization over other methods is that the instrument has a tremendous spatial resolution owing to the ultra-small wavelength of accelerated electrons.^{109,110}

According to the de Broglie principle regarding wave-particle duality,¹¹¹ an electron's wavelength, λ , is related to Planck's constant, h , and its momentum, p , by:

$$\lambda = \frac{h}{p} \quad (2-13)$$

It is possible to calculate the momentum of the accelerated electron because the momentum of the electron can be determined from:

$$p = m_0 v = \sqrt{2m_0 qV} \quad (2-14)$$

where m_0 is the mass of an electron, v is the electron velocity, q is the fundamental charge, and V is the accelerating voltage of the microscope. Substituting Equation 2-15 into Equation 2-13 and excluding any relativistic effects, the wavelength of an accelerated electron as a function of voltage can be determined by:

$$\lambda = \frac{h}{\sqrt{2m_0 qV}} \quad (2-15)$$

Assuming a typical accelerating voltage of 200 kV, the electron wavelength is on the order of 2.7 pm. However, the resolution of contemporary microscopes are not close to

this value due to the inability to manufacture a perfect electromagnetic lens which introduces aberrations during operation. However, modern-day instruments are capable of sub-Angstrom resolution which enables the characterization of nanometer-scale features to be commonplace.

2.3.1.1 TEM Sample Preparation

For TEM characterization to be effective, the sample must be thin enough to be transparent to the beam. With increasing sample thickness, the beam undergoes additional elastic and inelastic scattering processes which decrease spatial resolution. Due to increased scattering in the sample, a fraction of electrons will lose a small amount of their initial energy which is typically on the order of 10 eV. Due to the difference in energy, chromatic aberration will be introduced which will greatly reduce the resolution of the TEM.¹¹⁰ Unfortunately, scattering increases with increasing atomic mass which makes the sample preparation for Ge much more difficult than for Si. For high-resolution imaging of Ge, the sample thickness should typically be under 50 nm.¹¹²

The preparation of electron transparent semiconductor samples is not a trivial task. It is commonly more involved and time-consuming than the TEM characterization that follows. In general, there are two primary orientations for TEM characterization of semiconductors: 1. Cross-section or XTEM and 2. Plan-view or PTEM. In both orientations, it is critical to protect the surface as most ion implant processes place the region of interest (ROI) within 1 μm of the surface. Modern sample preparation relies heavily on ion beam preparation of TEM samples with both focused ion beam (FIB) and broad ion beam (BIB) milling tools widely used.

In this work, plan-view TEM samples were prepared using a broad ion beam (or ion mill) to produce electron transparent samples. PTEM samples were created by

dicing a 1 × 2 mm rectangle of the material followed by the mechanical thinning the back side of the sample to a thickness of approximately 10 μm as monitored by optical microscopy. A piece of Si was polished on the same stub to use a thickness reference because Si is well-known to be transparent to infrared when approximately 10 μm thick. Once thinned, a 3 mm Cu grid with oval opening was affixed to the back of the sample using M-Bond 610. The samples were then polished using a Fischione 1010 ion mill at an accelerating voltage of 3kV, a beam current of 5 mA, and a milling angle of 15°.

Cross-sectional TEM samples were prepared using a focused ion beam (FIB). A FIB is essentially an SEM which has a high-current focused Ga⁺ beam mounted at 52° to the electron column which enables a sample to be milled from the surface of interest. In order to protect the sample from Ga⁺ implantation and damage, an approximately 100 nm thick layer of carbon is thermally evaporated *ex situ* prior to beginning sample preparation. *In situ* Pt is deposited on top of the ROI to further protect from ion milling damage. Sample preparation proceeds by milling trenches on both sides of the ROI which progress closer to each other until the sample is thinned to approximately 1 μm thick lamella. The sample is then transferred *in situ* to a Cu grid where it is thinned to electron transparency. As thinning progresses, beam energy and current is decreased to reduce the amount of damage imparted to the sample.

In comparison to a broad ion beam system, FIB preparation is advantageous for its site-specificity, ease and quickness of operation, and low volume of material needed for sample preparation. However, a significant downfall of the FIB is the incredible difficulty of creating a PTEM sample which typically results in low quality. In general, FIB samples are of lower quality than other traditional methods due to the high current

and high ion energy which creates a layer of damaged or amorphous material on both sides of the sample. The damaged layer can be reduced by decreasing the ion energy for the final milling steps, but the resulting sample is still hindered by a damaged surface. Typical edge damage of ion milled and FIB milled samples is depicted in Figure 2-11. Despite the low energy polishing mill used in the FIB, it is evident that ion milled samples exhibit less surface damage. However, both methods provide adequate samples when proper care and attention is given during the preparation.

2.3.2 Secondary Ion Mass Spectrometry

Secondary ion mass spectrometry, or SIMS, is a destructive chemical analysis technique that is used to quantify minute dopant and impurity concentrations in semiconductors with a sensitivity to levels as low as $1 \times 10^{13} \text{ cm}^{-3}$.^{113,114} The ability of SIMS to detect minute impurity concentrations lends itself well to semiconductor characterization which is the biggest proponent of its use. In addition, it is capable of providing a dopant concentration depth profile from the surface to a depth of several microns with a resolution of approximately 1 nm.

SIMS profiling of B in Ge is carried out by accelerating a focused beam of primary Cs or O ions at a fixed flux towards the surface of interest. The impact of the primary ion at the surface induces the ejection of surface atoms from the surface of the material through a sputtering process. A fraction of these ejected atoms are ionized and are called secondary ions. The primary and secondary ions that escape the material are then passed through a mass-analyzer which separates the ions based on mass and charge by varying the magnetic field. Once the secondary ions are separated, they are sent to a mass spectrometer and the counts collected. The mass

spectrometer allows for the detection of all elements and provides an elemental profile of the impurities in the sample.

The primary ion beam sputtering of the material creates a crater in the surface which can be measured *ex situ* to determine the sputtering rate and profiling depth. The combination of secondary ion counts and sputtering rate is used to create the dopant depth profile. However, the construction of the concentration profile is not trivial due to differences in sputtering and ionization yields between the primary ions and the impurity and substrate atoms.¹¹⁵ The differences in sputter and ionization yield is a function of the surface chemistry and primary ion. Because of these differences, the use of a calibration standard is required for accurate depth profiling. Typically, for ion implanted samples, an as-implanted sample is used as a calibration standard by averaging the ion signal with the ratio of the implanted fluence to the sputtered depth.¹¹⁶ In addition, the near-Gaussian shape and the assumed $\pm 1\%$ implant uniformity provides further confirmation that the implanted species is being measured rather than some other interfering species. The use of an as-implanted sample is assumed to be valid because both samples should have the identical chemical compositions in the absence of any dopant out diffusion. Fortunately, this is not an issue for B in Ge under typical processing conditions.

An important issue for characterizing dopant profiles of ultra-shallow implants is the presence of profile artifacts produced during the sputtering of a surface or interface. These issues arise due to differences in dynamically changing ion yields in these near-surface and near-interface regions and exhibit themselves as an anomalous change in concentration unique to each sample characterized. These effects can be reduced by

using a primary ion with increased mass, decreased sputtering angle, or by evaporating a thin film of the substrate material on the surface^{117,118}; however, the complete removal is not possible. Due to the presence of surface artifacts, SIMS profiling of ultra-shallow B in Ge is not capable of producing absolute fluence measurements, but is satisfactory for comparison between as-implanted and processed concentration profiles.

2.3.3 Rutherford Backscattering Spectrometry

Rutherford backscattering spectroscopy, or RBS, is an ion beam analysis technique that takes advantage of the inherent structure of a crystalline material to monitor the composition and structure of the surface of a sample.¹¹⁹ The technique utilizes a beam of light ions, typically H^+ or He^{2+} , that is accelerated to an energy in excess of 0.5 MeV and directed towards a target precisely aligned along a crystal axis. The primary ions enter the sample to a given depth and collide with a target atom. Following collision with the sample, ions are backscattered and collected by an energy-sensitive detector. A plot of backscattered ion counts versus energy is then created from which information regarding the crystal structure is determined. For example, Figure 2-12 displays the channeling yield for a (001) Ge sample amorphized to a depth of 100 nm (black) and an as-received (001) Ge wafer. The randomized structure of the amorphized sample increases ion counts significantly over the pristine sample. In contrast, the pristine Ge sample allows for ion channeling down the (001) axis which reduces ion counts. The peak for the virgin crystal is due to increased scattering at the surface due to the presence of a surface oxide. The energy spread of the increased damaged counts of the amorphized sample corresponds to the thickness of the amorphous layer in which energy of the backscattered particles directly corresponds to

a distance or depth travelled through the crystal. From the difference in counts between two samples, the number of displaced Ge atoms can be determined.

One of the primary drawbacks of RBS is the low sensitivity for light elements, which often requires the combination of other nuclear based methods like nuclear reaction analysis (NRA) or elastic recoil detection analysis (ERD) which will be discussed in following sections. In addition, its chemical sensitivity¹²⁰ and depth resolution¹¹⁹ are orders of magnitude less than that of other techniques. However, its ability to accurately monitor crystal damage is an advantage that few other techniques offer.

2.3.4 Nuclear Reaction Analysis

Nuclear reaction analysis, or NRA, is a technique that provides quantitative information regarding the chemical concentration and lattice location of light impurities in semiconductors. Similar to RBS, it utilizes the interactions of accelerated light ions and target nuclei to characterize the target.¹¹⁹ However, the primary advantage of NRA characterization is its ability to quantify absolutely the concentration and location of light elements such as B.

During NRA characterization, the primary ion undergoes a characteristic nuclear reaction with the impurity atom of interest where the reaction byproducts are counted. For example, a typical reaction induced protons reacting with boron is described by $^{11}\text{B}(p, \alpha)^8\text{Be}$ where the reaction produces an alpha particle and are directly proportional to the B concentration in the target. (Figure 2-13) More significant to this work, by analyzing the target along known orientations such as $\langle 001 \rangle$, $\langle 011 \rangle$, and $\langle 111 \rangle$, it is possible to determine if the dopant is sitting in a preferred crystallographic orientation.

To complete NRA and lattice location characterization of B lattice location in Ge, several standards are needed to complete the experiment. Namely, a sample with B randomly distributed in amorphous Ge simulates the yield for a completely random or off-lattice distribution of B and a pristine (001) Ge wafer simulates the yield for a completely substitutional distribution of B. Typical yield profiles for the emitted α -particles are shown in Figure 2-18. Using these spectra as a reference, it is possible to determine the fraction of B that is substitutional in an unknown sample through the use of the following equation:

$$f_s(B) = \frac{1-\chi^B}{1-\chi^{Ge}} \quad (2-16)$$

where $f_s(B)$ is the fraction of substitutional B, χ^B is the ratio of the off-lattice and random yield, and χ^{Ge} is ratio of the number of displaced atoms measured in the pristine (001) sample to the number of displaced atoms measured in the random sample. The normalized channelling yield χ (χ^{Ge} and χ^B , for Ge and B atoms, respectively) is defined as the ratio of the aligned yield to the yield of randomly directed beam. χ^B is obtained from the α particle yield normalized to the random yield and is proportional to the fraction of B displaced out of the lattice. χ^{Ge} is measured just below the surface peak of the backscattered proton spectrum. The characterization is completed along the three major axes which enables the determination of lattice location of displaced B atoms.

2.3.5 Elastic Recoil Detection

Elastic Recoil Detection, or ERD, utilizes similar principles to those discussed in preceding sections on RBS and NRA where an accelerated ion impacts a target and the reaction products measured. NRA relies on elastic scattering between the primary ion and the target atom for the ability to monitor elemental concentration and depth profiling

of light impurity atoms in heavy atomic mass targets. However, in contrast to RBS and NRA, ERD typically utilizes a heavy ion, such as Si, to forward-scatter light recoil ions, such as B, towards a detector for characterization. The forward scattered yield of light ions is directly proportional to the chemical composition in the solid which allows for quantitative elemental analysis.¹¹⁹ Similar to RBS, ERD allows for absolute quantification of dopant concentration in the absence of a calibration standard. In addition, its sensitivity to light elements makes it an ideal candidate to determine the chemical concentration of B in Ge.

In an ERD experiment, a beam of heavy atomic mass ions are accelerated toward a target consisting of a matrix of heavy atomic mass atoms with an unknown concentration of impurity atoms of interest. The primary ion is angled at grazing incidence with the detector also placed at grazing exit incidence. A thin mylar foil on the order of 10 μm thick is placed in front of the detector as depicted in Figure 2-15. The light atomic mass of the impurity atoms allows for easy penetration through the foil whilst stopping the primary ions as well as any forward scattered matrix atoms. The detected counts allow for the conversion into an elemental areal concentration.¹²¹

2.4 Summary

In this work, a combination of electrical and structural characterization yielded information regarding the properties of ion implanted B in Ge following thermal processing.

Ion implantation was used to introduce a precise amount of B into (001) Ge substrates. Elastic Recoil Detection was used to quantify the residual implanted B fluence as a function of energy. It was shown that a significant fraction of implanted dopant was lost due to ion backscattering in good agreement with simulations.

Secondary ion mass spectrometry was used to monitor the B concentration profile as a function of annealing temperature. Electrical characterization was carried out with micro Hall effect and micro four point probe techniques to determine the sheet resistance, sheet carrier density and the drift mobility of B⁺ implanted samples. Nuclear reaction analysis and Rutherford backscattering spectrometry was used to yield information regarding the lattice location of B following processing to corroborate electrical data.

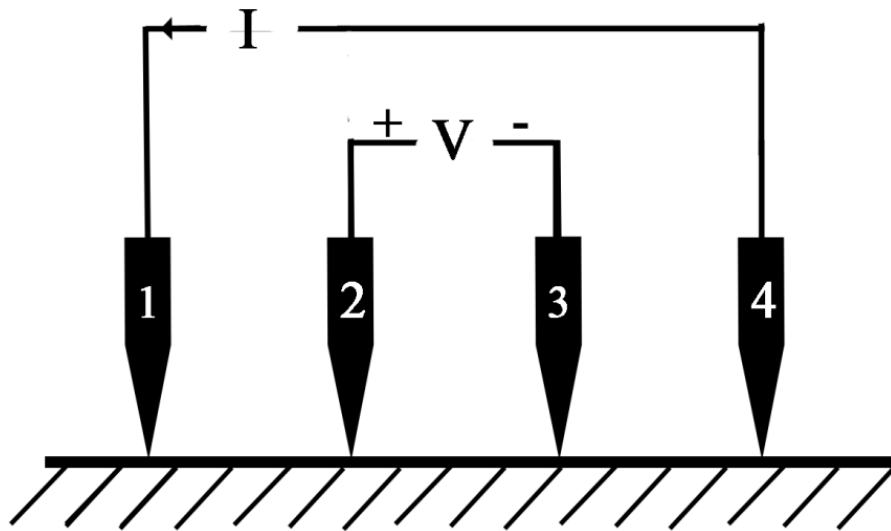


Figure 2-1. Schematic of four point probe configuration used to determine sheet resistance, R_S .

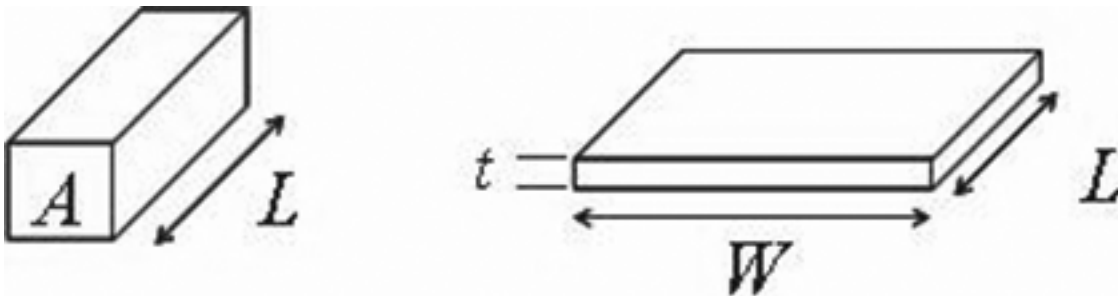


Figure 2-2. Sample geometry for a four point probe measurement

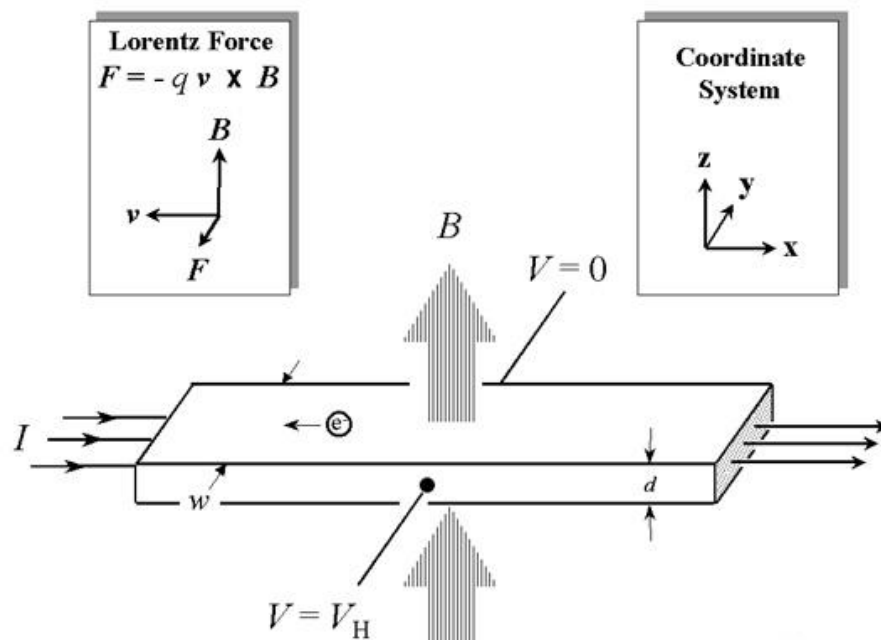


Figure 2-3. Illustration of the electrons passing through a solid in the presence of a magnetic field.

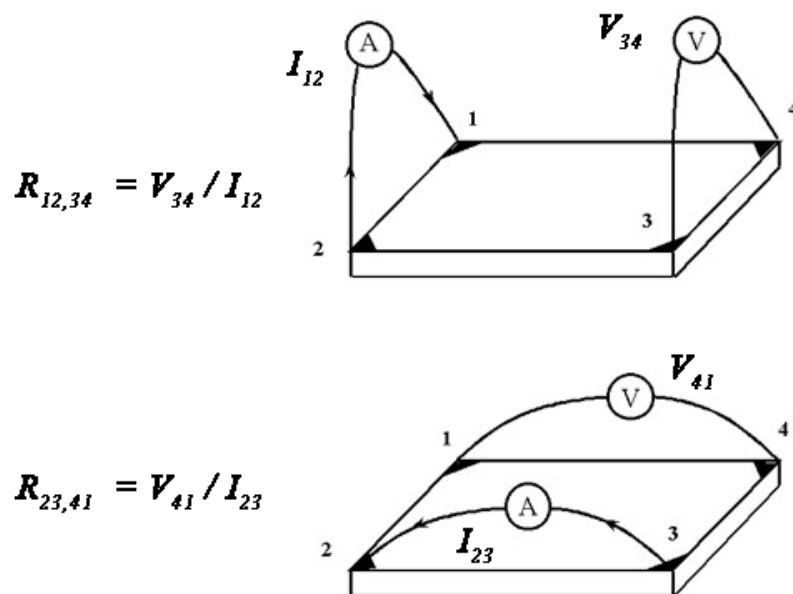


Figure 2-4. Schematic of the van der Pauw contact scheme

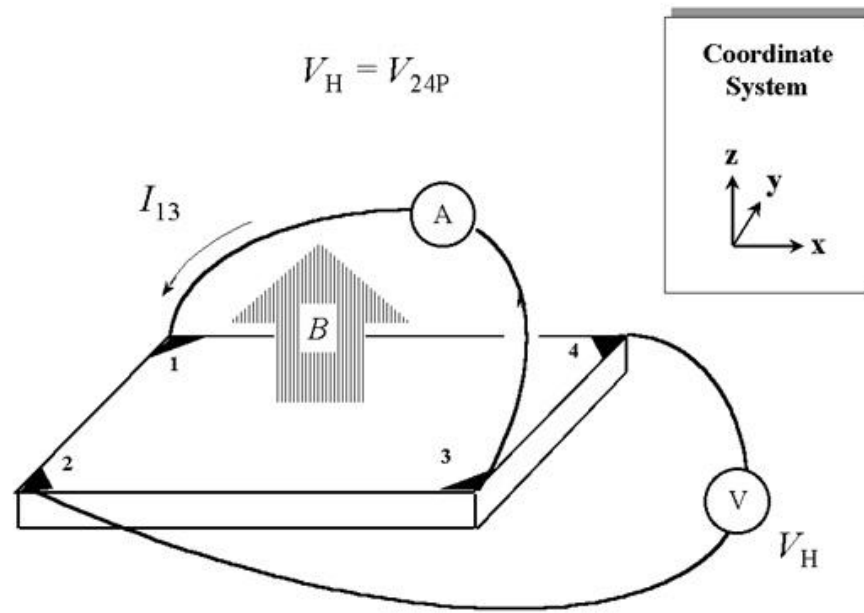


Figure 2-5. Illustration of the contact scheme typically used for Hall effect measurements. Current is passed through contacts 1 and 3 and V_H is measured through contacts 2 and 4.

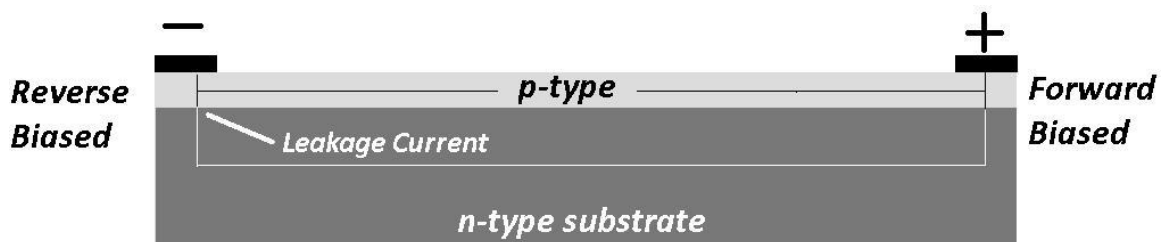


Figure 2-6. Leakage current into the n-type substrate can dominate a measurement if the metallurgical junction is not sufficient.

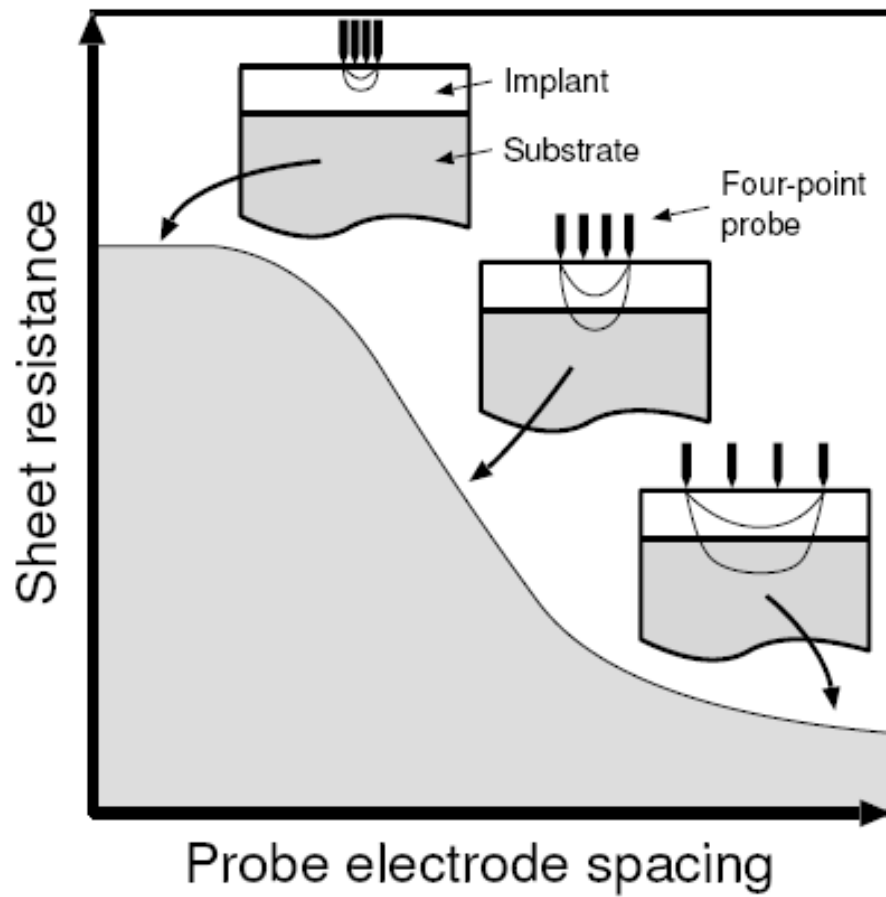


Figure 2-7. Decreased horizontal length scale of measurement probes reduces the junction leakage.

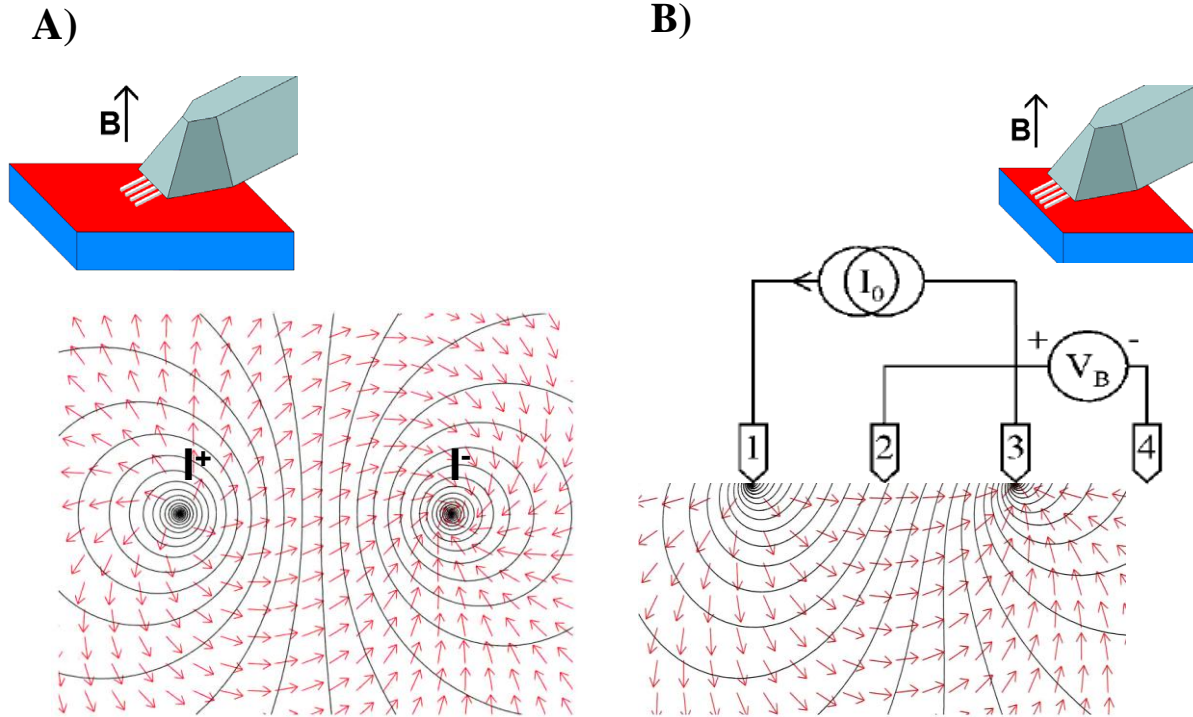


Figure 2-8. Current paths near contacts for M4PP measurements under the influence of a magnetic field. A) In the bulk, current travels tangentially around current injection contact. B) Near an insulating boundary, the current fields in the sample undergo a detectable shift.

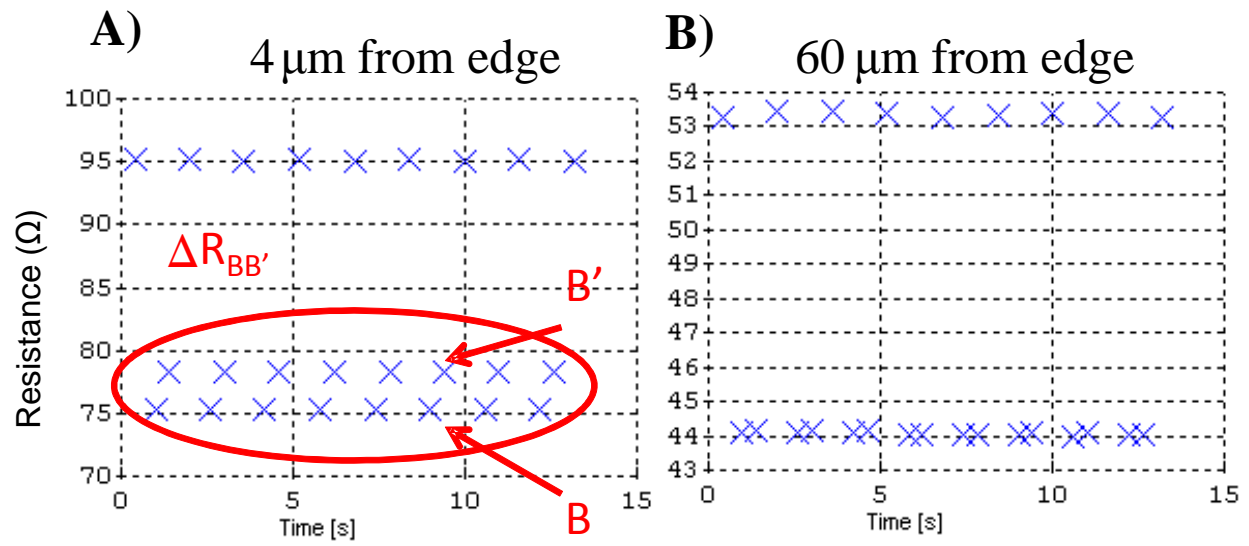


Figure 2-9. The presence of a cleaved boundary gives rise to a resistance difference, $\Delta R_{BB'}$, between B and B' during micro Hall effect measurements. At A) 4 μm from the cleaved edge which is not evident in B) at 60 μm from the cleaved edge.

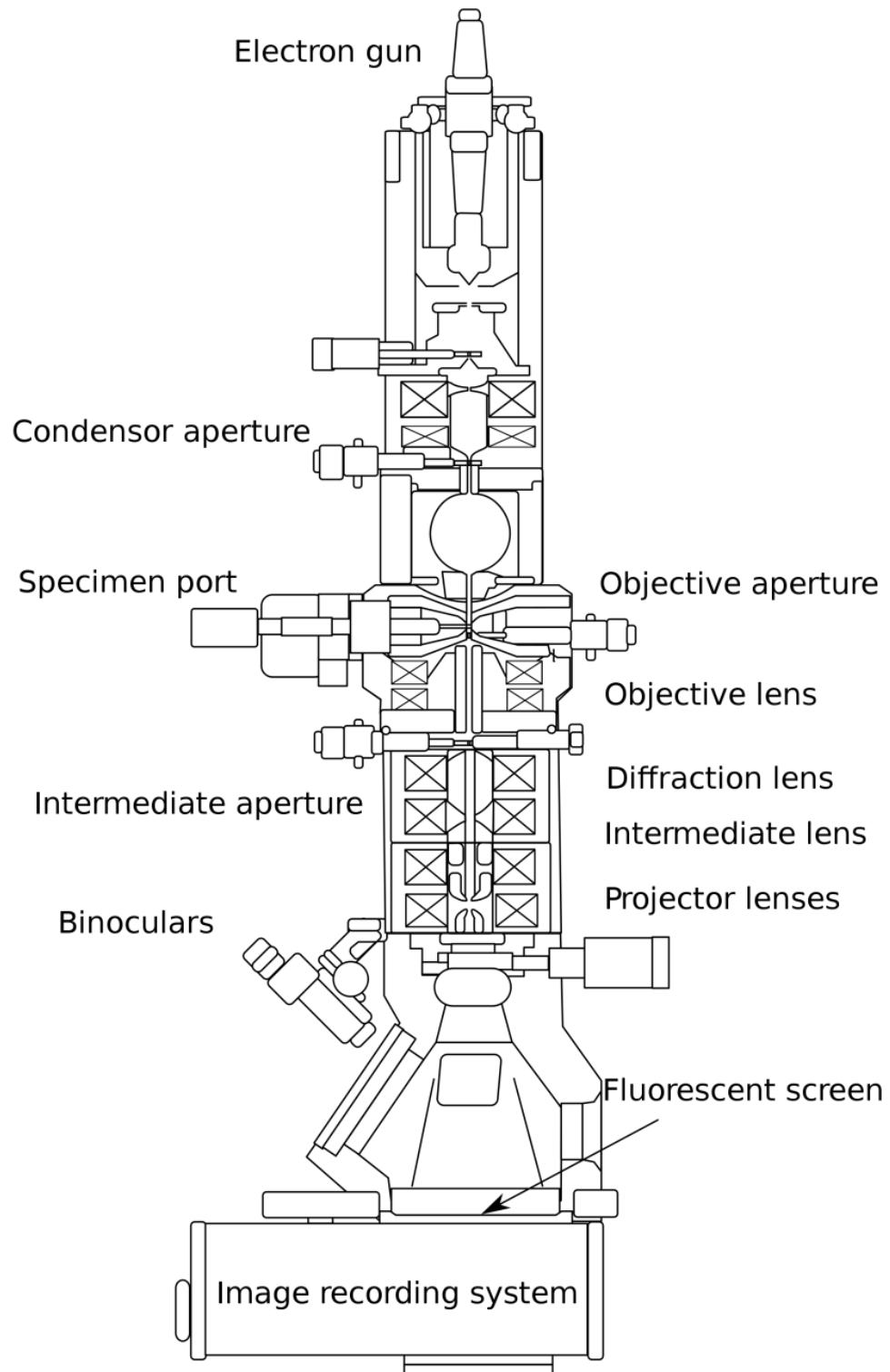


Figure 2-10. Schematic diagram of a TEM.

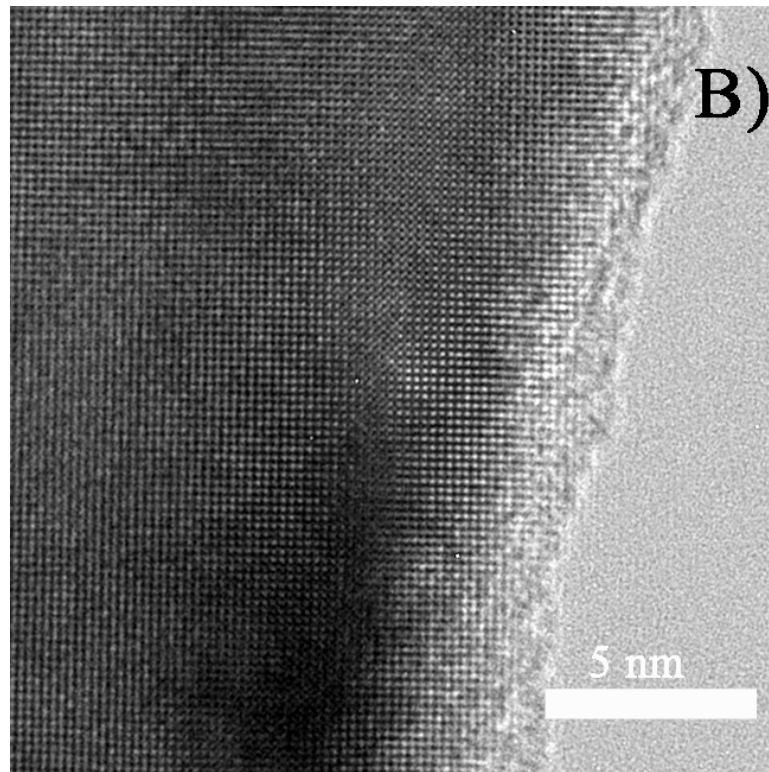
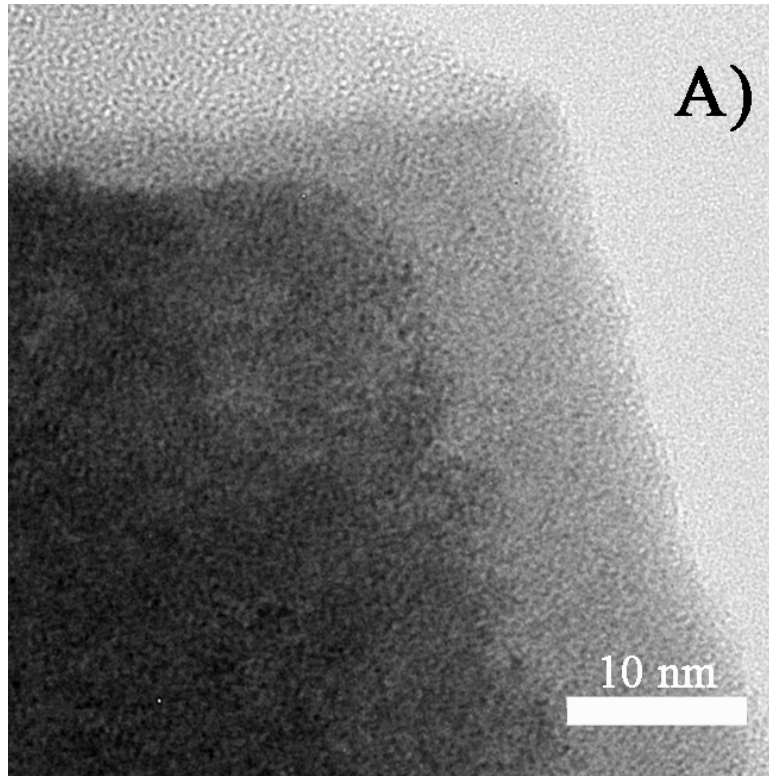


Figure 2-11. Representation of typical damage layer produced by FIB milling A) at 7 kV with Ga^+ beam and B) ion milling at 3 kV with Ar^+ beam.

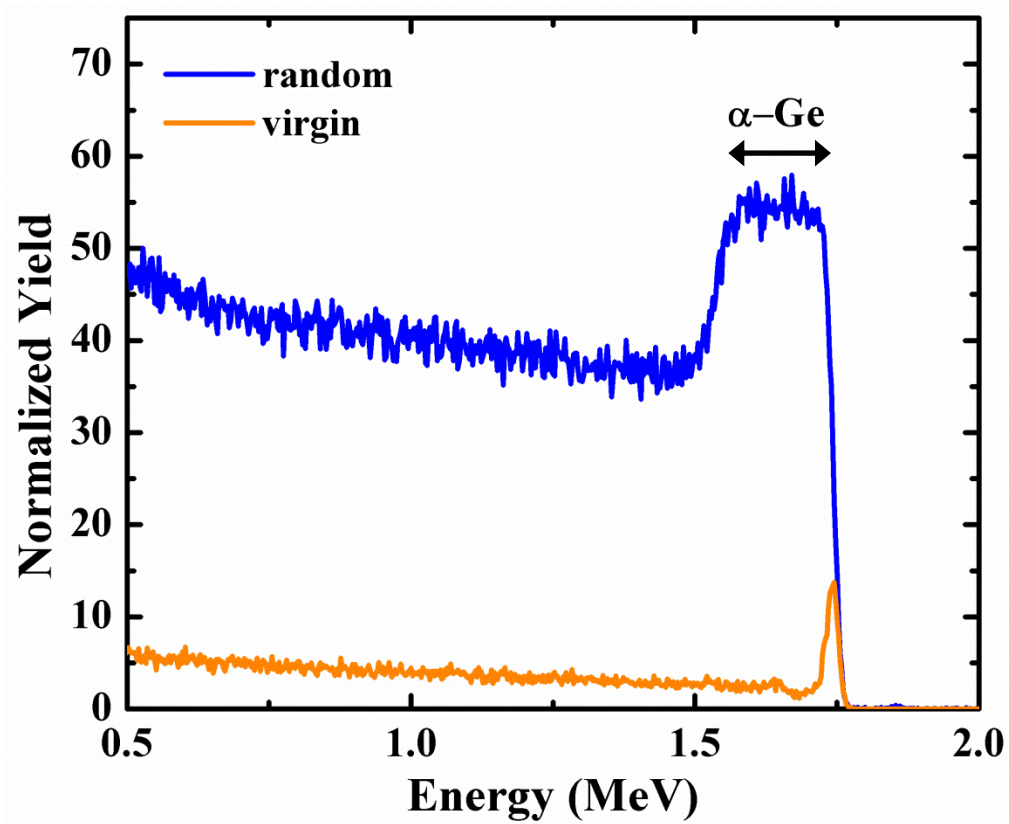


Figure 2-12. Typical data produced from c-RBS experiment. (001) Ge crystal amorphized to a depth of 100 nm with a 100 keV Ge⁺ implant to a fluence of $2.0 \times 10^{14} \text{ cm}^{-2}$ and a virgin substrate.

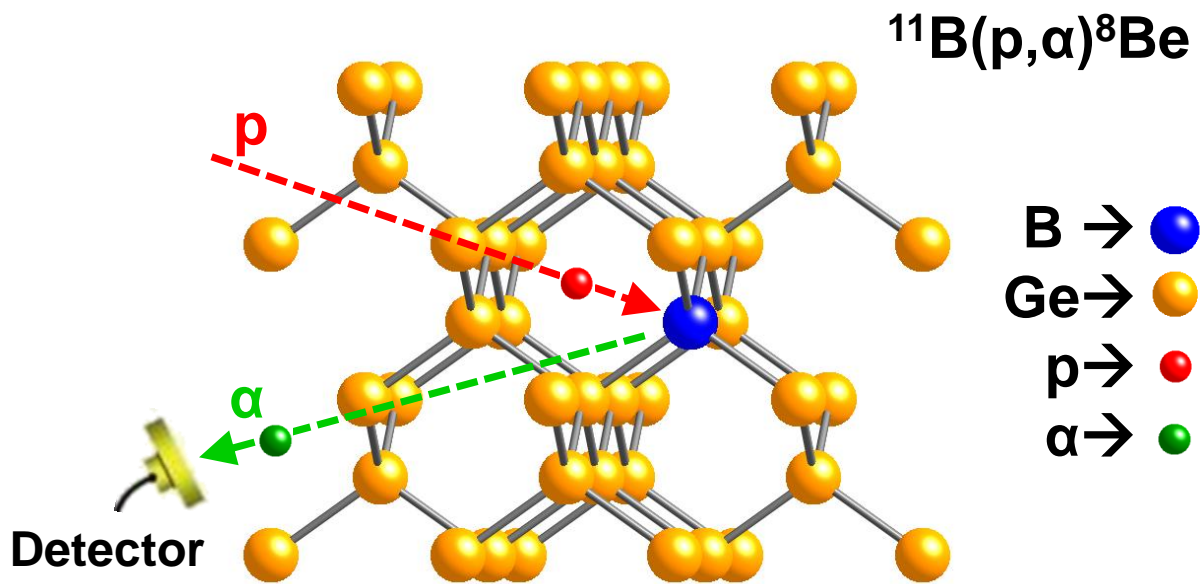


Figure 2-13. Illustration of a nuclear reaction between a proton and a B atom as it produces an α -particle

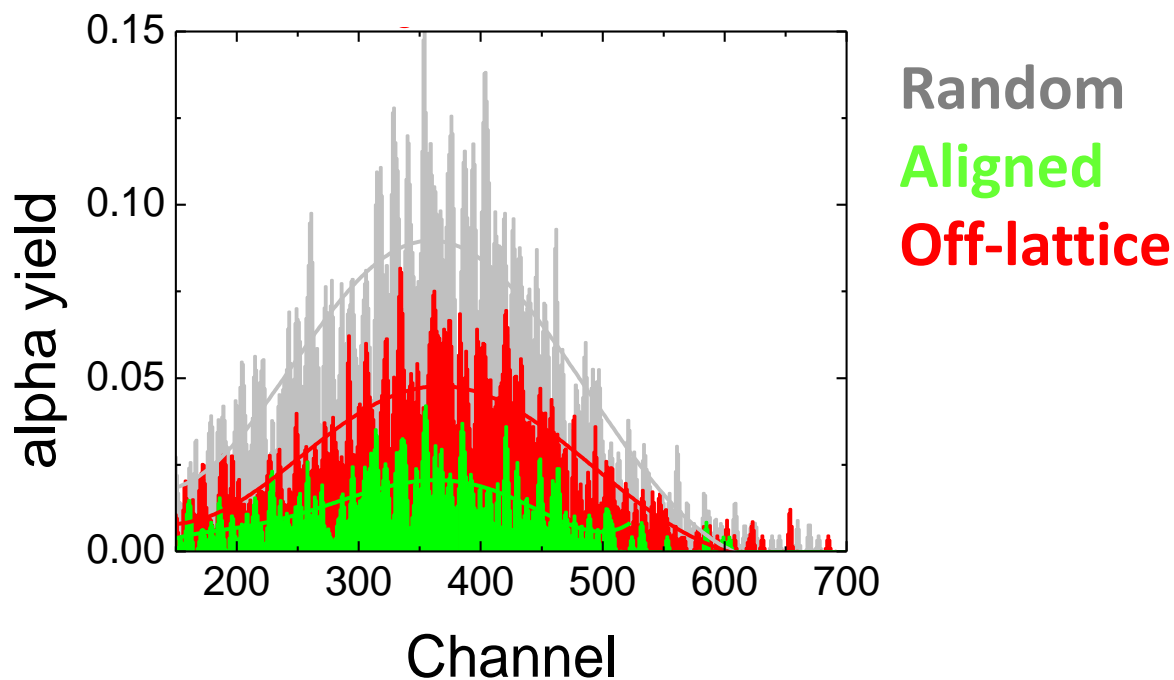


Figure 2-14. Representation of α particle counts produced by analyzing B atoms in different confirmations; randomly oriented (grey), fully substitutional (green) and off-lattice (red).

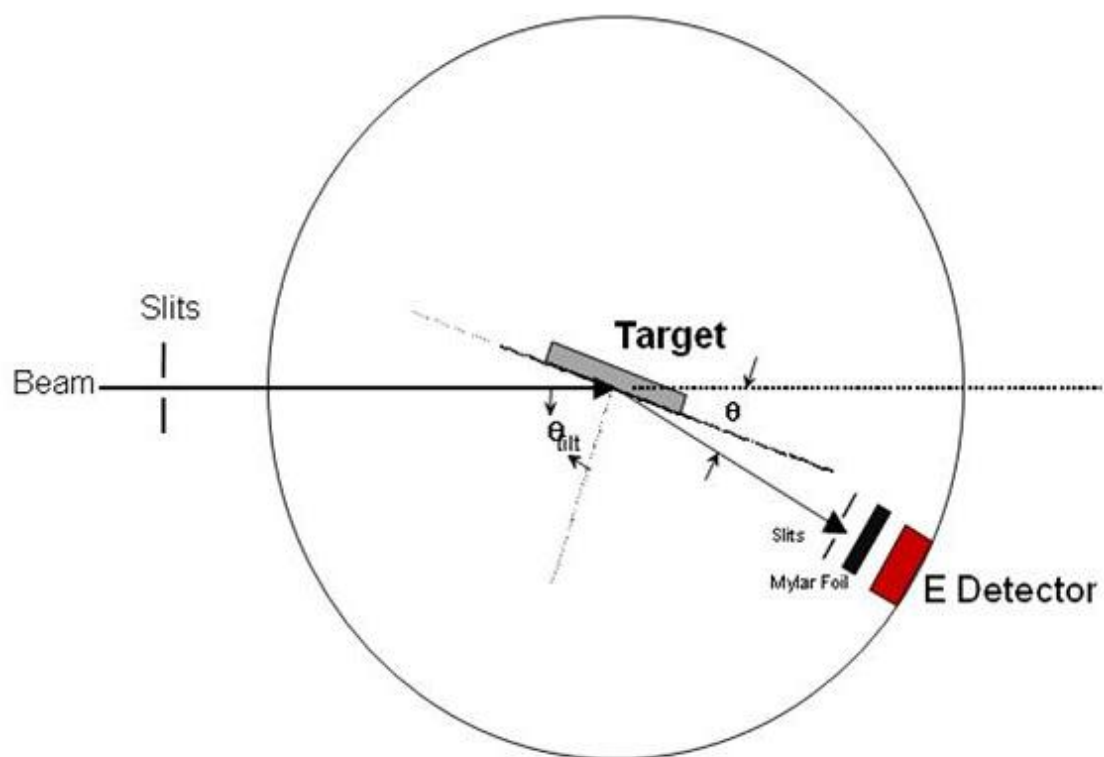


Figure 2-15. Experimental setup of an ERD experiment

CHAPTER 3 ACTIVATION OF ULTRA-SHALLOW BORON IMPLANTS IN GERMANIUM

3.1 Activation of B⁺ Implants in Ge

As the scaling associated with traditional Si metal oxide semiconductor (MOS) devices reaches fundamental limits, changes in MOS design or material composition are becoming necessary. Ge is a promising alternative material for next-generation MOS devices as its increased carrier mobility makes it an attractive replacement for Si.² In addition, its reduced melting temperature may allow for less aggressive annealing recipes which could prove advantageous for process integration of high- κ /metal gate device structures.

In the case of B, it is known that the equilibrium chemical solid solubility limit in Ge²⁸ is $5.5 \times 10^{18} \text{ cm}^{-3}$ at 850°C, which is significantly lower compared to Si at the homologous temperature.^{55,122} However, electrical activation in excess of this value has been reported for B⁺-implantation into single-crystal (c) as well as pre-amorphized (PA) material.^{23,31,34,35,37,46,123} For B⁺ implants at 35 keV into PA-Ge, complete activation was observed for all doses up to $7.6 \times 10^{15} \text{ cm}^{-2}$ implying active B concentrations as high as $5.7 \times 10^{20} \text{ cm}^{-3}$ following an anneal at 360°C for 1 h.³¹ In the case of PA-Ge, annealing to induce solid-phase epitaxial growth (SPEG) of the amorphized layer results in the incorporation of a concentration of substitutional B greater than the equilibrium chemical concentration; analogous behavior has been similarly reported for the case of B⁺-implantation into Si.¹²⁴

Although B activation has been characterized for deep B⁺-implantation into both c-Ge and PA-Ge, the activation of low energy B⁺-implantation in Ge remains poorly understood and characterized. In the few studies which utilized low energy B⁺-

implantation, the activation level, if determined, was calculated indirectly by fitting resistance values to a mobility model.^{23,45,123} This model was developed using Hall effect measurements and may suffer from possible error introduced from Hall scattering factor assumptions.⁴⁴ In order to accurately characterize the activation behavior, the sheet carrier density and mobility should be measured directly using a Hall effect technique.

Characterization of shallow implant activation is very challenging and in some cases impossible with conventional four-point probe and Hall effect techniques partially due to high junction leakage.^{104,125,126} Due to the smaller band gap of Ge compared to Si and the larger number of intrinsic carriers², junction leakage is increased for Ge^{98,127} which exacerbates the characterization challenges. Recently, instruments and techniques have been developed which perform four-point probe and Hall effect measurements using probes with μm -scale spacing as described in detail elsewhere^{104,107,108,128}; these micro four-point probe (M4PP) and micro Hall effect (MHE) measurements have been shown to greatly reduce the effects of junction leakage^{104,125,126} and have previously been used for successful characterization of active shallow dopants in Ge.^{46,129}

In addition to the electrical characterization of ultra-shallow B⁺ implants, the chemical dose following ion implantation can not be assumed to be equal to the implanted dose due to ion-solid interactions reducing the total amount of implanted B. Due to the relatively light atomic mass relative to Ge, the B ions are highly susceptible to backscattering which is caused by elastic collisions between the implanted B⁺ and the target Ge matrix which expels B from the lattice (Figure 3-2). The effect of

backscattering is increased with reducing ion mass and ion energy which creates an environment primed for dose loss for ultra-shallow B⁺ implants into Ge. As shown in Figure 3-1, for a 2 keV B⁺ implant, greater than 20% of the implanted fluence is expected to be lost to backscattering in Ge while only 6% is lost for Si.⁷⁸ Due to the susceptibility of ultra-shallow B⁺ implants to backscatter, it is necessary to measure the residual chemical dose for accurate quantification of the implanted dopants.

Following implantation and annealing, it is also important to structurally determine the location of residual B atoms to fully understand the activation behavior. It has been shown previously that Ge is p-type immediately following B⁺ implantation with no annealing treatment.³³ Deep level transient spectroscopy (DLTS) characterization was used and it was determined that the p-type activation was due to implant damage related acceptor centers and not as-implanted substitutional B atoms. Nuclear reaction analysis (NRA) is an ion beam analysis technique that is able to determine the lattice location of B following implantation in Ge. In addition, the lattice location results obtained by using NRA are useful for corroborating electrical data if results are atypical.

In this chapter, the activation of low energy B⁺-implantation into c-Ge and PA-Ge was studied using M4PP and MHE measurements. Ion beam analysis techniques and transmission electron microscopy are used to further explain the electrical behavior observed upon annealing.

3.2 Experimental Details

Czochralski-grown n-type (001) wafers (resistivity ~ 50 Ωcm) were used for this work. A set of c-Ge samples was produced by B⁺ implantation at 2 keV to doses of $5.0 \times 10^{13} - 5.0 \times 10^{15} \text{ cm}^{-2}$ while a set of PA-Ge samples was produced by first performing Ge⁺-implantation at 120 keV to a dose of $2 \times 10^{14} \text{ cm}^{-2}$ before the same B⁺-implantation

step. In the case of PA-Ge samples, a continuous amorphous layer extending ~100 nm from the surface was produced as verified by high-resolution cross-sectional transmission electron microscopy (HR-XTEM). Samples were annealed in N₂ ambient at 400 °C for 1 h to activate the implanted B. HR-XTEM was used to image the microstructure of the specimens before and after annealing with samples prepared using focused ion beam (FIB) milling. Secondary ion mass spectrometry (SIMS) was performed on selected samples to determine B concentration profiles before and after annealing.

Sheet resistance, Hall sheet number (n_H), and Hall mobility (μ_H) were measured using a CAPRES microRSP M-150 M4PP with Au-coated probes, a probe spacing of 20 μm , and a permanent magnet with a magnetic flux density of 0.475 T. Hall sheet number and mobility values were adjusted to obtain the carrier sheet number (n_s) and drift mobility (μ_d) by using a scattering factor (r_H) of 1.21 as determined empirically by Mirabella *et al.* for high dose B⁺-implantation into Ge.³¹ The carrier density and drift mobility are related to the Hall values by $n_s = n_H \times r_H$ and $\mu_d = \mu_H / r_H$, respectively.

It has been speculated that a large fraction of the implanted B⁺ fluence is lost to ion backscattering.^{24,130} To characterize the as-implanted chemical dose of ultra-shallow B⁺ implants in Ge, a set of variable energy samples were implanted at 2, 4, and 6 keV and characterized using elastic recoil detection (ERD). Any losses due to backscattering would be independent of implanted dose; therefore, a dose of $5.0 \times 10^{15} \text{ cm}^{-2}$ was used to increase measurement counts and decrease experimentation time for all implant energies investigated. ERD characterization was performed using the ¹¹B (²⁸Si, ¹¹B) reaction with a 28 MeV Si⁴⁺ beam with the Ge target tilted at 75° from

incidence and a recoil angle of 30°. A 12 µm mylar foil was used to shield forward scattered Si ions and to allow the recoiled B atoms to enter the detector. The B counts enabled the calculation of the areal density of the implanted boron.¹²¹

Nuclear Reaction Analysis (NRA) is an ion beam technique to detect B atoms in Ge by measuring the yield of α particles from the reaction $^{11}\text{B}(p,\alpha)^8\text{Be}$.^{15,131–134} NRA and channelling measurements along the $\langle 100 \rangle$, $\langle 110 \rangle$ and $\langle 111 \rangle$ axes were performed using a proton energy of 650 keV on a set of B^+ implanted samples. The α particle detector was placed at 160° with respect to the incident beam direction and it was covered with a 10-µm-thick aluminised mylar film to prevent backscattered protons to reach the detector. A second detector was placed at 165° and was used to detect protons backscattered from Ge atoms and to perform the Ge sample alignment procedure. The normalized channelling yield χ (χ^{Ge} and χ^{B} , for host Ge and B atoms, respectively) is defined as the ratio of the yield obtained when the beam is oriented down a channelling axis to the yield obtained in a randomly oriented or amorphous crystal. χ^{B} is proportional to the fraction of B that is sitting in off-lattice positions. χ^{Ge} is a measure of the off-lattice Ge atoms with respect to a perfect crystal. If the off-lattice B atoms do not have a preferential position, then similar χ^{B} values will be detected along the main crystal axes. Given the measured χ^{B} values, the apparent substitutional fraction f_s is defined as:

$$f_s(B) = \frac{1 - \chi^{\text{B}}}{1 - \chi^{\text{Ge}}} \quad (3-1)$$

3.3 Characterization of Residual Implanted Dose

To confirm the residual implanted dose of ultra-shallow B^+ implants in Ge, samples as-implanted to a dose of $5.0 \times 10^{15} \text{ cm}^{-2}$ were characterized using ERD. The

residual implanted dose for samples implanted at 2, 4, and 6 keV was found to be $3.84 \times 10^{15} \text{ cm}^{-2}$, $3.88 \times 10^{15} \text{ cm}^{-2}$, and $4.12 \times 10^{15} \text{ cm}^{-2}$, respectively. The deviation from the implanted dose is significant as the loss is in excess of 20% of the implanted dose for the lowest implant energy. As speculated in previous reports, it is believed that ion backscatter is a large source of dose loss and at first inspection could seemingly reduce the activation of the B⁺ implant.²⁴ Due to the low atomic mass relative to Ge and the $1/E^2$ dependence of backscattering, boron is highly susceptible to ion backscattering during low-energy implantation which reduces the chemical dose before any other processing is completed. Taking into account that samples were characterized as-implanted, it is assumed that the deviation from implanted dose is due completely to backscattering losses during implantation. Boron is known to diffuse very slowly in Ge^{28–30} and no further significant dose loss is expected due to surface desorption following annealing at 400-600°C for 60 s.¹³⁵

Figure 3-2 shows the percentage of implanted B⁺ lost to backscattering as a function of implant energy as measured with ERD plotted in conjunction with SRIM simulations.⁷⁸ The simulations compare favorably with the dose loss values experimentally determined through ERD and confirm that a large fraction of the implanted dose is lost to ion backscattering. Given that backscattering is an energy-dependent phenomenon, it is assumed that this behavior is identical for lower doses. The experiment confirms that SRIM simulations are sufficient for estimating the retained implanted dose for ultra-shallow B⁺ implants in Ge.

3.4 Hall Effect Characterization

Figure 3-3 presents measured R_s and n_s values as a function of implanted B⁺ dose for both c-Ge and PA-Ge samples following annealing at 400 °C for 1 h. As shown

in Figure 3-3(a), the R_s value decreases with increasing B^+ dose for both c-Ge and PA-Ge samples with c-Ge samples exhibiting higher sheet resistance values compared to the PA-Ge samples. The reduced R_s values for the PA-Ge samples are explained by the increased solubility and B incorporation during SPEG as previously reported by others for different implant conditions.^{23,34,35} The carrier sheet number is plotted as a function of implanted B^+ dose for both c-Ge and PA-Ge samples after adjustment with a Hall scattering factor of 1.21 as shown in Figure 3-3(b); the PA-Ge samples exhibited higher n_s values compared to c-Ge samples, similar to previous reports.^{23,34,35} More interestingly, for B^+ doses less than $5.0 \times 10^{15} \text{ cm}^{-2}$, the percent activation for both c-Ge and PA-Ge samples is relatively independent of dose at ~ 7 and ~ 30 %, respectively. At a dose of $5.0 \times 10^{15} \text{ cm}^{-2}$, the difference in percent activation is much smaller, ~ 10 and 15 % for c-Ge and PA-Ge samples, respectively. Figure 3-4 shows HR-XTEM images of a c-Ge sample B^+ -implanted at 2 keV to a dose of $5.0 \times 10^{15} \text{ cm}^{-2}$. As shown in Figure 3-4(a), a damage layer extending 18 ± 0.5 nm from the surface is evident, which matches well with the expected range²⁴ of the implant. At higher magnifications, as shown in Figure 3-4(b), amorphous pockets are evident within the damaged layer. Thus, the smaller difference in R_s between c-Ge and PA-Ge for the case of a B^+ dose of $5.0 \times 10^{15} \text{ cm}^{-2}$ is likely due to enhanced incorporation of substitutional B within the amorphous regions during SPEG upon annealing.

To better understand the activation behavior, samples B^+ -implanted to doses of 5.0×10^{13} and $5.0 \times 10^{15} \text{ cm}^{-2}$ into c-Ge and PA-Ge were analyzed using SIMS before and after annealing to determine B concentration profiles, as shown in Figure 3-5. The measured B concentration profiles (both before and after annealing) were very similar to

as-implanted simulations.⁷⁸ The lack of dopant diffusion is in excellent agreement with previous reports.³⁴ The maximum active concentration was estimated using the SIMS profile and the corresponding measured n_s values presented in Figure 3-2(B). For c-Ge and PA-Ge samples B⁺-implanted to a dose of $5.0 \times 10^{15} \text{ cm}^{-2}$, the maximum active B concentrations were estimated at 2.0×10^{20} and $4.0 \times 10^{20} \text{ cm}^{-3}$, respectively; the value for PA-Ge is similar to prior results while the results for c-Ge are the highest reported.^{23,31,34,35,46,123}

The observed activation behavior for both c-Ge and PA-Ge samples is very interesting; incomplete activation is observed for even the lowest B⁺ fluences in both sample sets. Based on the reported maximum active B concentration of $5.5 \times 10^{20} \text{ cm}^{-3}$ ³¹, full activation should be expected for B⁺-implantation at 2 keV to a dose of $5 \times 10^{13} \text{ cm}^{-2}$ for both c-Ge and PA-Ge, yet the measured percent activation in each case was ~7 and ~30 %, respectively. It should be further noted that this behavior implies that a single electrical solubility limit does not exist for these shallow implants in Ge. This is unexpected and may have resulted from chemical dose loss or a unique dopant clustering/precipitation that scales with B⁺ fluence. Boron is not known to diffuse readily or suffer dose loss through the surface upon annealing at 400°C and is thus not expected to be a contributor to the reduction of active carriers.^{28–30}

One contributing factor for the low levels of activation could be due to the shallow nature of the implant, even slight surface oxidation is capable of consuming a non-negligible portion of the implanted B⁺ dose. HR-XTEM analysis revealed the presence of a $3.0 \pm 0.2 \text{ nm}$ -thick surface oxide on all as-implanted samples, as shown in Figure 3-3. As per simulations⁷⁸, ~8 % of the implanted dose is rendered inactive via the

presence of a GeO_x layer of this thickness. Finally, it should be noted that the percent of dose rendered inactive due to both oxidation and ion backscattering should be independent of implanted dose; however, the combination of losses due to backscattering and surface oxidation can only account for ~28% of dose loss. Thus, the bulk of the inactive fraction cannot be explained by these factors.

Another possible source of inactive B is due to the formation of an inactive cluster or complex, which has been observed and extensively studied in Si.^{13,67} In the case of Si, for a given processing condition, full activation is expected for low B^+ doses until a certain concentration threshold is reached after which clustering occurs. However, for the presented data, incomplete activation is observed even for the lowest B^+ dose with the percent activation remaining relatively constant with increasing dose for doses $< 5.0 \times 10^{15} \text{ cm}^{-2}$. Work by Impellizzeri *et al.*³⁷ revealed incomplete activation for B^+ -implantation at 35 keV into c-Ge, which was attributed to the formation of a B-Ge cluster; however, incomplete activation observed in this work is much more pronounced and is observed in both c-Ge and PA-Ge samples. The physical explanation behind the observed anomalous activation behavior is unclear; however, the close proximity of the surface is a possible contributing factor, since it is known that defect production and annihilation can be influenced by surface proximity.¹³⁶ Sample characterization using structural techniques is necessary to corroborate the electrical data and to gather further data regarding the anomalous activation behavior.

3.5 Nuclear Reaction and Channeling Analyses

It is expected that the formation of an inactive complex would be dependent on the implanted fluence or overall B concentration with respect to a solubility limit. If the B concentration were to exceed this limit, clustering and inactive dopants would be

expected; below this limit, substitutional and active dopants would be the case. This behavior is what is typically observed for dopant implantation and activation in Si. It should be noted that this behavior is much different from what has been reported previously regarding B clustering in Ge^{34,37-39} for two reasons: 1. Although not as prominent, dose-independent clustering also occurred in ultra-shallow B⁺ implants in PA-Ge and 2. The behavior is independent of fluence and the activation percentage is fixed even for a 5.0×10^{13} B⁺-cm⁻² implant for both c-Ge and PA-Ge. Since the electrical activation behavior deviates far from what has been observed previously in Ge as well as in Si, select samples were structurally characterized through channeling analyses utilizing nuclear reactions to determine the substitutional fraction of B after processing.

Table 3-1 shows the fraction of substitutional B as measured using channeling and NRA following a 400°C 60s anneal. For both c-Ge and PA-Ge, low and high fluence samples were characterized to obtain structural data on samples that would be expected to be below and above electrical solubility, respectively. For all characterized samples, the normalized channeling yield (χ^B) obtained along the <100>, <110>, and <111> orientations are all approximately equal. This suggests that the non-substitutional B fraction is randomly distributed throughout the lattice. The substitutional fraction for each sample was obtained by using Equation 3-1 and averaging the channeling yield obtained along each crystal orientation. The substitutional fractions obtained using channeling analyses and electrical measurements agree favorably for all characterized samples. For even a modest B⁺ fluence of 1.0×10^{14} cm⁻² (peak B concentration of approximately 6.0×10^{19} cm⁻³)⁷⁸, the substitutional fractions as measured by Hall and channeling analyses are in agreement at approximately 10%.

The data obtained from NRA and channeling analyses confirm the efficacy of electrical measurements of ultra-shallow B⁺ implants in Ge and suggest that electrical results obtained using different processing conditions, ie different implant fluences or annealing thermal budgets, should be considered to be accurate.

3.6 Summary

In summary, residual implanted dose following ultra-shallow B⁺ implantation was characterized using ERD and is in good agreement with values obtained through Monte Carlo simulations. The results permit the use of SRIM simulations for the evaluation of backscattering loss. The activation of B⁺-implantation at 2 keV into crystalline and pre-amorphized Ge was studied using micro four-point probe and micro Hall effect measurements. For B⁺ doses of $5.0 \times 10^{13} - 5.0 \times 10^{15} \text{ cm}^{-2}$, pre-amorphized samples exhibited greater activation compared to crystalline samples following a 400 °C anneal for 1 h. In the case of B⁺-implantation to a dose of $5.0 \times 10^{15} \text{ cm}^{-2}$, the discrepancy in activation between crystalline and pre-amorphized samples was much smaller; this was attributed to solid-phase epitaxial growth within amorphous pockets formed in crystalline samples as a result of only B⁺-implantation.

Notably, for both crystalline and pre-amorphized samples, the measured percent activation was approximately independent of implanted dose; this behavior is in stark contrast to reported activation behavior of shallow B⁺-implantation in Si and deeper B⁺-implantation in Ge. In conjunction with Hall measurements, samples were characterized using NRA and have determined that a large fraction of the residual implanted fluence is off-lattice and electrically inactive. It should be noted that these activation values are well below reported electrical solubility. These results suggest the possibility of the formation of a dose-independent B-Ge cluster which is unique to ultra-

shallow B^+ -implantation in Ge; the physical explanation of this anomalous behavior is unclear, though the close proximity of the surface and reduced B^+ implant energy may be a contributing factor.

Table 3-1. Channeling yields and corresponding substitutional B fractions as measured by channeling analysis using nuclear reactions along three axes (<100>, <110>, and <111>) and Hall effect measurements after annealing 400°C for 60s.

	B ⁺ Fluence (/cm ²)	$\chi_B<100>$	$\chi_B<110>$	$\chi_B<111>$	NRA ^a	Hall ^b
c-Ge	1.0×10 ¹⁴	0.92±0.05	0.90±0.05	0.91±0.05	9.0	11.9
c-Ge	1.0×10 ¹⁵	0.81±0.01	0.83±0.01	0.84±0.01	18.3	12.0
c-Ge	5.0×10 ¹⁵	0.91±0.01	0.89±0.01	0.92±0.01	11.0	11.7
PA-Ge	1.0×10 ¹⁵	0.41±0.01	0.39±0.01	0.43±0.01	62.0	53.9
PA-Ge	5.0×10 ¹⁵	0.76±0.01	0.75±0.01	0.79±0.01	24.6	19.0

^a Determined by averaging χ^B values from <100>, <110>, and <111> orientations

^b Ratio of carrier sheet density divided by the residual fluence

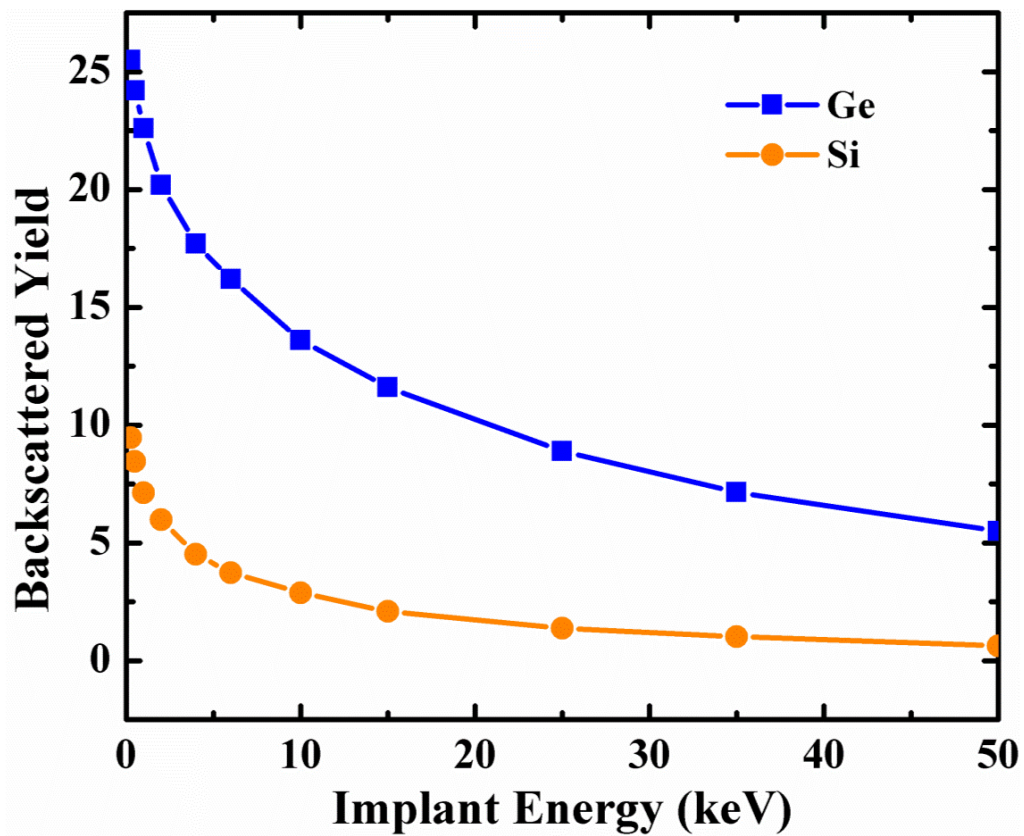


Figure 3-1. The effect of B⁺ backscattering for implantation into Ge and Si as simulated by SRIM.

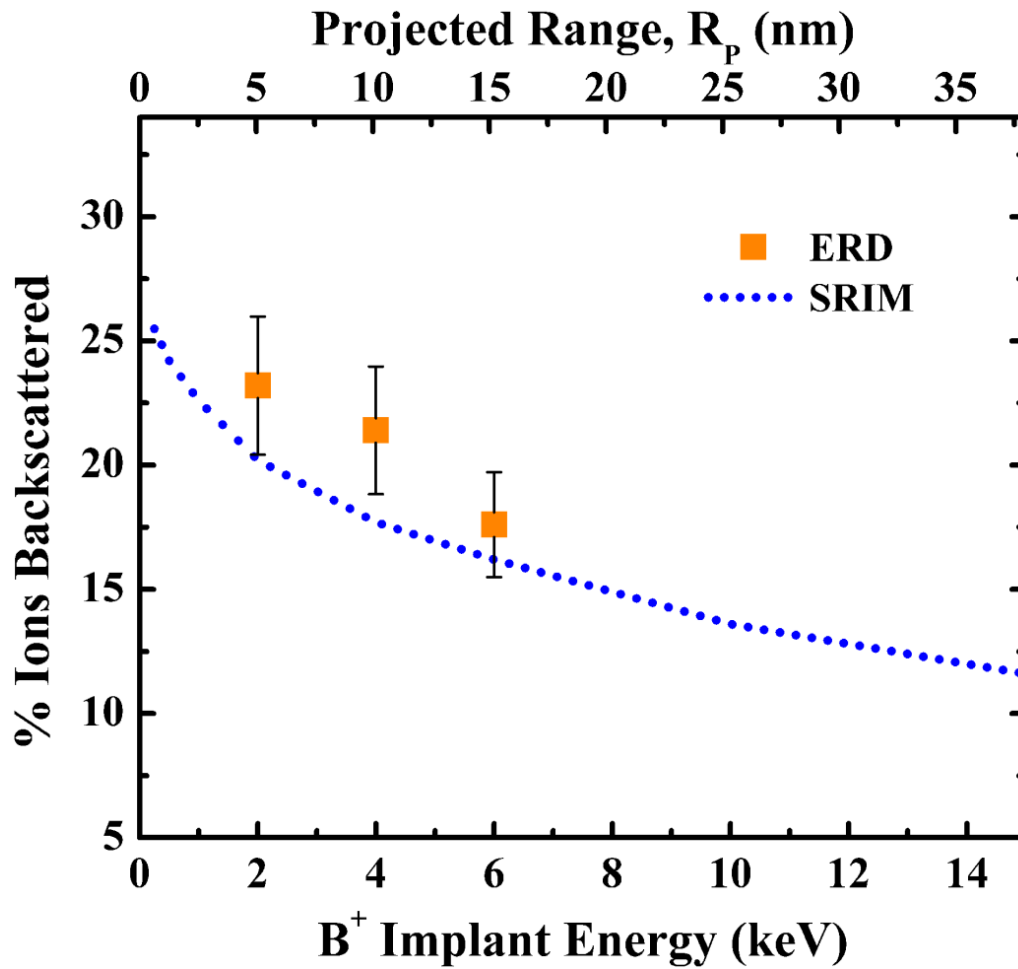


Figure 3-2. Percent of B ions backscattered as a function of implant energy into Ge as simulated by SRIM and experimentally determined through ERD for a $5.0 \times 10^{15} \text{ cm}^{-2}$ implant into Ge.

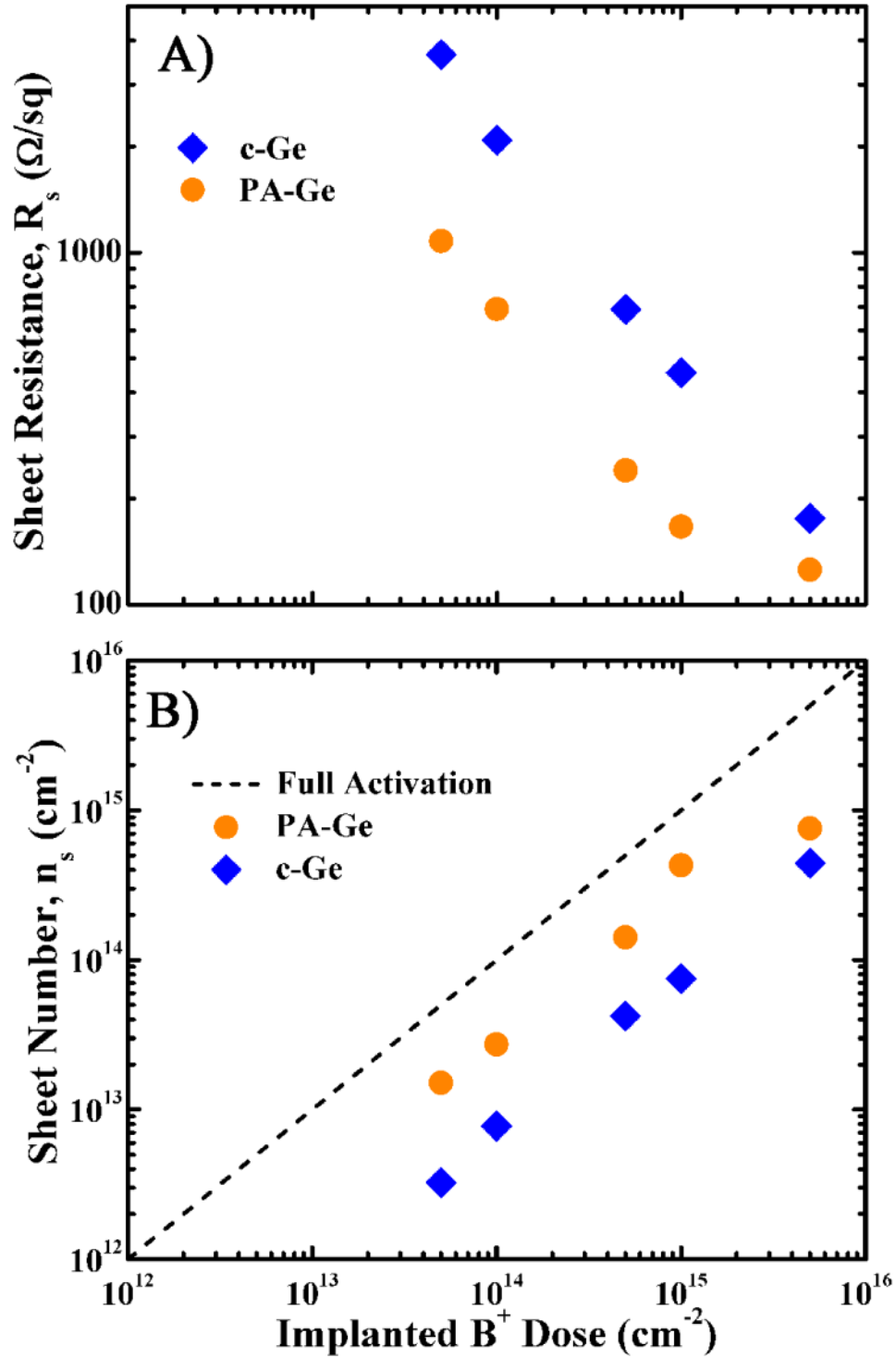


Figure 3-3. Electrical characteristics as a function of B⁺ fluence implanted at 2 keV into crystalline and preamorphized Ge, respectively, after annealing at 400°C for 1h. A) Measured sheet resistance (R_s) and B) sheet number (n_s) as a function of B⁺ dose implanted

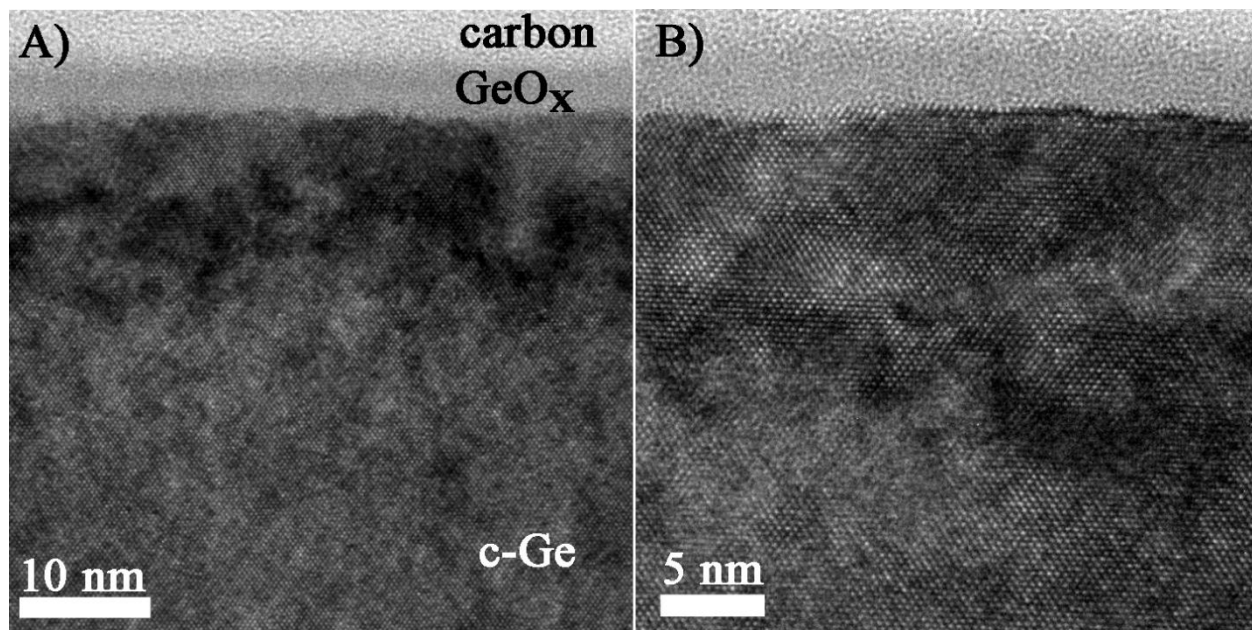


Figure 3-4. HR-XTEM micrographs of a crystalline Ge sample B⁺ implanted at 2 keV to $5.0 \times 10^{15} \text{ cm}^{-2}$ as-implanted in c-Ge showing: A) a surface GeO_x layer and a damaged layer extending 18 nm from surface and B) amorphous pockets and lattice defects in close proximity to the surface.

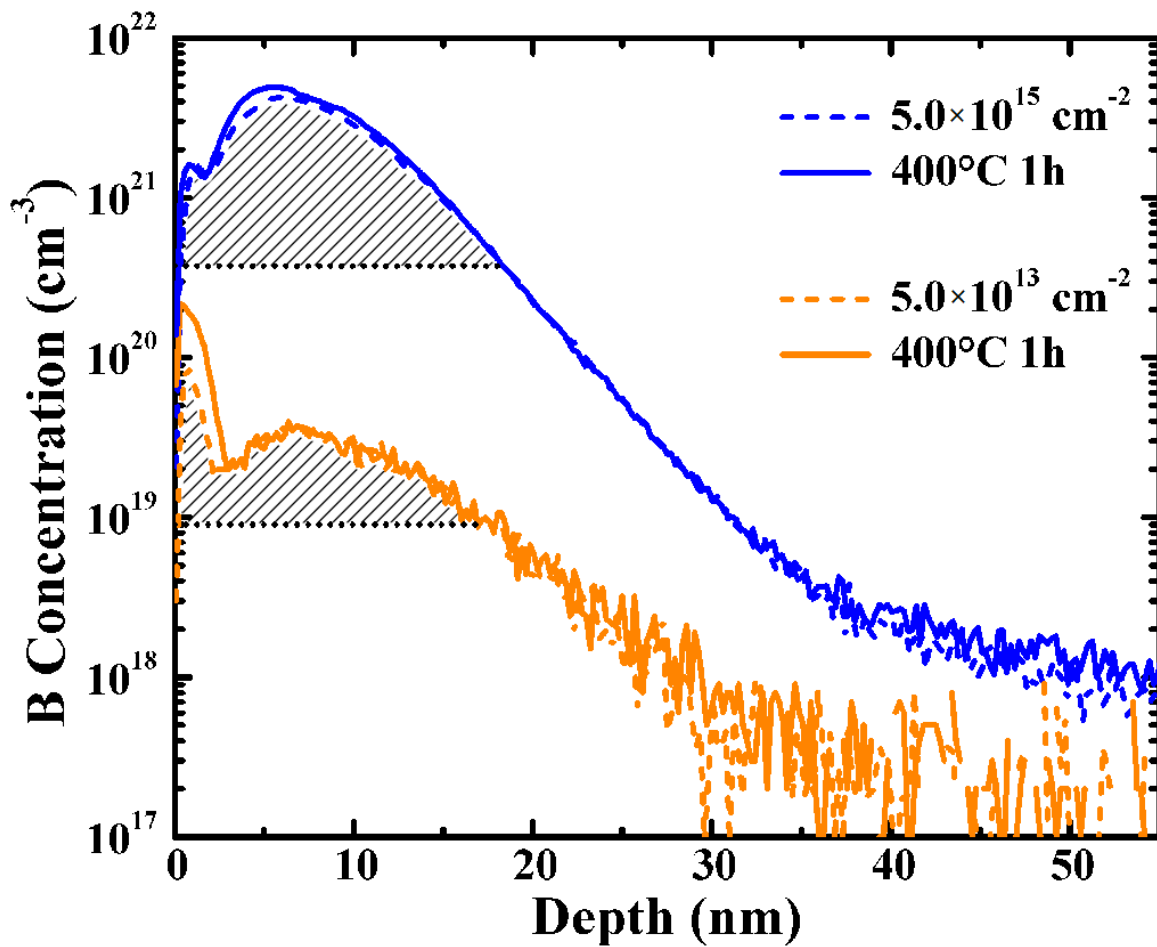


Figure 3-5. B concentration profiles of a pre-amorphized Ge sample B⁺-implanted at 2 keV to doses of 5.0×10^{13} or $5.0 \times 10^{15} \text{ cm}^{-2}$ as-implanted (dashed line) and after annealing at 400 °C for 1 h (solid line) as measured using SIMS. The horizontal dotted lines indicate the estimated maximum active B concentration for both implant conditions.

CHAPTER 4 EFFECT OF IMPLANT ENERGY ON B ACTIVATION

4.1 Low Energy B⁺ Implantation in Ge

This work is the first report of the anomalous activation behavior observed for shallow B⁺ implants in c-Ge and PA-Ge which raises the question as to why it has not been observed previously. A minute body of research exists regarding the electrical behavior of shallow B⁺ implants in Ge which may explain how this behavior has gone unnoticed. In addition, the experiments that have been completed typically measured sheet resistance of a single sample or small sample set implanted to a high fluence which does not yield significant information regarding carrier activation.^{34,38,40,45} The use of a single high fluence implant is capable of masking the incomplete activation observed for low energy implants in this work by pushing the peak concentration well above electrical solubility values reported in the literature.

To further understand the fluence-independent activation behavior of B in Ge, a systematic study of increasing implant energy as a function of fluence is necessary. In this chapter, the activation of low energy B⁺-implantation into c-Ge and PA-Ge was studied using M4PP and MHE measurements. The effect of increasing B⁺ implant energy and its effect of increasing point defect formation is studied. The consequence of increasing the distance between the surface and the B profile on electrical activation is also investigated.

4.2 Experimental Details

Czochralski-grown n-type (001) wafers (resistivity ~ 50 Ωcm) were used for these experiments. A set of c-Ge samples was produced by B⁺ implantation at 2, 4, and 6 keV to doses of $5.0 \times 10^{13} - 5.0 \times 10^{15} \text{ cm}^{-2}$ while a set of PA-Ge samples was produced

by first performing Ge⁺-implantation at 120 keV to a dose of $2 \times 10^{14} \text{ cm}^{-2}$ before the same B⁺-implantation step. Samples were annealed in N₂ ambient at 400 °C for 60s to activate the implanted B.

Sheet resistance, Hall sheet number (n_H), and Hall mobility (μ_H) were measured using a CAPRES microRSP M-150 M4PP with Au-coated probes, a probe spacing of 20 μm , and a permanent magnet with a magnetic flux density of 0.475 T. Hall sheet number and mobility values were adjusted to obtain the carrier sheet number (n_s) and drift mobility (μ_d) by using a scattering factor (r_H) of 1.21 as determined empirically by Mirabella *et al.* for high dose B⁺-implantation into Ge.³¹ The carrier density and drift mobility are related to the Hall values by $n_s = n_H \times r_H$ and $\mu_d = \mu_H / r_H$, respectively.

4.3 Effect of Increased B⁺ Implant Energy

Figure 4-1 shows profiles for 2, 4, and 6 keV B⁺ implants to a fluence of $5.0 \times 10^{13} \text{ cm}^{-2}$ as simulated using SRIM.⁷⁸ The profiles show that as B⁺ implant energy is increased, the B profile is pushed further from the surface as well as broadened. In doing so, the peak B concentration is reduced. A fluence of $5.0 \times 10^{13} \text{ cm}^{-2}$ was simulated to show that the majority of the B concentration is below the reported electrical solubility of B in Ge for the low fluence implants. The maximum reported electrical solubility of B in c-Ge is approximately $2.0 \times 10^{20} \text{ cm}^{-3}$ as reported in the previous chapter.

Figure 4-2 shows the sheet resistance (R_S) for samples implanted at 2, 4, and 6 keV to B⁺ fluences ranging from 5.0×10^{13} to $5.0 \times 10^{15} \text{ cm}^{-2}$ after annealing for 400°C for 60s. In Figure 4-2(A) and 4-2(B), it is evident that R_S decreases with increasing fluence and energy for both c-Ge (diamonds) and PA-Ge (circles). Following a 400°C 60s anneal, the minimum R_S achieved was 45.9 and 105.9 Ω/sq for PA-Ge and c-Ge,

respectively. The lower R_S values for PA-Ge with respect to c-Ge have been documented previously^{6,15,20} and are due to increased B incorporation upon SPEG. The decrease in R_S with increasing implant energy can be explained by the increase in the fraction of implanted B with a concentration below the solubility limit. SRIM simulations show that the projected range of the implant shifts from 9.5 to 24.0 nm as the implant energy is increased from 2 to 6 keV. In doing so, the B peak widens at higher energies and allows for a larger fraction of dopant activation for identical fluences. The B concentration profiles following B⁺ implantation to a fluence of $5.0 \times 10^{13} \text{ cm}^{-2}$ is shown in Figure 4-1. It should be noted that the fluence used for this figure is only for representation of the effect of energy as similar behavior would be observed for increased or decreased B⁺ fluence.

In Figure 4-3(A) and 4-3(B), sheet number (as adjusted using $r_H = 1.21$) is plotted as a function of implant fluence. It is evident that the decrease in R_S with increasing fluence is due to an increase in the overall number of active dopants. With increasing implant energy, a larger fraction of implanted dopant is incorporated into the lattice for reasons described in the previous paragraph. For $5.0 \times 10^{15} \text{ B}^+ \text{-cm}^{-2}$ implants at 6 keV, the n_s obtained was 7.4×10^{14} and $2.2 \times 10^{15} \text{ cm}^{-2}$ for c-Ge and PA-Ge, respectively. The corresponding activation value, defined as the ratio of sheet number divided by the residual implanted fluence, was 18 and 52% for c-Ge and PA-Ge, respectively. These low activation values are not entirely surprising given the peak B concentration, which was simulated by SRIM to be approximately $1.4 \times 10^{21} \text{ cm}^{-3}$ and thus is well above solubility values reported in the literature.^{24,31,34}

Figure 4-4 (A) and 4-4 (B), the drift mobility (as adjusted using $r_H = 1.21$) is plotted as a function of B⁺ implant fluence for both c-Ge and PA-Ge samples. It can be seen that drift mobility is higher for c-Ge with respect to PA-Ge samples across the investigated range. In addition, the data shows a trend of decreasing mobility with increasing B⁺ fluence. Comparing this data with the sheet number values in Figure 4-3 (A) and 4-3 (B), these trends can be explained by the increase in the number of active dopants for these conditions as ionized carriers exhibit a stronger effect on carrier mobility than neutral dopant atoms.

In conjunction with the anomalous activation behavior of ultra-shallow B⁺ implants in Ge that has been reported previously,²⁴ a large discrepancy between the implanted and active fluence exists for both c-Ge and PA-Ge. For the lowest B⁺ fluence of $5.0 \times 10^{13} \text{ cm}^{-2}$ implanted at 2 keV, the peak B concentration as simulated by SRIM⁷⁸ is expected to be only $3.0 \times 10^{19} \text{ cm}^{-3}$ which is lower than the reported solubility of B in both c-Ge and PA-Ge.²⁴ Despite the low concentration, only a small fraction of dopant is rendered active following a 400°C anneal for 60s. The short annealing time is not the source of poor activation as previous reports have shown that 400°C for 1h have yielded similar results.²⁴ The decrease from complete activation is not due to any electrical solubility argument.

The large concentration of inactive B observed in c-Ge and PA-Ge is well-behaved across the investigated energy range and is intriguing due to its fluence-independent nature. The sheet number values obtained increase as a function of energy which suggests that inactivity may increase when the boron profile is located near the surface.

With decreasing implant energy, the concentration profile shifts towards the surface as shown in Figure 4-1. This increases the concentration of B above the solubility limit and also reduces the activation of B. The simulated concentration profile and the measured sheet number were used to determine the corresponding maximum active B concentration as described elsewhere.³⁴ For the highest fluence across all B⁺ energies investigated, the average active concentration was determined to be $1.3 \pm 0.3 \times 10^{20}$ and $4.5 \pm 0.5 \times 10^{20}$ B-cm⁻³ for c-Ge and PA-Ge and correlates well with values in the literature.^{23,24,31,34}

However, it needs to be stressed that the inactivity exhibited for these ultra-shallow B⁺ implants is not due to electrical solubility constraints. Completing the same procedure for the 5.0×10^{10} cm⁻² fluence returns an electrical solubility value well below the lowest reported electrical solubility values. This suggests that the activation behavior of these ultra-shallow B⁺ implants in Ge do not follow traditional electrical solubility rules in which all dopant above the solubility concentration is inactive while all dopants below the solubility concentration is electrically active. Rather, the observed behavior suggests that B activation is dependent on the local B concentration in which the electrical solubility limit mimics the chemical dopant profile decreased by a factor less than unity.

4.4 Role of Implant Energy

To investigate the effect of increasing implant energy, the electrical activation values obtained by variable B energy implants into c-Ge to a fluence of 5.0×10^{14} cm⁻² following annealing at 400°C for 60s were used. Data from Bruno *et al.*²³ and Suh *et al.*³⁶ which used 35 keV and 60 keV B⁺ implants, respectively, is used to gain further insight into the effect of implant energy and surface proximity. Indeed, increasing the

implant energy while implanting a fixed fluence widens the B profile and decreases the peak concentration. However, it has been shown previously in this work that the fraction of electrically active dopant atoms is approximately constant as a function of fluence and not a function of electrical solubility which is typically invoked for implants into Si. In addition, the effect of varying annealing conditions is not expected to change activation values appreciably as will be discussed in the following chapter.

The activation results as a function of variable B energy is plotted in Figure 4-5. It is evident that activation is observed to strongly increase for the ultra-shallow implants completed in this work. However, upon fitting the low energy implants to the data obtained from other works, it is evident that the increase in activation observed with increasing energy begins to level off. Extrapolating the fit, complete activation is not expected until an implant energy of approximately 190 keV is used. It should also be noted that this fit predicts 0% activation as the B⁺ energy approaches 0 keV. However, this finding is not entirely unreasonable if the surface truly is a sink for vacancies which would create the greatest interstitial super saturation as the B energy approaches 0 keV.

Similar results of surface proximity have been reported by Priolo *et al.* for low energy B⁺ implants into Si. Figure 4-6 shows a representation of the percentage of electrically active B atoms as a function of the implant R_p for a fixed fluence of $1.0 \times 10^{13} \text{ cm}^{-2}$. It is evident that a sharp decrease in electrical activation is evident for low energy implants. The authors were able to show that high-energy Si implants used to enrich the surface with vacancies were successful in increasing the activation of these low-energy implants by a factor of 2.5. Successive high energy Si⁺ implants were

successful in further increasing the B activation. Therefore, this behavior of incomplete activation for low-energy B⁺ implants in Si was attributed to a decrease in the vacancy population in the near-surface region which increased the formation of inactive B-complexes.¹³⁷

In recent publications, it has been shown that the Ge surface may act as a sink for vacancies while reflecting interstitials. In work by Bracht *et al.*, B-doped layers grown by MBE showed no change as a function of proximity to the surface during annealing. Simulations of the diffused B profile showed that a homogenous interstitial supersaturation existed. Conversely, P profiles showed a reduction of diffusion during proton irradiation. Considering that B and P diffuses through interstitial and vacancy mechanisms, respectively, it can be concluded that the near-surface region may be an interstitial-rich environment following implantation.⁵⁰

Other work by Scapellato *et al.* have also concluded that the Ge surface does not allow for interstitial recombination through the use of diffusion studies of B-doped layers grown by MBE.⁵⁴ In this work, B-doped Ge layers were implanted with oxygen at 235 keV to a fluence of $4.0 \times 10^{14} \text{ cm}^{-2}$ which has an R_p of approximately 500 nm. Following annealing at 650°C for various times, it was shown that B profiles diffused homogeneously for times less than and equal to 120 min through a form of enhanced diffusion due to oxygen precipitation. From these results, it was suggested that the homogeneous B diffusion further proves that the surface does not allow for interstitial recombination, but rather reflects them to the bulk.⁵⁴

In addition to increasing the distance from the surface, increasing the B⁺ implant energy also increases the number of vacancies created during implantation. As the B ion comes to rest, it loses its energy to the lattice through nuclear collisions which result in the creation of target vacancies and interstitials. If the B ion energy is increased, the amount of energy lost to nuclear collisions, and therefore the creation of point defects, increased.

Figure 4-7 displays the number of vacancies created per incoming B ion for variable energy B⁺ implantation in Ge as simulated by SRIM.⁷⁸ The observed increase in activation with increasing energy could also be attributed to the introduction of a larger vacancy population. For an off-lattice B atom to become electrically active, it must recombine with a lattice vacancy. By increasing the implant energy, the number of vacancies created is increased which increases the probability that an off-lattice B atom will react with a vacant.

It should also be mentioned that the Ge surface is known to undergo a radical transformation into a nanoporous structure following high-dose implantation.¹³⁸⁻¹⁴² This structure is attributed to a barrier between interstitial-vacancy recombination and the formation of vacancy clusters that increase in size with fluence.^{141,143} Although high-dose Ge⁺ implants were not used in this work, the effects of this barrier to interstitial-vacancy recombination may still be affecting the activation results. It has been shown that Ge⁺ implants to a fluence of $2.0 \times 10^{15} \text{ cm}^{-2}$ at energies from 30 to 120 keV were not observed to create the nanoporous structure, but SPEG was slowed near the surface.¹⁴⁴ The reduction of SPEG velocity was increased as the energy of the implant was reduced. Despite the lack of porous formation, the reduction of SPEG velocity was

attributed to the presence of sub-microscopic voids formed due to the barrier of interstitial-vacancy recombination in the near-surface region.¹⁴⁴

By increasing the implant energy, the effect of surface proximity is reduced; however, the number of vacancies created is also increased. Both of these properties may explain the increase in activation observed in this work for B⁺ implants at an energy between 2 and 6 keV. Although clustering has been previously observed for 35 keV B⁺ implants in Ge in which approximately 50% of implanted B was rendered active,^{37,39} the quantity of inactive B is much more significant for ultra-shallow implants as exhibited in this work. The work presented here is the first systematic report of ultra-shallow B activation in Ge which may explain why this phenomenon has not been observed previously. The results suggest that the role of implant energy has a significant effect on the electrical activation of shallow B⁺ implants in Ge.

4.5 Summary

In this chapter, it has been shown that moderate increases in the percentage of activated dopants occurs with increasing B⁺ implant energy. However, as was observed in the previous chapter, for a fixed implant energy, activation remains relatively independent of implanted B⁺ fluence.

The surface proximity and associated point defect populations was speculated to have an impact on B activation as increasing implant energy deepens the B profile from the surface. For a B⁺ implant to a fluence of $5.0 \times 10^{13} \text{ cm}^{-2}$, the percent of electrically active dopants as determined through micro Hall effect was found to be 10.1, 18.5 and 25.1% at an energy of 2, 4, and 6 keV, respectively. Given these implant conditions, the peak B concentration investigated is approximately $3.0 \times 10^{19} \text{ cm}^{-2}$ for the 2 keV implant and decreases with increasing implant energy. Full activation would be

expected for all of the investigated energies. As such, it has been determined that the effect of increasing activation with increasing implant energy is due to the creation of a larger vacancy population as well as the B profile being further removed from the surface and thereby reducing its effects on vacancy annihilation.

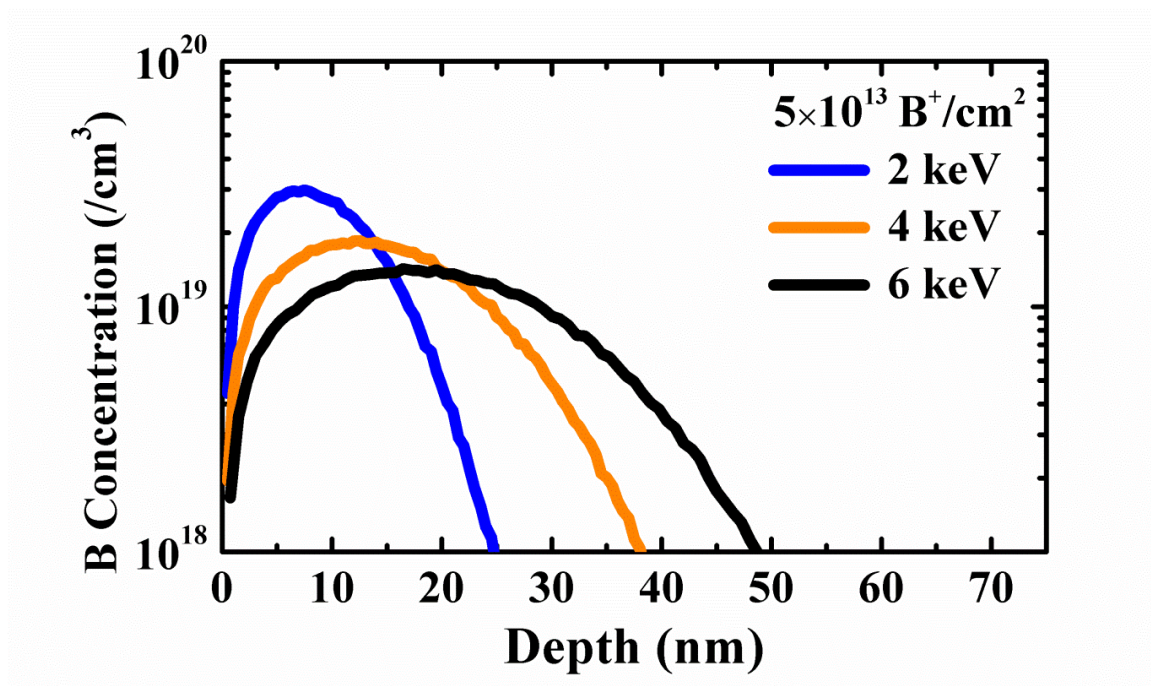


Figure 4-1. SRIM simulations depicting the shift in the B concentration profile produced with increasing implant energy.⁷⁸

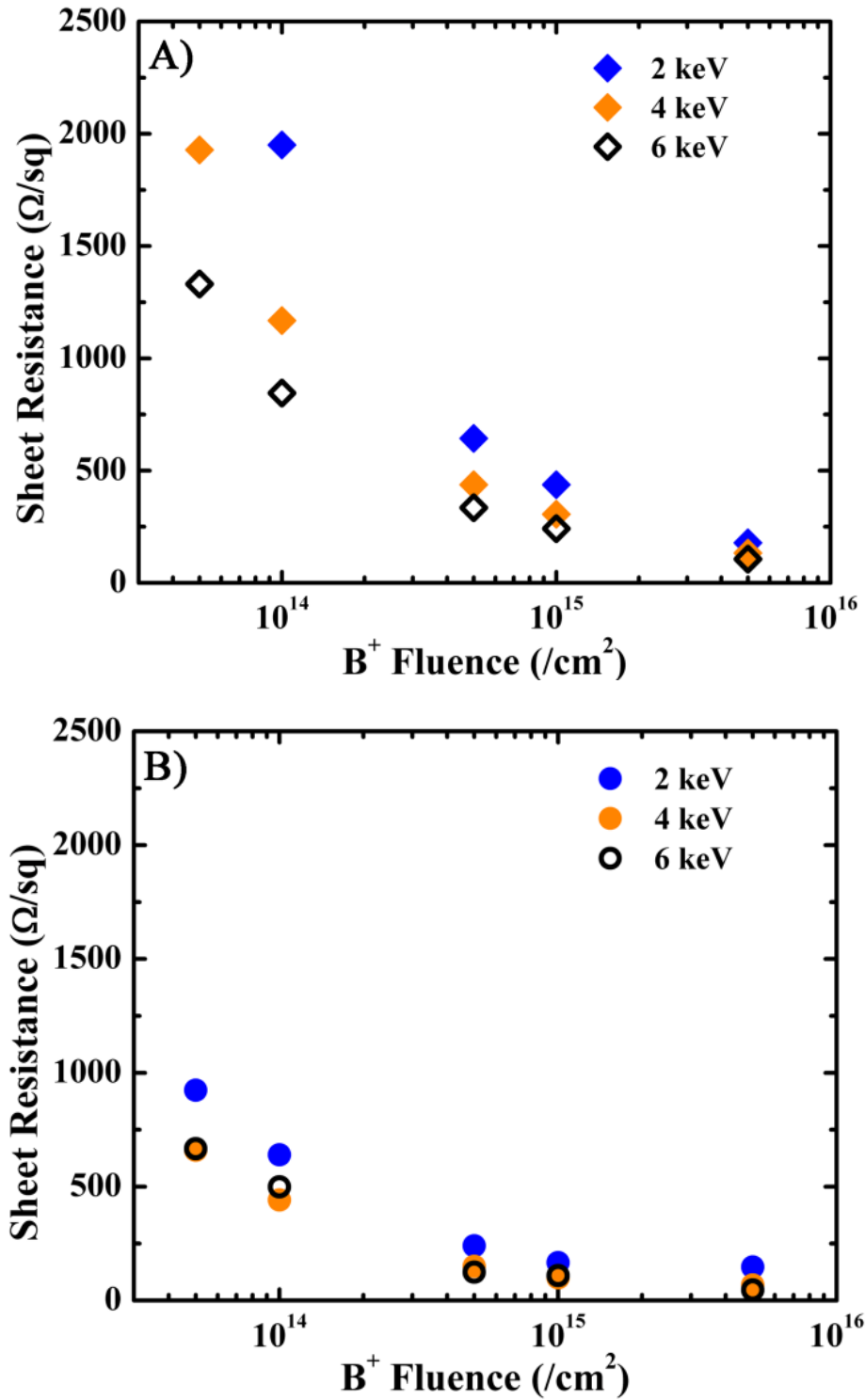


Figure 4-2. Measured sheet resistance of samples B⁺ implanted at 2, 4, and 6 keV to fluences ranging from 5.0×10¹³ to 5.0×10¹⁵ cm⁻² after annealing 400°C 60s in A) c-Ge and B) PA-Ge.

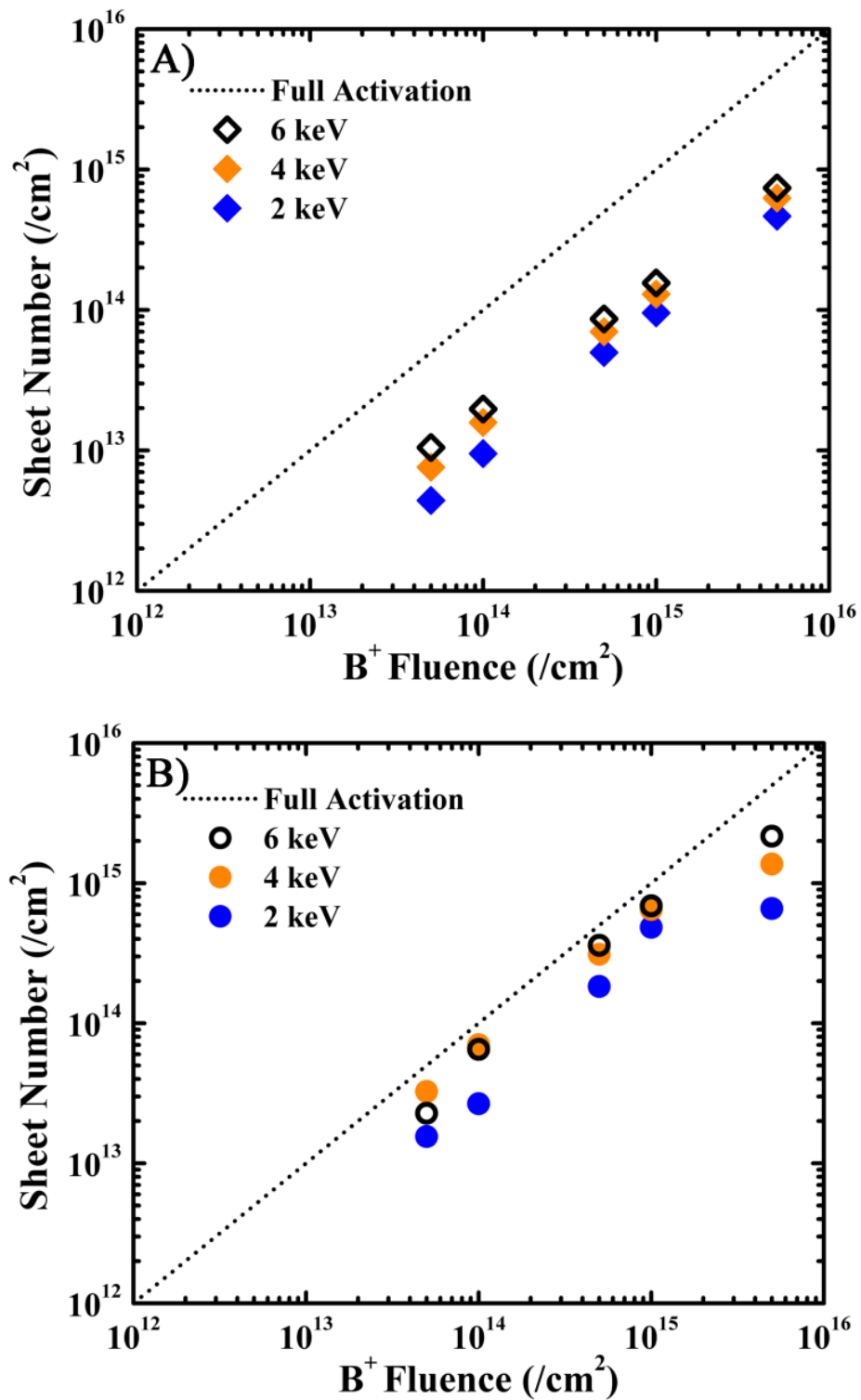


Figure 4-3. Measured sheet number of samples B⁺ implanted at 2, 4, and 6 keV to fluences ranging from 5.0×10¹³ to 5.0×10¹⁵ cm⁻² after annealing 400°C 60s. The dotted line represents complete activation for A) c-Ge and B) PA-Ge.

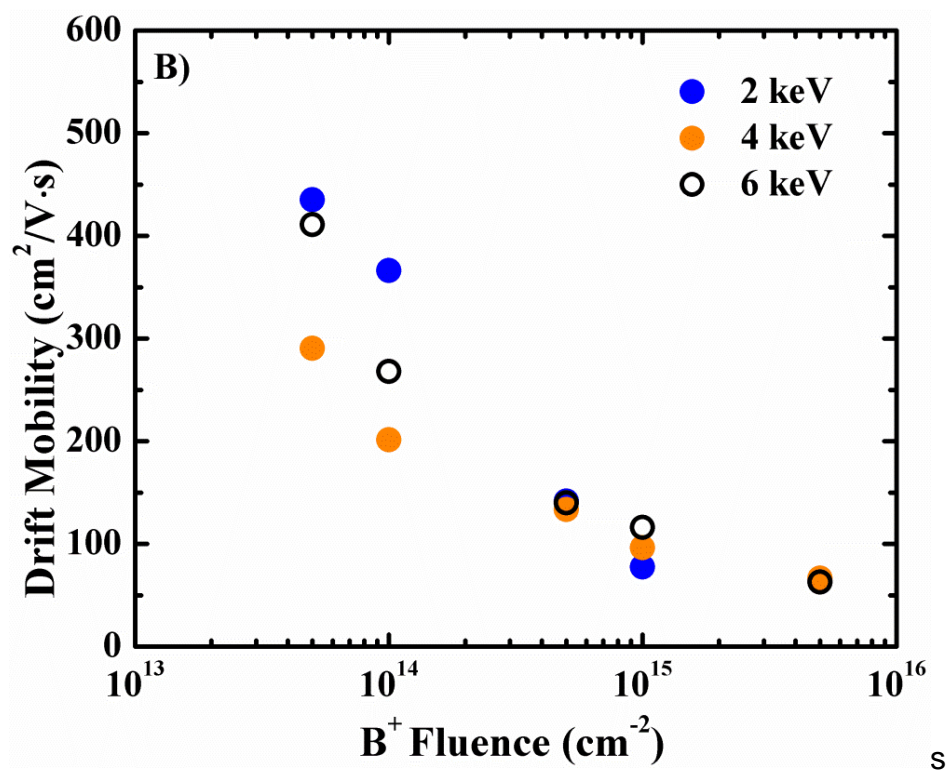
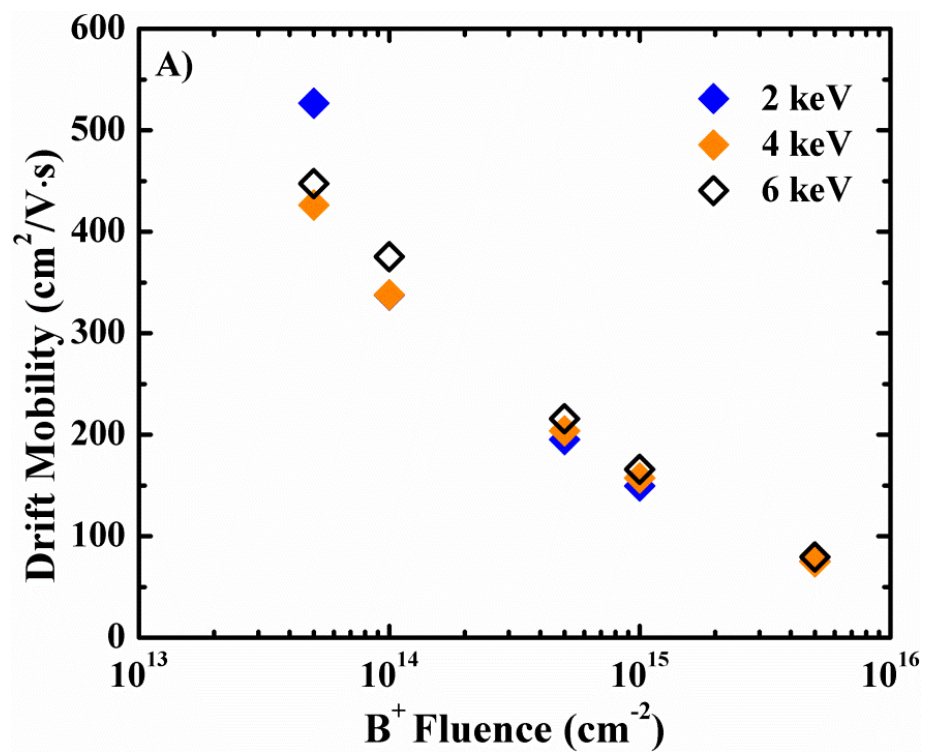


Figure 4-4. Measured drift mobility of samples B⁺ implanted at 2, 4, and 6 keV to fluences ranging from 5.0×10^{13} to $5.0 \times 10^{15} \text{ cm}^{-2}$ after annealing 400°C 60s. The dotted line represents complete activation A) c-Ge and B) PA-Ge.

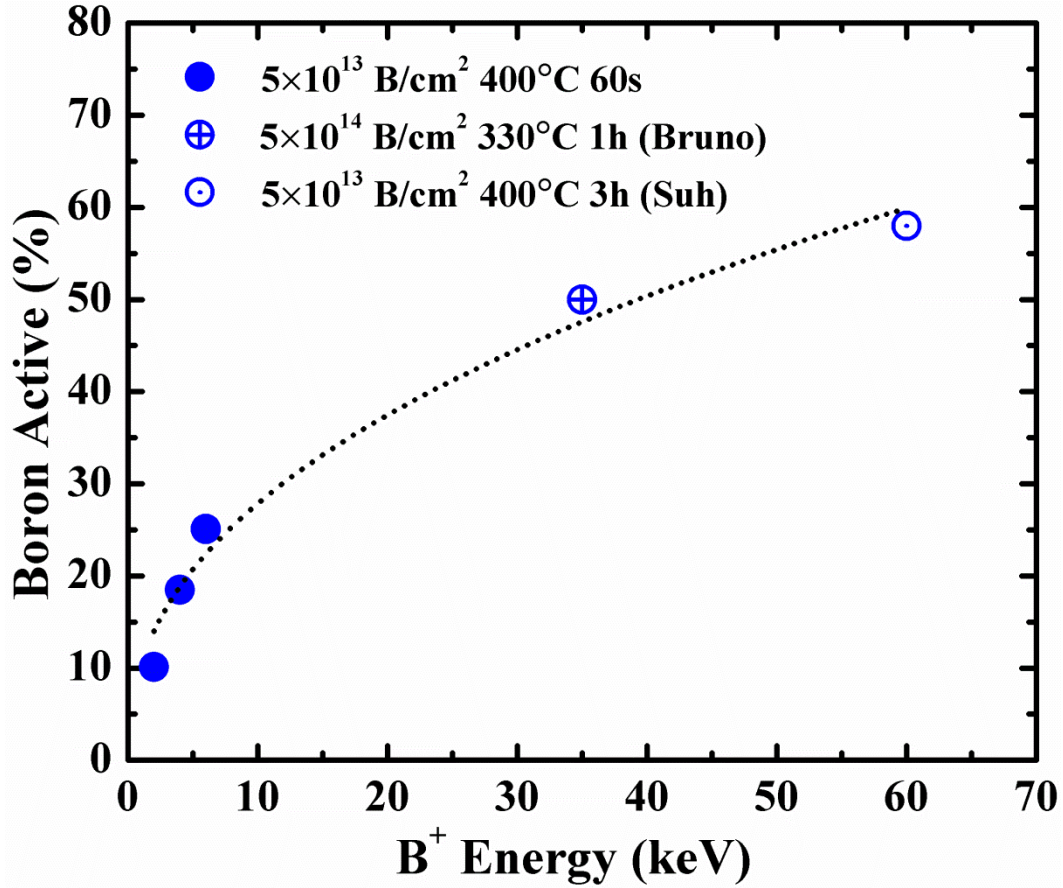


Figure 4-5. Measured percentage of electrically active B at variable implant energies. A 35 keV implant corresponds to an R_p of 90 nm. The crossed and dotted data points are from Bruno *et al.*²³ and Suh *et al.*³⁶, respectively.

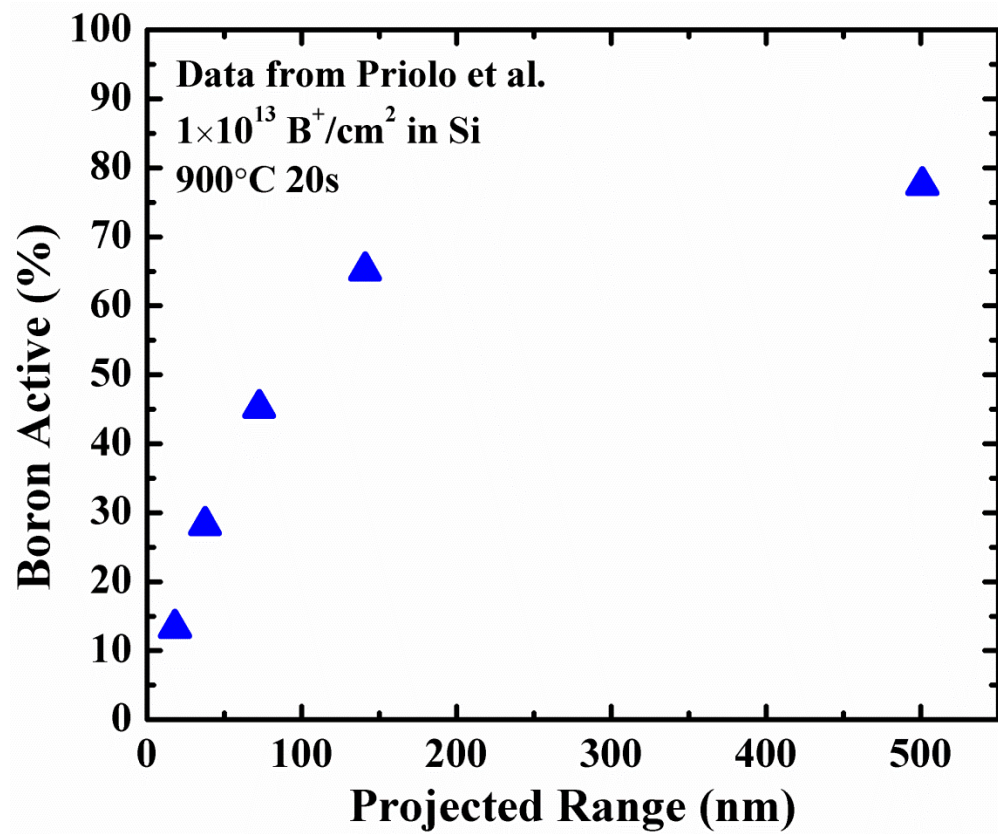


Figure 4-6. Measured percentage of electrically active B in Si at variable implant energies. Data is adapted from Priolo *et al.*¹³⁷.

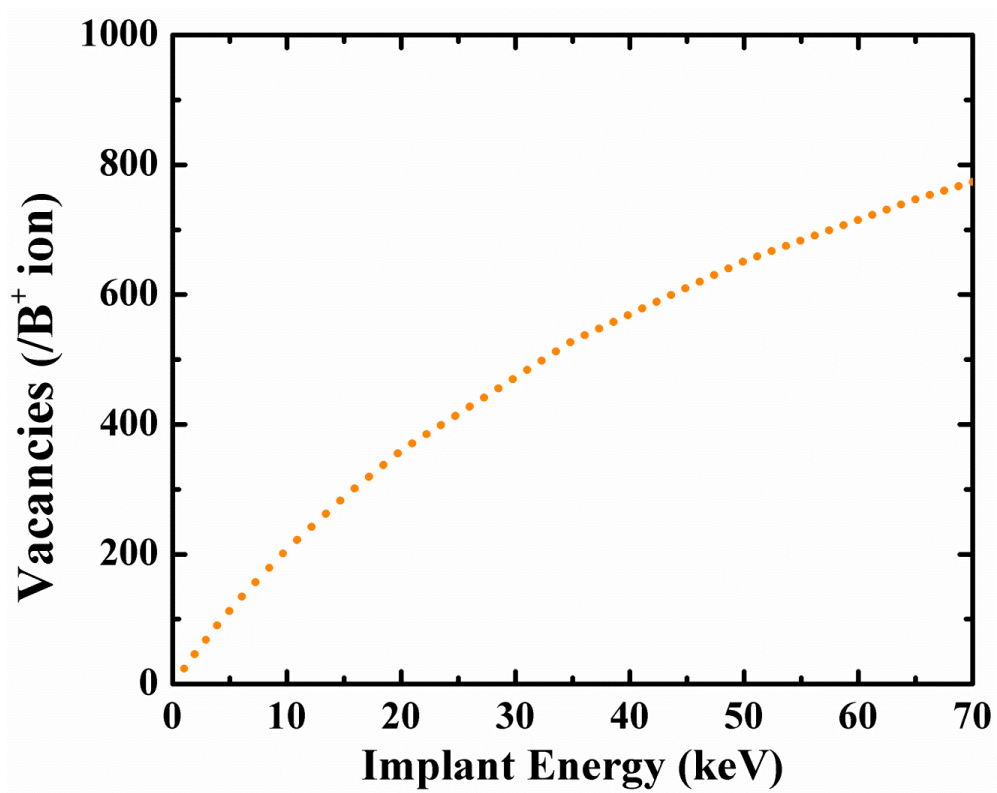


Figure 4-7. Vacancies created per incoming B ion as a function of implant energy as simulated by SRIM.⁷⁸

CHAPTER 5 THERMAL STABILITY OF BORON ACTIVATION IN GERMANIUM

5.1 Activation Stability of B in Ge

In recent years, several studies have investigated the electrical behavior of ion implanted B in both crystalline (c-Ge) and preamorphized (PA-Ge) Ge.^{23,31,35–37,145,146} Similar to Si, it has been shown that preamorphization increases dopant activation during the solid phase epitaxial growth (SPEG) process.³⁵ However, the majority of the experiments published in the literature have used high energy B⁺ implants that are not directly relevant for ultra-shallow junctions.

Limited data exists regarding the thermal stability of B activation in Ge which can be explained by the adequate stability evidenced in the available reports. Impellizzeri *et al.* has shown that 35 keV B⁺ implants exhibit stable activation following a modest activation anneal. They have shown that a modest 360°C anneal results in a high level of boron activation³¹ which remains stable for anneals up to 550°C for 1h.³⁷

Bruno *et al.* has shown similar results for c-Ge and PA-Ge samples in which activation remains stable for anneals up to 550°C for 1h. However, although not explicitly mentioned in this work, a qualitative decrease in R_S is evident for c-Ge samples while a similar increase is evident for PA-Ge samples.²³

Similarly, Simoen *et al.* has shown 4.5 keV B⁺ implantation to a fluence of $1.0 \times 10^{15} \text{ cm}^{-2}$ and $1.0 \times 10^{16} \text{ cm}^{-2}$ into c-Ge returns stable R_S values following RTA anneals between 400 and 600°C.⁴⁰ Satta *et al.* reported similar results for 6 keV B⁺ implantation to a fluence of $3.0 \times 10^{15} \text{ cm}^{-2}$ in which R_S remains stable for RTA anneals up to 600°C.³⁸ Similar to the work by Bruno,²³ the results shown by Simoen⁴⁰ and

Satta³⁸ *et al.* displayed a decrease in R_S with increasing annealing temperature for c-Ge samples.

Previously, it has been shown that the activation of 2 keV B⁺ implants in Ge has an anomalous activation behavior which is characterized by an incomplete activation independent of implanted fluence for both c-Ge and PA-Ge. The behavior is believed to be due to a B-Ge cluster formation which renders a large fraction of the implanted fluence inactive.²⁴ Although far less pronounced, the presence of B-Ge clusters has been reported previously, but has only been observed for implants into c-Ge.^{34,37–39} For Si, the formation and evolution of boron-interstitial clusters is well-characterized and understood,^{56,59,70} but to date, a comprehensive study has not been completed for B⁺ implants in Ge.

In this work, a systematic study of the effect of isochronal annealing on the electrical activation of ultra-shallow B⁺ implants in Ge is presented. High temperature anneals are used to determine if the activation is stable as temperatures approach the melting temperature of Ge. Transmission electron microscopy and secondary ion mass spectroscopy (SIMS) is used to further explain the electrical behavior observed upon annealing.

5.2 Experimental Details

Experiments were performed on Czochralski-grown n-type Ge (001) wafers with resistivity larger than 50 Ω -cm. Samples were B⁺ implanted at 2, 4, and 6 keV with fluences ranging from 5.0×10^{13} to 5.0×10^{15} cm⁻². An identical set of PA-Ge samples was produced by first implanting a Ge⁺ fluence of 2.0×10^{14} cm⁻² at 120 keV prior to B⁺ implantation to produce an amorphized surface layer to a depth of 100 nm as verified by

high-resolution cross-sectional transmission electron microscopy (HR-XTEM). The beam current was fixed at 1.1 mA for all B⁺ implants and the platen was held at 25°C.

Samples were processed in a Heatpulse 4100 rapid thermal annealer (RTA) in an N₂ ambient at 400-600°C for 60s to activate the implanted B. Select samples were isothermally annealed at 400°C for times ranging from 30s to 5 h. Additional samples were underwent high temperature isochronal anneals.

Micro Hall effect measurements were used for their ability to accurately measure the electrical properties of ultra-shallow junctions.^{126,147,148} Micro Hall effect characterization was completed using a CAPRES microRSP M-150 M4PP fitted with Au-coated probes, a probe spacing of 20 µm, and a permanent magnet with a magnetic flux density of 0.475 T. Hall sheet number (n_H) and mobility values (μ_H) were adjusted to obtain the carrier sheet number (n_s) and drift mobility (μ_d) by using a scattering factor (r_H) of 1.21 as determined empirically.³¹ The carrier density and drift mobility are related to the Hall values by $n_s = n_H \times r_H$ and $\mu_d = \mu_H / r_H$, respectively.

5.3 Isothermal Annealing

For this experiment, a small sample subset was implanted at 2 keV to a fluence of $1.0 \times 10^{15} \text{ cm}^{-2}$ into c-Ge and PA-Ge. The electrical behavior of these samples was monitored as a function of annealing at 400°C for times ranging from 30s to 5h. For short annealing times ($\leq 960\text{s}$), samples were annealed using an RTA while longer anneals were completed in a tube furnace. Both annealing environments utilized flowing N₂. Samples were processed concurrently meaning that an RTA sample annealed for 960s received all ramp-up and ramp-down cycles accumulated during all shorter annealing durations. RBS characterization was completed with a 2 MeV He⁺

beam at normal incidence was used to monitor the number of displaced Ge atoms as a function of annealing time.

Figure 5-1 shows the sheets resistance values obtained for isothermal annealing sequence at 400°C for B⁺ implants at 2 keV to a fluence of $1.0 \times 10^{15} \text{ cm}^{-2}$. In Figure 5-1 (A), the data for c-Ge samples is displayed. It is evident that sheet resistance decreases for times less than 120s and increases thereafter. The changes in sheet resistance are slight as the minimum R_S measured was 430.8 and 473.9 Ω/sq , respectively for 120s and 5h anneals. Figure 5-1 (B) shows the sheet resistance values obtained for PA-Ge samples. It should be noted that 60s at 400°C is the minimum time necessary to complete the SPEG process which explains why data for the PA-Ge series does not begin prior to this annealing time. In stark contrast to what is observed for c-Ge, PA-Ge samples show minimal change as a function of annealing time.

To provide further evidence that the R_S values do in fact decrease for short annealing times, a line scan comprising 40 individual measurements as a function of distance were completed on the sample annealed for 30s as shown in Figure 5-2. It is evident that the deviation from the mean is slight as the standard deviation is 1.76 Ω/sq across the entire 4 mm scan. From this line scan data, it can be assumed that every data point is reproducible and the trends observed are accurate.

Figure 5-3 displays the sheet number values obtained following the isothermal annealing sequence. In Figure 5-3 (A), it is clear that c-Ge samples show a strong decrease in active carriers with increasing annealing time. Conversely, Figure 5-3 (B) shows little change in active carriers for PA-Ge. It should be stated that the observed deactivation for c-Ge samples is significant in that slightly over 20% of the active

dopants become electrically inactive with further annealing; however, the overall fraction of active dopants remains near 10% for all annealing times investigated. The deactivation observed is not believed to be due to any sort of chemical dose loss as the PA-Ge samples were processed identically and did not exhibit any significant dose loss.

Comparing the R_S and sheet number data, it becomes clear that the increase in R_S for c-Ge samples annealed longer than 120s is due to a deactivation of dopant atoms. The decrease in R_S observed for short annealing times is believed to be due to annealing of implant damage which allows for an increase in the drift mobility.

Figure 5-4 shows the drift mobility for c-Ge samples annealed for times ranging from 30 to 1920s. It is clear that a quick uptick in drift mobility is evident for short annealing times which corresponds with removal of implant damage. After this increase, the drift mobility values begin to stagnate. The removal of implant damage and subsequent increase in drift mobility coupled with the deactivation of B atoms explains the R_S trends observed in Figure 5-1 (A).

Similar to the fluence-independent activation documented in previous chapters, the deactivation observed for c-Ge samples with increasing annealing times is believed to be due to the large interstitial population that exists following ion implantation which may spur the formation of an inactive cluster. The displaced Ge population can be measured using RBS which may provide insight into the deactivation behavior of the c-Ge samples.

Figure 5-5 (A) shows the RBS spectra acquired for c-Ge samples B⁺ implanted at 2 keV to a fluence of $1.0 \times 10^{15} \text{ cm}^{-2}$ following furnace annealing for 1, 3, and 5h. A virgin Ge sample is shown as well for comparison. Figure 5-5 (B) highlights the surface

region of the investigated samples. The area under the surface peak displayed in Figure 5-5 (B) is directly proportional to the displaced Ge concentration.

From this characterization, it is evident that the number of displaced Ge atoms does not change appreciably with annealing despite the deactivation observed as the surface peaks are nearly overlaid. It is, however, evident that there is a population of Ge atoms that are displaced from their lattice sites as the peaks are larger than that of a virgin crystal.

The number of displaced Ge atoms were calculated and tabulated in Table 5-1 in conjunction with the inactive number of B atoms as determined from the micro Hall effect characterization. It is clear that the number of displaced Ge atoms remains relatively constant with annealing time across the investigated range. Following a 1h anneal, 4.93×10^{15} Ge/cm² atoms are displaced in comparison to 4.56×10^{15} Ge/cm² following a 5h anneal. To gain perspective on the deactivation behavior, the ratio of displaced Ge atoms to electrically inactive B atoms (displaced Ge:inactive B) was determined and found to be approximately 6.66. The Ge:B ratio is relatively constant across the annealing range which thereby fails to yield information regarding the deactivation observed for c-Ge samples.

It should be noted that the RBS technique is unable to determine the confirmation of displaced Ge; whether it is situated as a unique point defect, an interstitial cluster, or an inactive Ge:B complex among other possibilities. This shortcoming of RBS limits the characterization ability of inactive B in Ge. However, the data obtained shows that a substantial fraction of Ge is situated off-lattice despite a

400°C anneal for 5h. This information gives further credence to the notion that the interstitial Ge population may be a driving force in the inactivity of ultra-shallow B in Ge.

5.4 Activation Thermal Stability Between 400-600°C

Figure 5-6 shows the sheet resistance values obtained for 2 keV c-Ge (Figure 5-6(A)) and PA-Ge (Figure 5-6(B)) samples after annealing between 400°C and 600°C for 60s. It is evident that large changes in R_S exist for samples implanted at a reduced fluence while minimal changes exist for those samples implanted at an increased fluence. The trends hold true for both c-Ge and PA-Ge, but the R_S data trends in opposite directions for both c-Ge and PA-Ge. For c-Ge samples, with increasing annealing temperature, a reduction in R_S is observed while for PA-Ge samples, an increase in R_S is evident.

Figure 5-7 shows the change in sheet resistance between annealing at 400°C and 600°C for 60s for samples implanted at 2, 4, and 6 keV. Rather than presenting all measured data, the relative change in R_S was used to highlight the trend observed for all implant energies while maintaining a concise plot. Interestingly, with increasing annealing temperature, it was apparent that R_S decreased for all c-Ge implant conditions and increased for all PA-Ge implant conditions. As implant fluence was decreased, the relative changes in R_S became more prominent for both c-Ge and PA-Ge. For the lowest influence implanted at 2 keV in c-Ge, R_S decreased 33.70% while for the highest fluence R_S decreased only 4.86%. A trend of increasing R_S was observed between the lowest and highest implanted fluences for PA-Ge as well.

Bruno *et al.* reported the thermal stability of high energy B activation following 35 keV implants in Ge with similar annealing conditions (360 to 550°C for 1 h).²³ The data appears to follow a similar trend to what is observed for ultra-shallow implants in this

work in which R_S decreases for c-Ge and increases for PA-Ge. However, it appears to occur to a lesser extent which is not surprising as the data presented in this work suggests that the trend decreases with implant energy. For example, for a B fluence of $5.0 \times 10^{13} \text{ cm}^{-2}$ into c-Ge, the decrease in R_S is 34% and 26% for 2 keV and 6 keV, respectively.

The trends in R_S behavior are intriguing and can be explained by examining the components of the resistance term itself. Figure 5-8 shows the thermal evolution of active carriers and drift mobility for a B⁺ implant to a fluence of $5.0 \times 10^{15} \text{ cm}^{-2}$ into c-Ge and PA-Ge for anneals between 400 and 600°C. Notably, it should be mentioned that no significant change in activation was observed across the investigated temperature range for both c-Ge and PA-Ge samples. Previous reports have shown that the activation of B in Ge is remarkably stable.^{23,34,36,40} However, Panciera *et al.* have reported that the dopant-defect interactions involved with end of range dissolution has an effect on activation values.¹⁴⁶ The observed changes were slight (approximately 10% change in activation/ deactivation) and suggests that dopant-defect interactions in Ge behave much differently from that which has been extensively studied in Si in which large fluctuations in activation are observed upon annealing.¹⁴⁹

In Figure 5-8(A), n_s is observed to increase with increasing annealing temperature for PA-Ge samples; conversely, n_s values slightly decreased for c-Ge samples. Similar to the work by Panciera *et al.*,¹⁴⁶ the observed changes in activation are subtle and do not have significant effect on the overall activation value. The changes in activation for conditions investigated were on the order of 10%. A significant fraction of the residual implanted dose remained electrically inactive following a 600°C

anneal for 60s. These results suggest that the B-Ge cluster responsible for the B inactivity in both c-Ge and PA-Ge is stable at elevated temperatures.

Drift mobility exhibited a contrasting behavior in that values decreased for PA-Ge and increased for c-Ge samples with increasing temperature as shown in Figure 5-8(B). The drift mobility decreased with increasing implant energy and annealing temperature for PA-Ge samples which can be explained by the increase in the number of active dopants. It is known that the impact of ionized dopants on mobility is much more significant than that of neutral dopants due to the effects of coulombic scattering.² The increase in μ_D for c-Ge is explained by the reduction of microstructural damage and subsequent reduction in scattering centers as evidenced in Figure 5-9.

It should be mentioned that the increase in μ_D for c-Ge is not as significant as expected based on reported mobility models for high B concentrations in Ge.³¹ This results suggests that some other mobility degradation mechanism is at work for c-Ge samples. The culprit is likely the presence of B-Ge clusters which scatter carriers and reduce their effective drift mobility. These mobility trends give further evidence that the inactive B is not in the lattice as a free interstitial, but rather likely in a B-Ge complex.

Figure 5-9 shows the microstructure of samples B⁺ implanted at 2 keV to a fluence of $5.0 \times 10^{15} \text{ cm}^{-2}$ into c-Ge and PA-Ge after annealing for 400-600°C for 60s. It is well known that B⁺ implants into c-Ge are characterized by a defective microstructure that is centered near the projected range (R_p) of the implant.^{34,37,40,45} In the case of c-Ge, the layer is not characterized by discernible extended defects, but rather a highly defective microstructure distinguished by inhomogeneous contrast which diminished with increasing annealing temperature. The inability to observe unique defects may be

due to several factors. The samples may not have been subjected to a sufficient thermal budget to allow the formation of extended defects or if already formed, they may be very small and high in concentration which limits the ability to view individual defects.¹⁵⁰ Further work was completed regarding B⁺ implant related defects in c-Ge and will be discussed in later a chapter.

In the case of PA-Ge, the initial amorphous Ge (α -Ge) layer was approximately 100 nm (not shown) and is observed to be fully regrown following a 400°C anneal for 60s as shown in Figure 5-9(D). In addition, no implant related defects were found for any annealing condition of PA-Ge. However, the formation of extended defects resulting from the SPEG process is not expected for low Ge⁺ implant fluences and is not expected to form for anneals in excess of 400°C.^{34,38,45,151}

The observed activation behavior in both c-Ge and PA-Ge is certainly unique and a far departure from what has been observed previously for B⁺ implants in Si. The ultra-shallow nature of the implants in this work suggests that there may be a correlation with surface proximity, but the effect may not have been captured within the investigated B⁺ energy regime. The Hall effect results by Mirabella *et al.* for 35 keV B⁺ implantation which report full activation following a modest 360°C for 1h further suggests that the cluster behavior observed is a function of implant energy. It has been suggested that there is a barrier to point defect recombination at the Ge surface which has been shown to spur the formation of a nanoporous structure.¹⁴¹ However, the clustering behavior was prominent also for samples implanted at 6 keV and any correlation between surface proximity and clustering that exists was not apparent in this work.

5.5 High Temperature Anneals

The large inactive fraction of B following annealing at 600°C for 60s for nearly 2/3 of the melting temperature of Ge in both c-Ge and PA-Ge samples is intriguing. The changes in electrical values can be deemed significant when comparing relative values between anneals, but on the whole, the fraction of dopant rendered electrically active is relatively minute. It would be assumed that any inactive defect complex that may exist would be able to be dissolved into its constituent components, in this case presumably B and Ge, given a heat treatment high enough in temperature. To determine if a high temperature heat treatment is capable of dissolving the dopant-defect cluster, high temperature isochronal anneals at 10s were completed on samples implanted at 6 keV $5.0 \times 10^{14} \text{ cm}^{-2}$ into c-Ge and PA-Ge. The samples were capped with 100 nm of SiO₂ prior to the heat treatment to resist the loss of the Ge surface and implanted dopants.^{41,152,153} HR-XTEM was completed using a JEOL 2010F to image the microstructure of specimens before and after annealing. SIMS was used to verify the chemical profile following annealing. TEM samples were prepared using a FEI DB235 focused ion beam.

Figure 5-10 displays the sheet resistance of c-Ge and PA-Ge samples implanted at 6 keV to a fluence of $5.0 \times 10^{15} \text{ cm}^{-2}$ and were subjected to anneals for temperatures ranging from 400 to 850°C. Anneals in excess of 600°C were 10s while those below 600°C were 60s. The data shows that R_S is relatively stable for temperatures below 750°C, but for temperatures in excess of 750°C, an increase is evident in both series.

Figure 5-11 shows the sheet number of c-Ge and PA-Ge samples implanted at 6 keV to a fluence of $5.0 \times 10^{15} \text{ cm}^{-2}$ and were subjected to anneals for temperatures ranging from 400 to 850°C. Similar to the R_S data, the sheet number is relatively stable

at low temperatures while significant changes occur at increased temperature. For PA-Ge samples, anneals in excess of 650°C produced a dramatic decrease in sheet number while for c-Ge the decrease is less prevalent and occurs for temperatures in excess of 750°C.

5.5.1 B Concentration Profile Following High T Annealing

To eliminate the possibility of surface or dopant loss, secondary ion mass spectroscopy (SIMS) was used to verify that the B profile has not changed significantly during heat treatment to allow for direct comparison of electrical data across all anneals. Figure 5-12 displays the B concentration profiles as obtained from SIMS for samples as-implanted, annealed at 650°C for 10s and 800°C for 10s following removal of the SiO₂ and electrical characterization. The annealed profiles are characterized by an anomalous hump extending from the surface to near the projected range of the implant. The behavior is more pronounced for increasing annealing temperature. The channeling tail of the B profile is similar for all investigated samples. Similar behavior was obtained for PA-Ge samples as shown in Figure 5-13.

The anomalous SIMS data is explained by the presence of disperse pits distributed across the surface of the samples which interferes with the sputtering process during characterization. SIMS characterization relies on a standard rate of material removal as a function of time in order to effectively produce the atomic concentrations present in the material of interest. The presence of an interface or surface inhomogeneities make it difficult for sputtering to occur uniformly as a function of area which translates to non-conformities as a function of depth.¹¹⁸ The pits are explained through the loss of the Ge surface through the formation of GeO and subsequent desorption of GeO.^{41,152,153} However, it has been observed that the

surface loss occurs only from material desorb from pits and is not a planar process. Figure 5-14 shows a HR-XTEM image of a pit formed during thermal processing of Ge prior to removal of the SiO₂. It is evident that the native oxide of Ge still remains which shows that the initial surface is not affected by surface loss in areas where pitting does not occur.

The planar area typically measured during SIMS characterization is relatively large and is typically on the order 0.1 cm².¹¹⁴ The relatively large characterization volume lends SIMS towards being more of a sampling technique representative of the bulk rather than local concentration differences.

An obvious benefit of using scaled down metrology tools is that the sensitivity is much greater than conventional tools and enables the characterization of precise locations.^{106,108,154} The electrical measurements on these high temperature samples were completed in regions that were devoid of pits and were optically pristine. To further confirm that this is true, measurements taken in locations that have even minor surface scratches yield inconsistent results. In addition, even activation fluctuations created by inhomogeneous laser annealing is easily detected by MHE characterization.¹⁰⁴

If the surface was lost due to GeO desorption, a lateral shift in the B concentration profile would be expected. Published results concerning surface loss from Ge desorption confirm this to be true as well.¹⁵² However, this is not the case for these samples. The profile tail of the as-implanted and annealed samples are well-aligned. If the surface was lost during GeO desorption, the concentration in the tail region of the profiles would not coincide with each other as is shown in Figure 5-15. In

this figure from Oh *et al.*, it is evident that surface desorption introduces a significant horizontal shift in the chemical profile following surface desorption of uncapped samples.¹⁵² This shift is not evident in the SIMS profiles displayed in Figure 5-12 and Figure 5-13. The SIMS characterization is unable to show that the peak of the B profile is unchanged, but the data obtained from the tail of the profile proves that B is still located in the substrate at approximately the same depth as expected. The lack of diffusion is in agreement with published values regarding B diffusion in Ge following ion implantation.²⁸⁻³⁰

5.5.2 Reduction of Active Carriers Following High T Annealing

The equilibrium solid solubility of B in Ge at 800°C is considered to be approximately $5.5 \times 10^{18} \text{ cm}^{-3}$ as measured from high temperature diffusion studies. In these studies, the diffused part of the B profile was considered to be below solubility while the non-diffused B was considered to be above solubility.²⁸⁻³⁰ In addition, phase diagram determinations have shown the solubility of B in Ge to be negligible.^{26,27}

The analysis of the n_S data shows that the increase in R_S is due to a reduction in the number of active carriers with increasing temperature. The reduction of carriers can be explained by the metastable electrical activation created during the ion implantation process. Upon high temperature annealing, the B atoms fall out of solid solution with Ge as it approaches its equilibrium state.

5.5.3 Significance of the Lack of B Diffusion

It is well-known that B diffuses through an interstitial-mediated mechanism and is largely controlled by the large formation energy of Ge interstitials.^{30,50} Under equilibrium conditions, B does not readily diffuse²⁸⁻³⁰, but diffusion of B in Ge has been observed when an excess interstitial concentration is present.^{48,50,54} The electrical and NRA

characterization completed in prior chapters as well as this chapter confirms that a large fraction of implanted B is located in off-lattice positions following annealing. RBS characterization has also shown that a large population of displaced Ge also remains following annealing. However, it is not known whether B atoms can be situated as interstitial B or in a B-Ge cluster.

The lack of diffusion is certainly a note-worthy observation that may shed light on the confirmation of off-lattice B atoms. Given the high residual interstitial Ge concentration, it could be expected that B diffusion would be observed following an anneal at 800°C for 10s as these interstitials should be mobile given this thermal budget. Transient enhanced diffusion of B in Ge has been documented following a 380°C anneal for 1h in which end of range damage was shown to dissolve thereby releasing interstitials to induce B diffusion.⁴⁸ However, for this work, no diffusion was observed. For boron in Si, it has been observed that the fraction of the B atoms in an inactive complex with Si do not diffuse.¹⁵⁵ Similar behavior could be expected for B in Ge. It can be interpreted that the off-lattice B and Ge concentrations as measured by Hall and ion beam analysis techniques are not free interstitials, but rather arranged in a thermally stable B-Ge complex. Bisognin *et al.* and Impellizzeri *et al.* have reported the formation of a B-Ge cluster in the ratio of 8:1 (Ge:B) following a 35 keV B⁺ implant and annealing at 360°C for 1h.^{37,39} From this information, it can be assumed that the off-lattice B and Ge populations are in an electrically inactive and thermally stable complex which explains the lack of diffusion of the chemical profile observed following high temperature annealing.

5.6 Theory for B Inactivity

The observed activation behavior is unique in that it is independent of implanted dose. The Hall and channeling analyses data in the previous chapter suggests that a small fraction of the implanted B is located substitutionally while the majority of the dopant is located in off-lattice positions. Presumably, the dopant is bound to an electrically inactive complex; notably the formation of a B-Ge cluster as has been documented for 35 keV B⁺ implants in Ge.^{23,37,39} In addition, the minimal change observed with increasing annealing temperature suggests that the inactive complex is thermally stable during subsequent anneals. For PA-Ge samples, a modest 60s anneal at 400°C is necessary to complete SPEG and activate the B. However, annealing at increased temperature has not shown any significant change in activation for PA-Ge or c-Ge.

It is not clear whether an inactive B-Ge cluster forms during the implantation or during the subsequent annealing step. The formation of the well-studied B-Si complexes occur during the post-implantation annealing step.^{156–158} For this work, the platen is held at room temperature during implantation to reduce sample heating, but the temperature of the sample, specifically the sample surface, is not directly held at a set temperature. Recent works by Lopez *et al.* have shown that B⁺ implantation in Ge can induce thermal spikes, or a localized volume near the ion cascade of increased temperature, due to the reduced melting temperature and increased thermal conductivity of Ge with respect to Si.¹⁵⁹ These thermal spikes may allow for the formation of the inactive complex during the implantation step. Although to a lesser extent, thermal spikes do occur in Si as well during implantation,^{159,160} but the formation of B-Si clusters are not observed until post-implantation annealing. If the inactive

complex is formed during post-implantation annealing as in Si, the B and point defect diffusivities are important parameters to hypothesize the formation mechanism of the inactive complex.

The diffusivity of atoms or point defects through a solid can be described by the Arrhenius relationship as follows:

$$D = D_0 \exp\left(\frac{-E_A}{kT}\right) \quad (5-1)$$

where D is the diffusivity, D_0 is the diffusion coefficient, E_A is the activation energy for the diffusion process, k is Boltzmann's constant and T is temperature.

The diffusivity of B in Ge has been reported to be characterized with a pre-exponential term of $19 \text{ m}^2/\text{s}^{-1}$ and an activation energy of $4.65 \pm 0.3 \text{ eV}$.³⁰ Similar values have been observed in other works.^{28,29} The mechanism for B diffusion is reported to be interstitial-mediated^{30,50,161} which is speculated to be limited by the formation of Ge interstitials which is reported to have a formation energy of 3.5 eV .^{162,163}

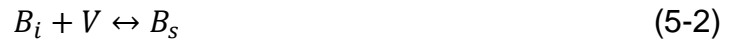
Data regarding the diffusivity and equilibrium concentration of self-interstitials in Ge is sparse and very little information is presently known. However, metal tracer diffusion experiments have shown that the vacancy diffusivity and concentration product is much greater than that of the interstitial.^{164,165} Other reports have documented similar values for the diffusion of Ge self-interstitials.^{166–168}

The calculation of the diffusion length of B atoms for the lowest thermal budget investigated of 400°C for 60s yields a value of $2.05 \times 10^{-7} \text{ nm}$. The diffusion length of B atoms is minimal and can be considered immobile for the lowest thermal budget investigated in this work.

However, the diffusivity of vacancies in Ge is quite significant given the investigated thermal budget. The diffusivity of vacancies in Ge in the temperature range from 650°C to 900°C has been reported to be characterized with a pre-exponential term of $2.40 \times 10^3 \text{ m}^2/\text{s}^{-1}$ and an activation energy of $2.65 \pm 0.11 \text{ eV}$. Using this Arrhenius relationship, the corresponding diffusion length of vacancies following 400°C for 60s is 28.67 nm. The calculated diffusion length of vacancies in Ge is several orders of magnitude larger than that of B or self-interstitials. From this information, it can be deduced that vacancies are the primary diffuser which would require vacancies to diffuse to interstitial B atoms to render them substitutional.

Using SRIM simulations, a 2 keV B⁺ implant to a fluence of $5.0 \times 10^{13} \text{ B}^+/\text{cm}^2$ in Ge creates a self-interstitial population, which to a rough approximation, is 50 times larger than the number of implanted B atoms.⁷⁸ It should be noted that the defect populations created by SRIM do not take into account any dynamic point defect recombination during the implant process. The number of interstitials and vacancies created during the ion implantation process creates an excess concentration that is in excess of equilibrium values which creates a driving force for point defect recombination.

Using the assumptions outlined above, for an implanted B atom to become substitutional on a lattice site, a vacancy must travel to the B site due to the inability for B to diffuse through the lattice satisfying the forward direction of this reaction:



where B_i is an interstitial B atom, V is the mobile vacancy and B_s is the substitutional B atom. Likewise, a vacancy must also travel to the self-interstitial to render it substitutional. The reaction can be described by:



where Ge_i is an interstitial Ge atom and Ge_s is the substitutional Ge atom.

It is theorized that the excess number of Ge_i created during implantation with respect to B_i drives the reaction depicted in Equation 5-3 forward while simultaneously restricting the number of vacancies available for recombination with B_i atoms.

Therefore, the reaction rate described by Equation 5-2 would decrease with an increased interstitial population. For a single mobile vacancy diffusing the lattice, the probability of interacting with an implanted B atom is only a fraction of the probability that it will react with a self-interstitial due to the far greater self-interstitial population. It is this low probability of B_i - V interaction that is theorized to restrict the activation of ultra-shallow ion implanted B in Ge.

It has been observed that increasing the B^+ implant energy results in an increase in the number of active or substitutional B atoms. Recent research has shown that the surface is an efficient sink for vacancies while reflecting interstitials.^{50,54} For near-surface implants, this boundary condition would further reduce the number of vacancies available thereby reducing the forward reaction of Equation 5-2. In addition, it should allow for a supersaturation of Ge_i following implantation which would increase the forward reaction depicted in Equation 5-3.

Also, as discussed in the previous chapter, reducing the B^+ implant energy effectively reduces the number of vacancies created which should have a direct correlation on the fraction of B atoms activated during annealing. However, the mere creation of vacancies should not be sufficient enough to describe the activation behavior as ion implantation is a very dynamic process. Indeed, increasing the implant energy

introduces additional point defects into the lattice, but it also broadens the implant-damage affected volume. Even though increasing the implant energy introduces a larger number of vacancies, it also increases the volume over which they are distributed thereby possibly reducing the probability of B_i -V interaction. The presence of a vacancy sink, such as the surface, or a vacancy clustering mechanism as discussed in the previous chapter further complicates assumptions regarding vacancy populations. The most significant vacancy population would be located in close proximity to the B ion to reduce these effects.

Lopez *et al.* has used molecular dynamics to simulate the point defect environment surrounding a B ion following implantation at 2 keV.¹⁶⁹ Figure 5-16 represents the vacancy population as a function of radial distance from the implanted B ion from this work. In Figure 5-16 (B), it is evident that the vacancy population sharply increases as a function of distance until approximately 6.0 nm is reached. The interstitial distribution closely mimicked the vacancy profile. The increase in vacancy population can be explained by the increase in the volume as the sampling radius is increased as $V = \frac{4}{3}\pi r^3$ where V is the volume and r is the sampling radius. Increasing the implant energy would certainly increase the cumulative number of vacancies created, but it would also spread the vacancies over a larger volume thereby which would decrease B_i -V interaction. The increase in activation observed with increasing B^+ energy can be ascribed to the introduction of a larger vacancy population; however, it should not be assumed that the mere number of vacancies created should be directly correlated to the active fraction of B atoms. The quantity of vacancies created does not

take into account the effect of the surface proximity or the vacancy distribution and their distance to the B atom which are both important factors to consider.

5.7 Simulation of Activation Behavior

To further test the preceding theory, the use of kinetic Monte Carlo (kMC) simulations were employed. The kMC simulations are capable of calculating the probability that certain atomic steps, for example a B atom migrating to a vacant site, will occur during processing given certain a time and temperature. For these simulations, the point defect equilibrium concentration and diffusivities listed in the previous section were used in addition to the B diffusivity. The vacancy and interstitial populations and distributions created during implantation were simulated using a Monte Carlo based process simulator and input into the kMC simulation as well. The dopant-defect reactions investigated in this work were $B_i + V \rightarrow B_s$, $B + I \rightarrow B_i$, $I + V \rightarrow \text{null}$, and $V + V \rightarrow V_2$. The formation of V_2 were also allowed to interact with free vacancies to form larger V clusters. The formation of these larger V clusters reduces the numbers of V 's available to react with B_i to render B atoms electrically active. The activation of a B^+ implant at an energy of 2 keV to a fluence of 5.0×10^{13} and $5.0 \times 10^{15} \text{ cm}^{-2}$ following annealing at 400°C for 60s and 1h was simulated in this work. These two fluences were chosen as they represent the highest and lowest values investigated in this work.

Figure 5-17 displays the kMC simulations for the samples implanted to a fluence 5.0×10^{13} and $5.0 \times 10^{15} \text{ cm}^{-2}$ following annealing at 400°C for 60s. In Figure 5-17 (A) and Figure 5-17 (B), it can be observed that the simulations predict an active concentration that is approximately 10% of the total B concentration profile. These results are in excellent agreement with the Hall results presented in this chapter as well as preceding chapters which have shown that the active fraction is approximately 10% for a 2 keV B^+

implant independent of the implanted fluence. By comparing the two investigated fluences, it can be observed that the simulations also predict that a single electrical solubility limit does not exist; rather, the active profile mimics the total B concentration profile. This behavior is in agreement with experimental work reported by Suh *et al.* in which the active profile mimics the chemical profile further suggesting that a single electrical solubility limit does not exist for B in Ge.³⁶

To simulate the thermal stability of the B activation experimentally observed in this work, simulations were completed as a function of annealing time. Figure 5-18 displays the kMC simulations for the samples implanted to a fluence of $5.0 \times 10^{13} \text{ cm}^{-2}$ following annealing at 400°C for 60s and 1h. In comparing the two simulations, it is evident that little change occurs with increasing the annealing time from 60s to 1h at 400°C. This prediction is in excellent agreement with the experimental data presented earlier in this chapter in which the active fraction is approximately 10% independent of implant fluence or thermal budget for B⁺ implants in c-Ge.

It should be mentioned that the observed activation behavior could only be simulated by allowing the $V + V \rightarrow V_2$ defect reaction and thus invoking a mechanism which consumes free vacancies. When the simulations were completed in the absence of these reactions, the predicted active fractions were much higher; near 60% rather than 10%. The simulations provide further evidence that the activation of B in Ge is driven by the availability of vacant sites to accommodate an interstitial B atom.

Correlation between electrical data and the present theory lies in the fact that the creation of point defects would scale proportionally with the implanted B⁺ fluence. Evidence of the dose-independent B inactivity can be observed in Figure 3-3 (B). The

number of vacancies created would also increase with increasing energy which may explain the increased activation. The observed electrical and surrounding theory is a far departure from what is typically observed for B activation in Si; however, the equilibrium point defect concentrations and diffusivities are also much different in that the vacancy is the dominant point defect in Ge rather than the interstitial as it is in Si.^{164,165} In effect, these differences give rise to the B activation differences present between Si and Ge.

5.8 Summary

The electrical activation of ultra-shallow B⁺ implants in c-Ge and PA-Ge was investigated using micro Hall effect techniques following isothermal anneals at 400°C and isochronal anneals between 400 and 850°C. Following isothermal annealing, it has been shown that a deactivation occurs for c-Ge samples while PA-Ge samples remain relatively constant. The origins of this deactivation is not clear, but could be assumed to be from the interstitial saturation remaining following implantation.

It has also been shown that systematic changes in R_S exist upon annealing for both c-Ge (decrease with temperature) and PA-Ge (increase with temperature) samples. Corresponding changes in sheet number and drift mobility have been observed to be the source of the systematic changes of R_S . However, the changes in sheet number were not significant for temperature below 650°C for PA-Ge and below 750°C for c-Ge. Above these temperatures, a significant decrease in activation was observed which was attributed to the dopant atoms falling out of solution with Ge as predicted by the equilibrium solubility.

A large fraction of implanted dopant was electrically inactive for all investigated conditions which suggests the presence of an electrically inactive and thermally stable B-Ge complex. The lack of diffusivity observed following an anneal at 800°C for 10s

further suggests that the off-lattice B atoms are bound to a B-Ge cluster. The slow diffusivity of B in Ge coupled with the overwhelmingly large population of Ge interstitials relative to the implanted B fluence following implantation is given as an explanation for the inability for B interstitial atoms to find a vacant site during annealing. Kinetic Monte Carlo simulations were employed to simulate the activation behavior

Table 5-1. Inactive B determined from micro Hall effect and the corresponding displaced Ge obtained from RBS characterization for c-Ge samples annealed for various times.

Annealing Time (h)	Inactive B (/cm ²)	Displaced Ge (/cm ²)	Ge:B Ratio
1.0	7.2×10^{14}	4.93×10^{15}	6.86
3.0	7.2×10^{14}	4.87×10^{15}	6.80
5.0	7.2×10^{14}	4.56×10^{15}	6.33

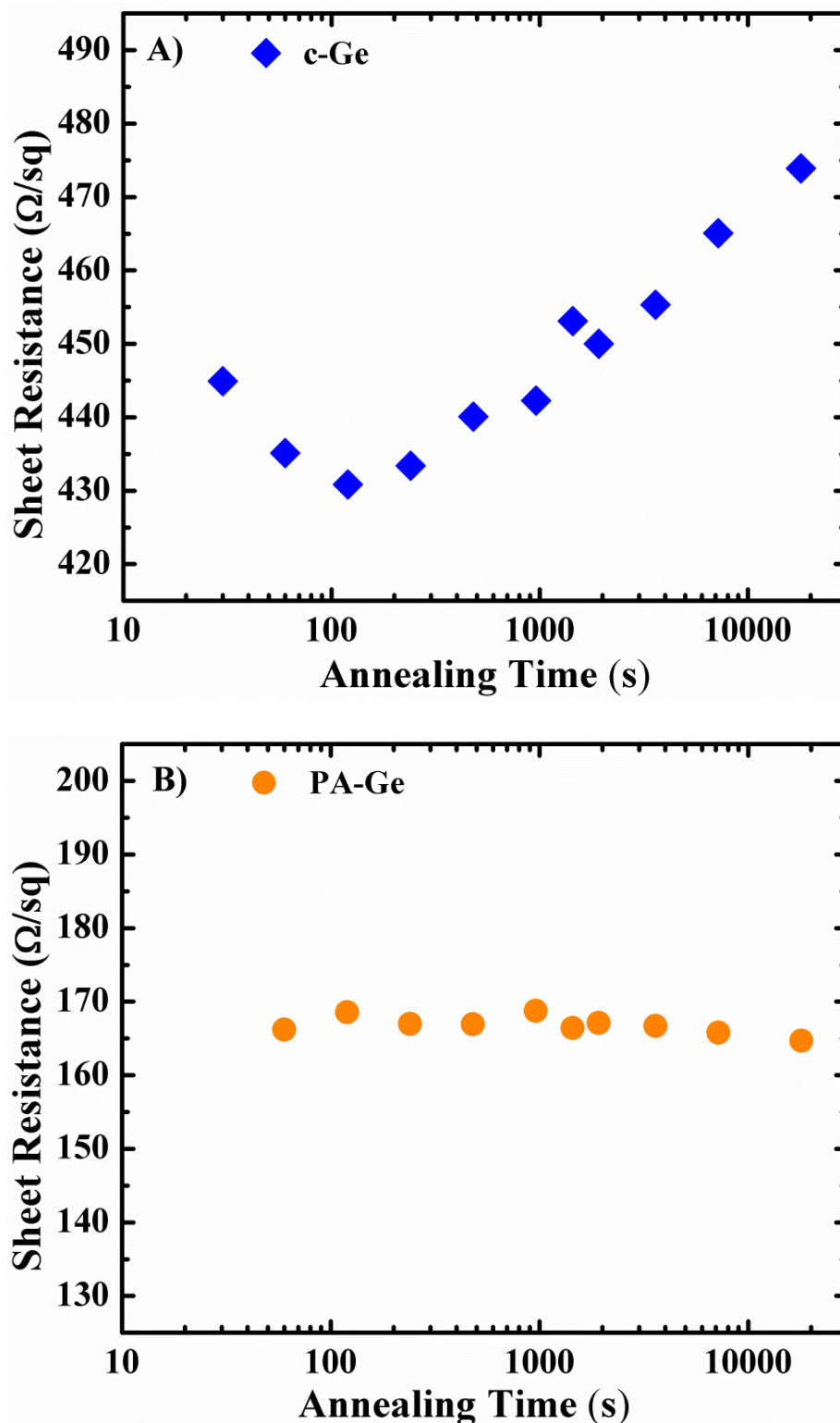


Figure 5-1. Sheet resistance data obtained for samples implanted at 2 keV with a fluence of $1.0 \times 10^{15} \text{ cm}^{-2}$ and subsequently annealed at 400°C for various times for A) crystalline Ge and B) preamorphized Ge.

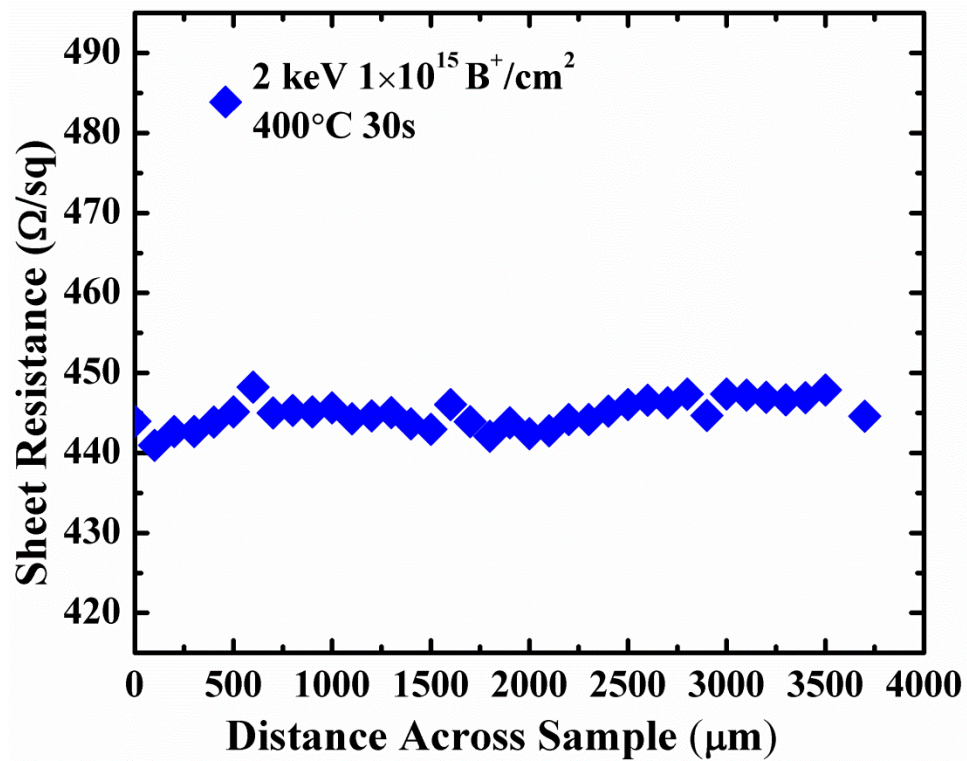


Figure 5-2. Sheet resistance line scan acquired across c-Ge sample annealed at 400°C for 30s. The precision of the M4PP technique is evidenced.

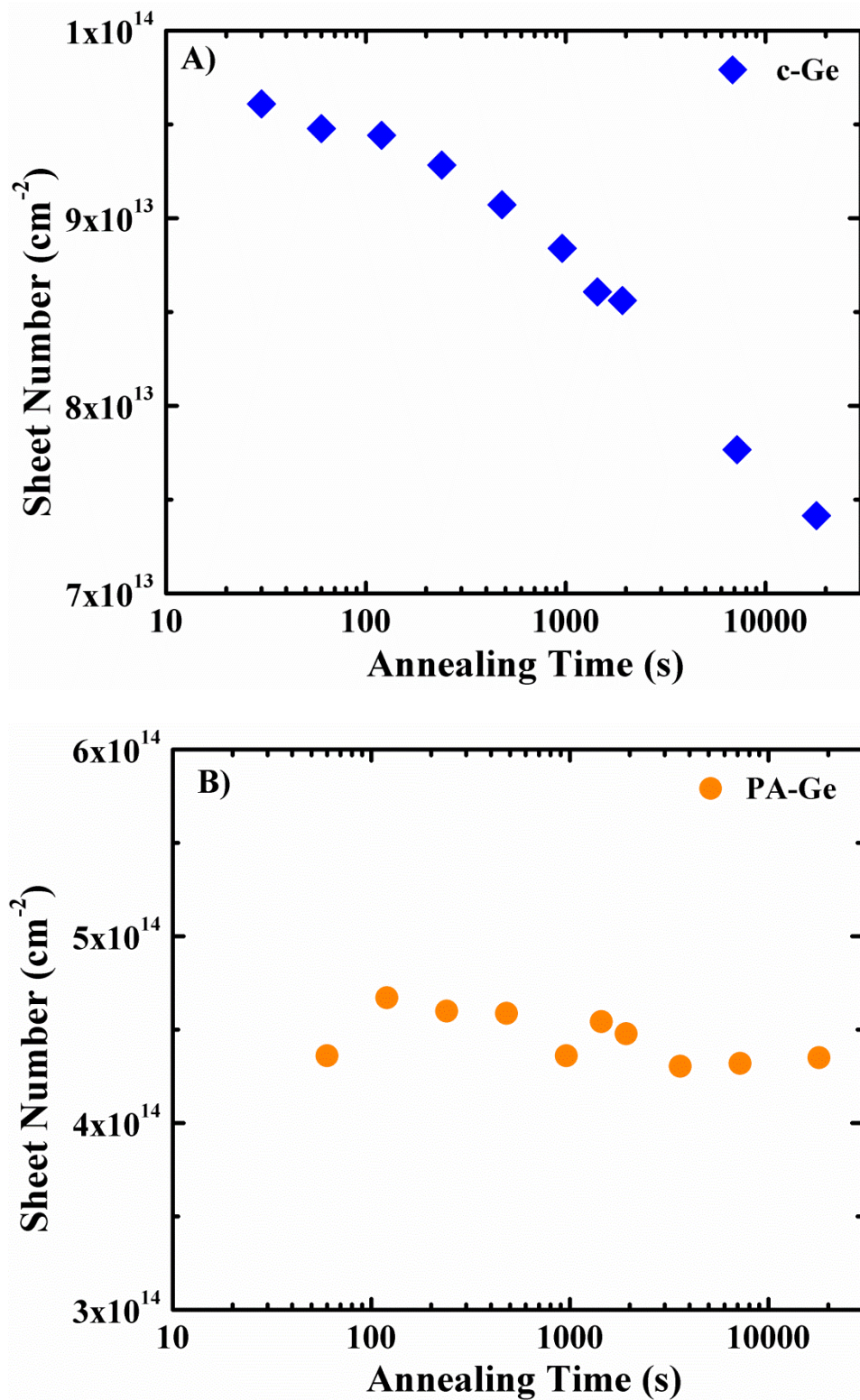


Figure 5-3. Sheet number data obtained for samples implanted at 2 keV with a fluence of $1.0 \times 10^{15} \text{ cm}^{-2}$ and subsequently annealed at 400°C for various times for A) crystalline Ge and B) preamorphized Ge.

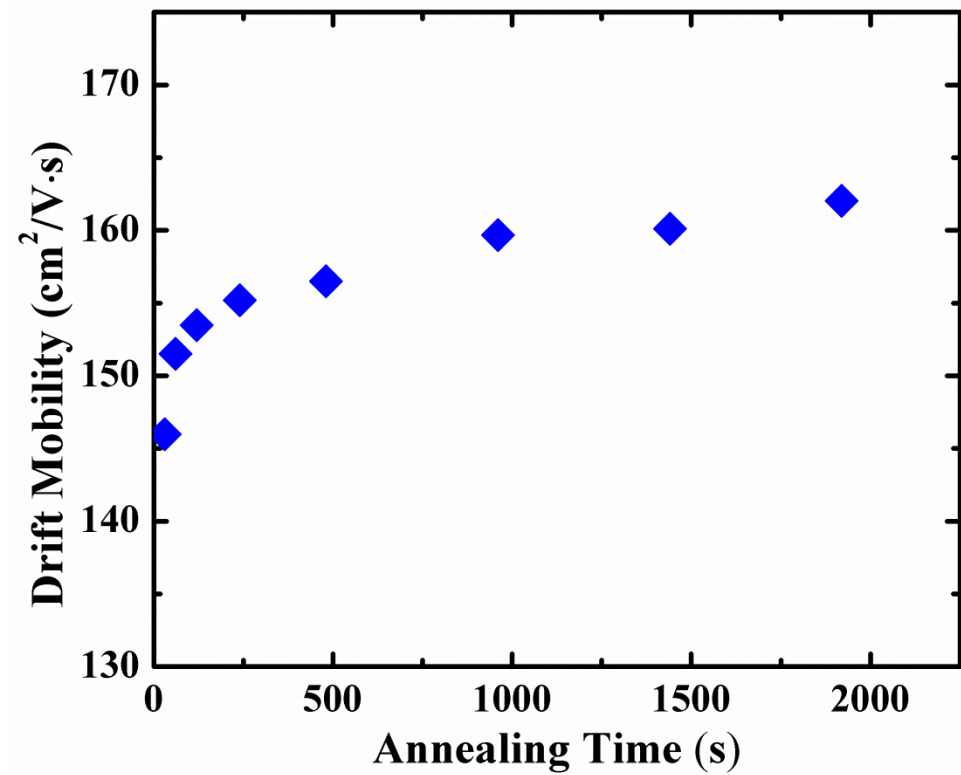


Figure 5-4. Drift mobility for a c-Ge samples implanted at 2 keV with a fluence of $1.0 \times 10^{15} \text{ cm}^{-2}$ and subsequently annealed at 400°C for various times.

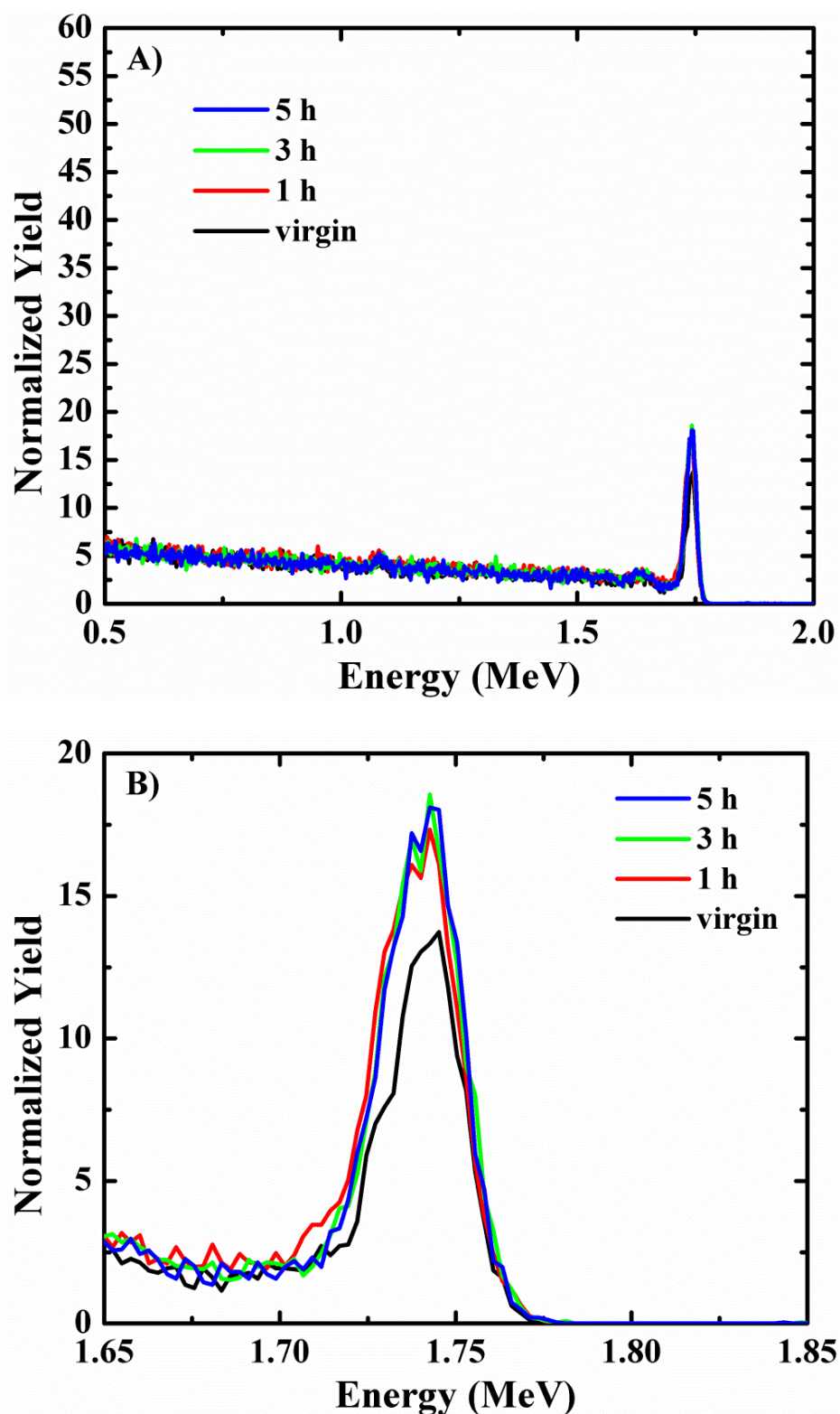


Figure 5-5. RBS channeling spectra for c-Ge samples implanted at 2 keV to a fluence of $1.0 \times 10^{15} \text{ cm}^{-2}$ and subsequently annealed at 400°C for various times where A) is the entire spectra and B) is the surface region.

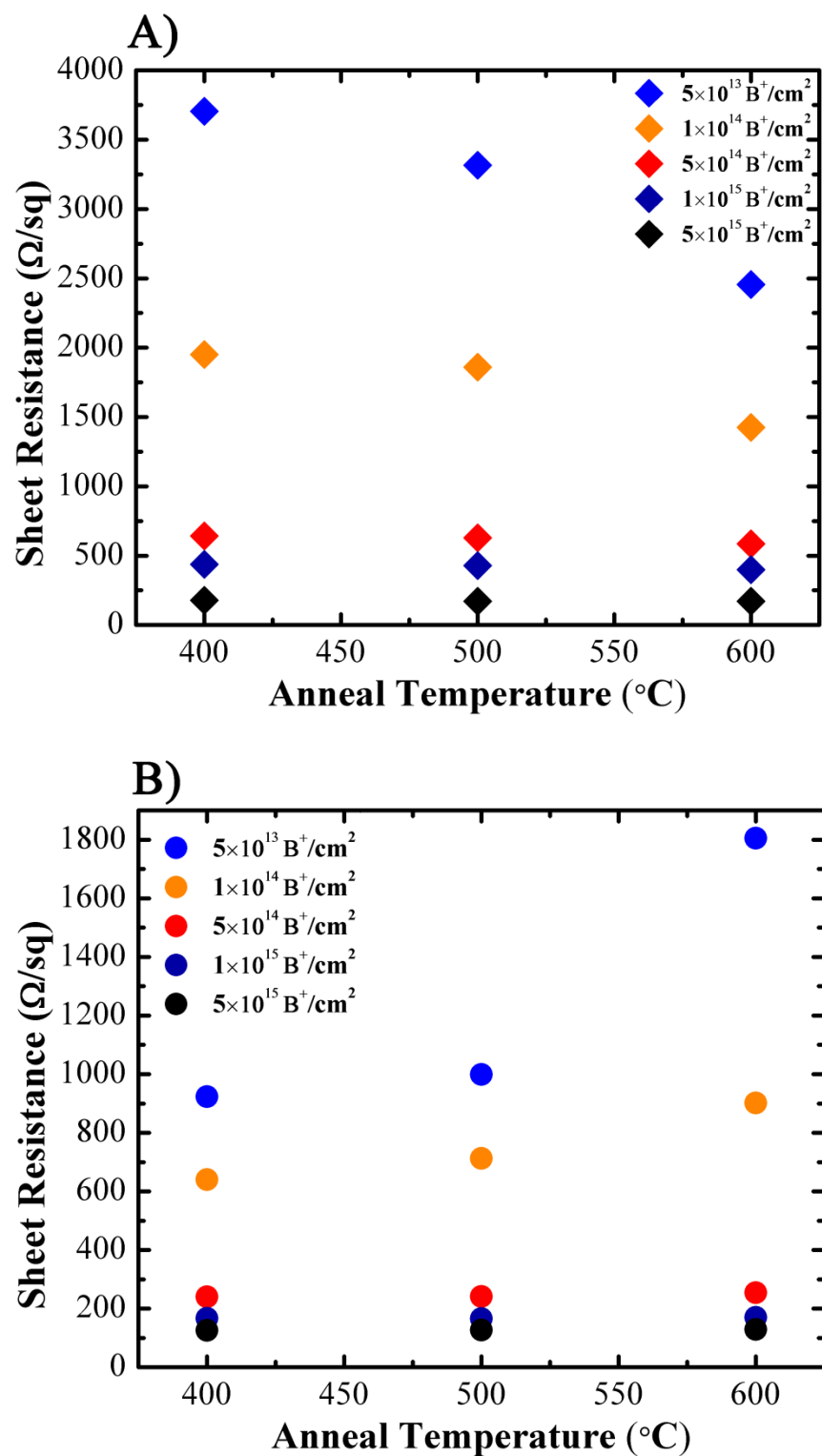


Figure 5-6. Sheet resistance data obtained for samples implanted at 2 keV with fluences ranging from 5.0×10^{13} to $5.0 \times 10^{15} \text{ cm}^{-2}$ and subsequent annealing at 400 °C and 600 °C for 60s for A) crystalline Ge and B) preamorphized Ge.

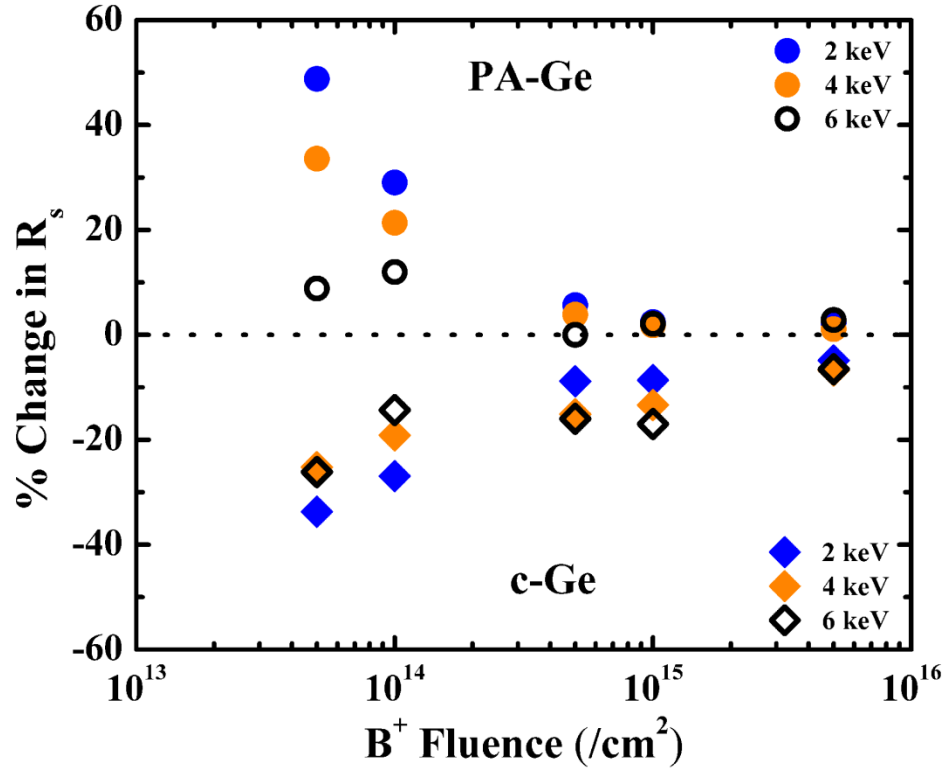


Figure 5-7. Change in sheet resistance for 2, 4, and 6 keV B⁺ implants to fluences ranging from 5.0×10^{13} to $5.0 \times 10^{15} \text{ cm}^{-2}$ between annealing at 400°C and 600°C for 60s. With increased annealing temperature, the data shows an increase and decrease in R_s for PA-Ge and c-Ge, respectively.

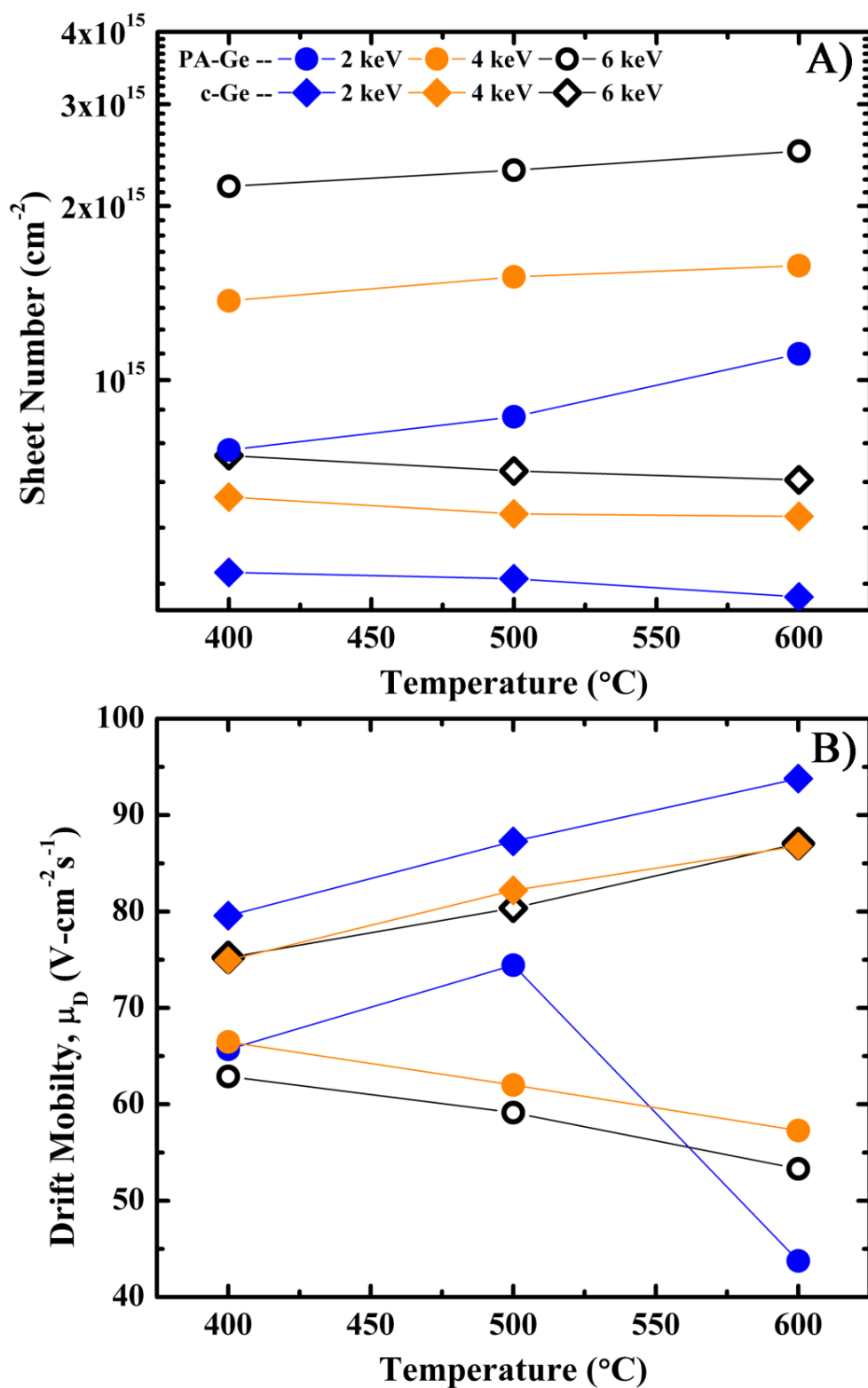


Figure 5-8. Electrical activation characteristics as a function of anneal temperature for samples B⁺ implanted at 2, 4, and 6 keV to a fluence of $5.0 \times 10^{15} \text{ cm}^{-2}$ into c-Ge and PA-Ge. Measured A) sheet number and B) drift mobility.

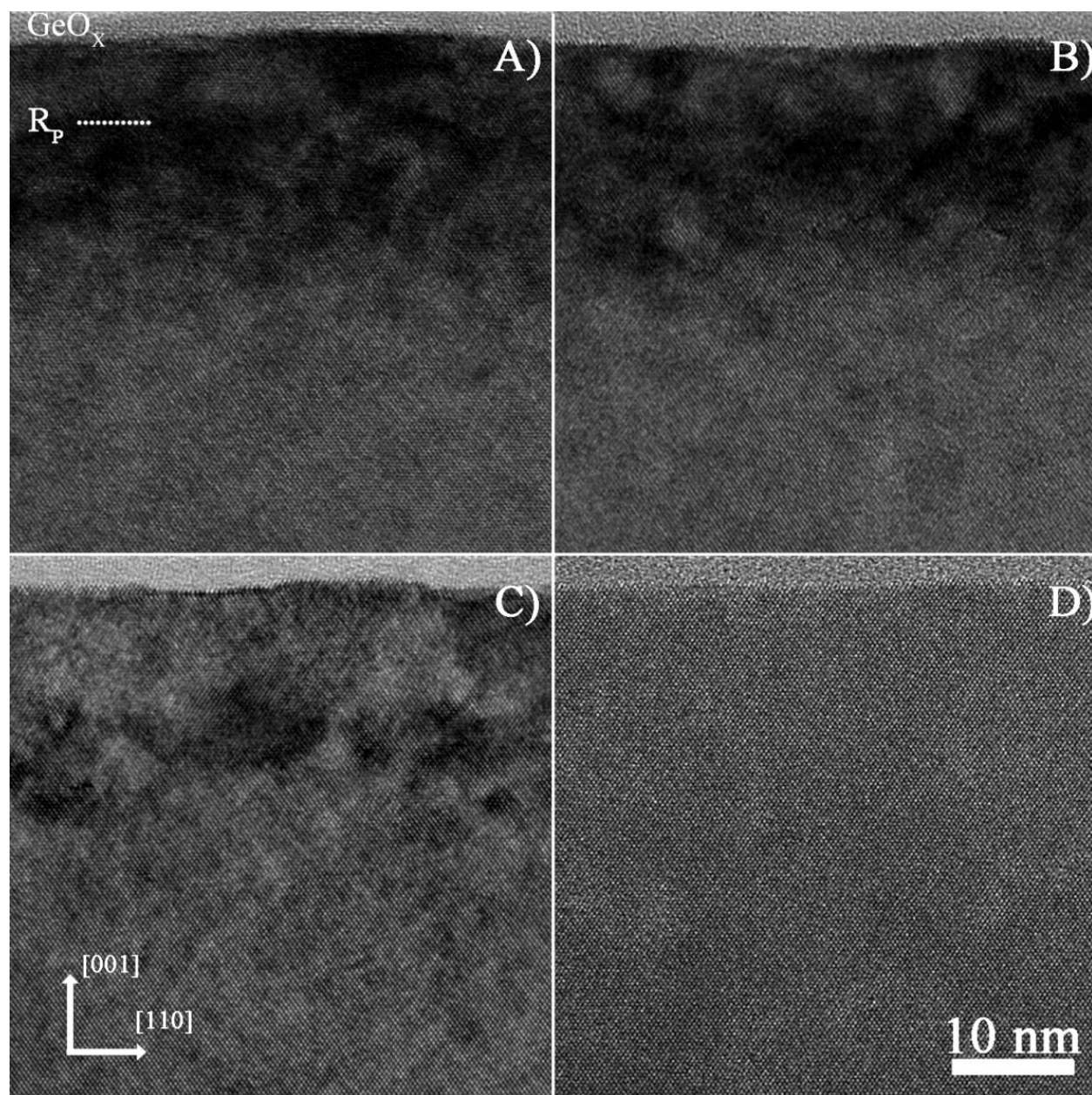


Figure 5-9. HR-XTEM images of samples B⁺ implanted at 2 keV to a fluence of $5.0 \times 10^{15} \text{ cm}^{-2}$ into c-Ge after annealing for 60s at 400°C A) at 500°C B) at 600°C C) and D) into PA-Ge after annealing for 60s at 400°C

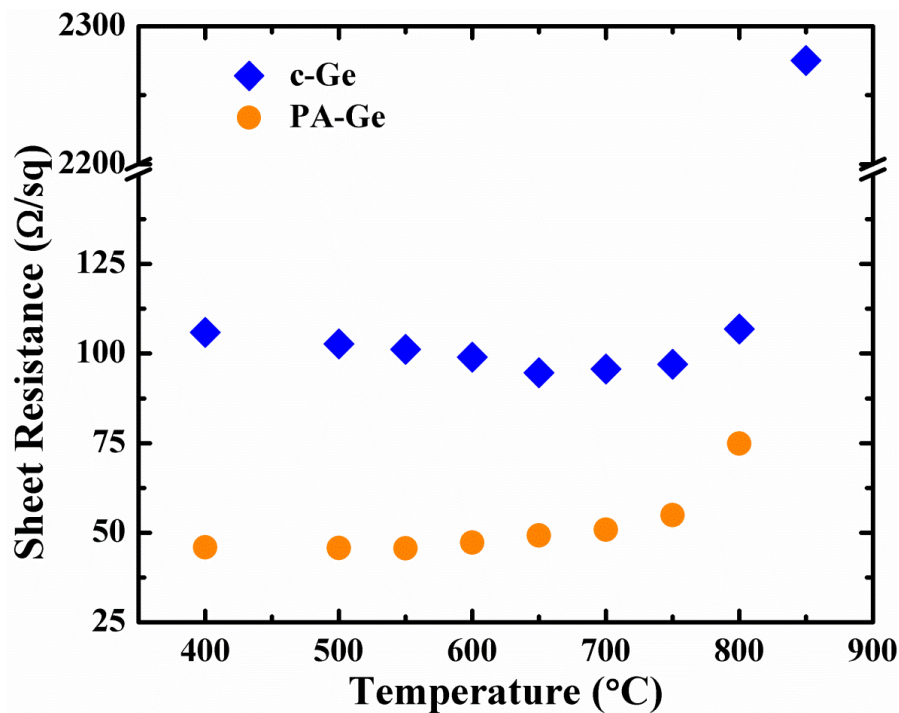


Figure 5-10. Sheet resistance for samples B^+ implanted at 6 keV to a fluence of $5.0 \times 10^{15} \text{ cm}^{-2}$ into c-Ge and PA-Ge. Anneals in excess of 600 $^{\circ}\text{C}$ were 10s while those below 600 $^{\circ}\text{C}$ were 60s.

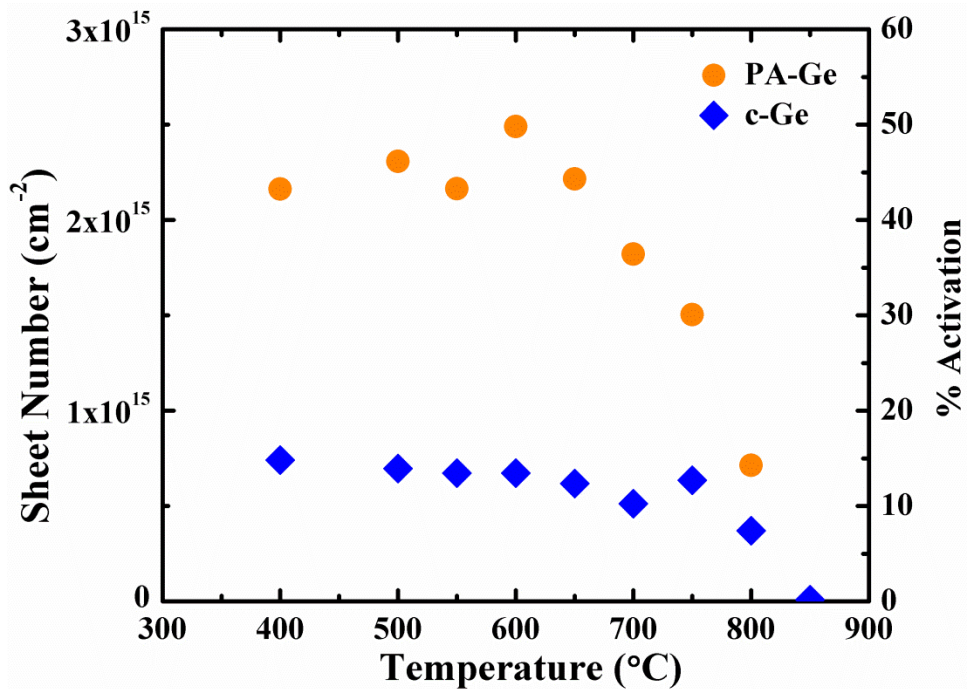


Figure 5-11. Sheet number for samples B^+ implanted at 6 keV to a fluence of $5.0 \times 10^{15} \text{ cm}^{-2}$ into c-Ge and PA-Ge. Anneals in excess of 600 $^{\circ}\text{C}$ were 10s while those below 600 $^{\circ}\text{C}$ were 60s.

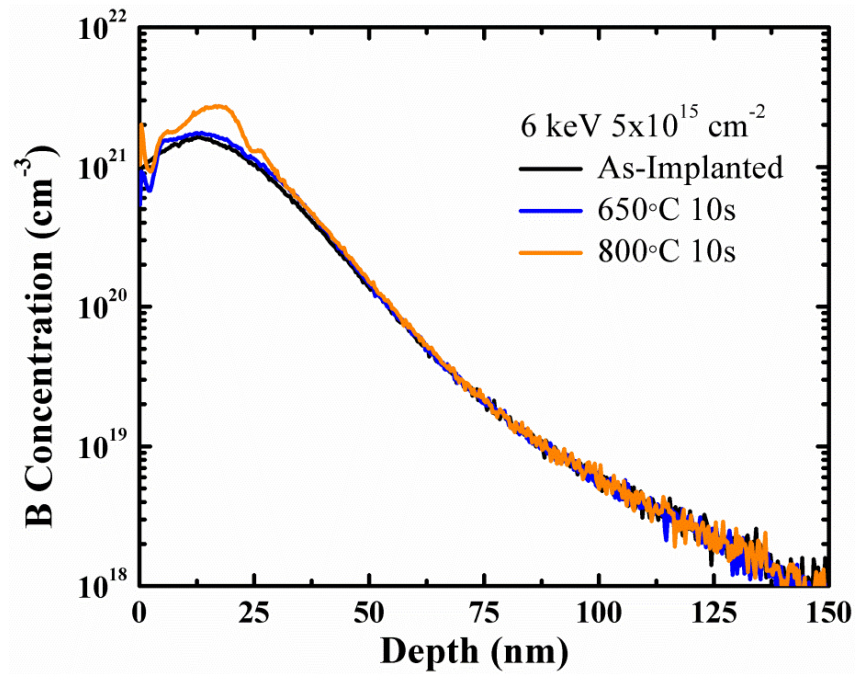


Figure 5-12. B concentration profiles for samples B⁺ implanted at 6 keV to a fluence of $5.0 \times 10^{15} \text{ cm}^{-2}$ into c-Ge as-implanted, annealed at 650°C for 10s, and annealed 800°C for 10s.

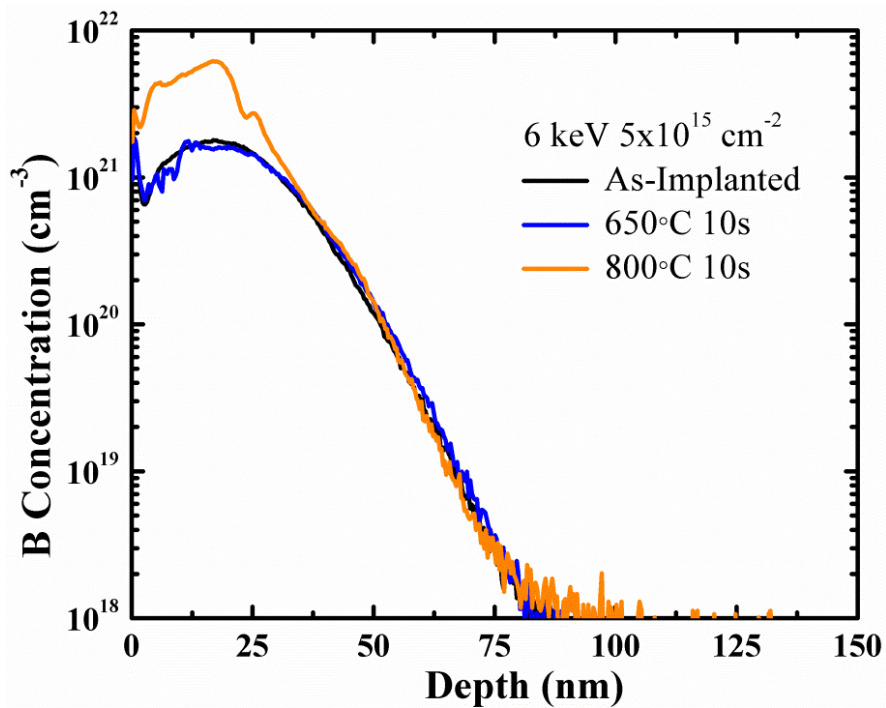


Figure 5-13. B concentration profiles for samples B⁺ implanted at 6 keV to a fluence of $5.0 \times 10^{15} \text{ cm}^{-2}$ into PA-Ge as-implanted, annealed at 650°C for 10s, and annealed 800°C for 10s.

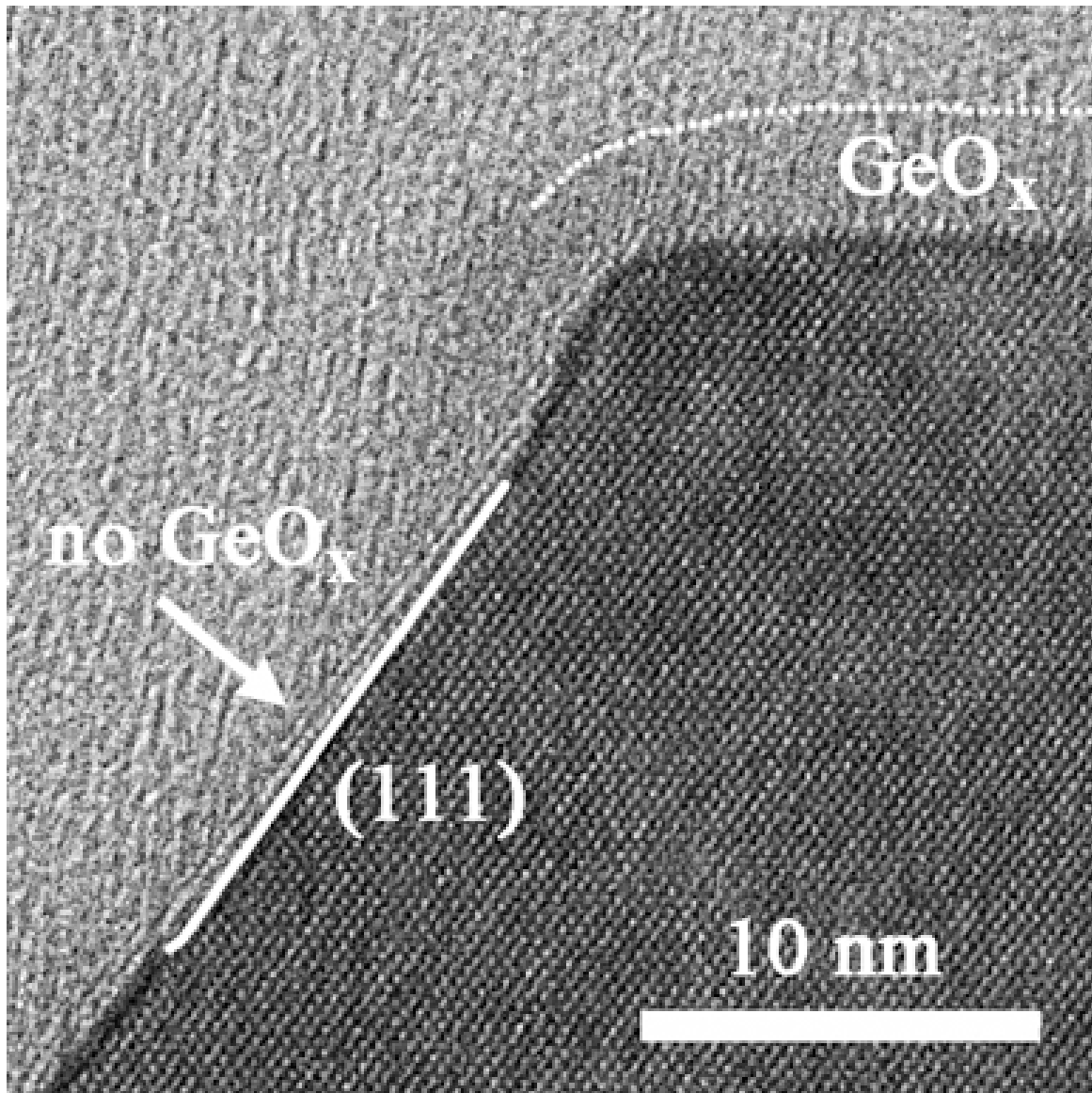


Figure 5-14. HR-XTEM micrograph of a pit formed in Ge following thermal processing. The presence of the native oxide surrounding the pit is evident.

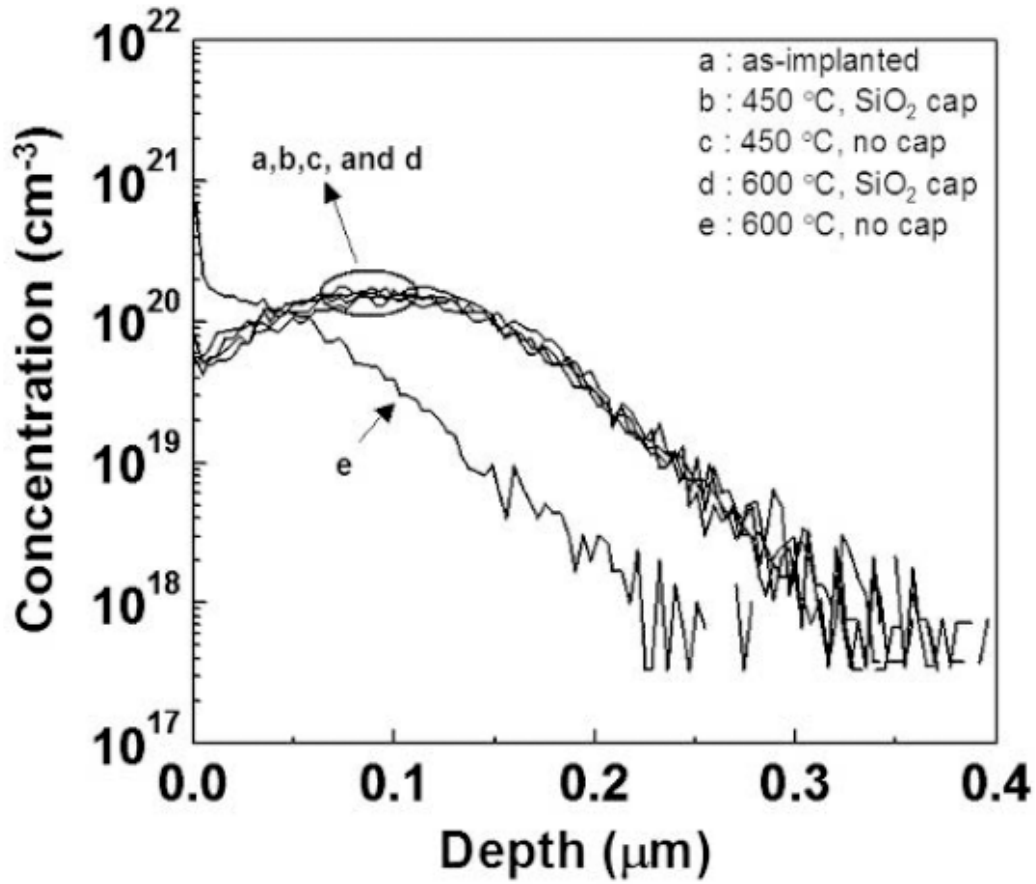


Figure 5-15. SIMS characterization of a sample B⁺ implanted at 35 keV to a fluence of $2.0 \times 10^{15} \text{ cm}^{-2}$ following various thermal treatments. The horizontal shift in the chemical profile of the uncapped sample annealed at 600 °C is evident. J. Oh and J.C. Campbell, *J. of Electron. Mater.* **33**, 364. Copyright (2004). Kindly reprinted with permission from Springer Science and Business Media.

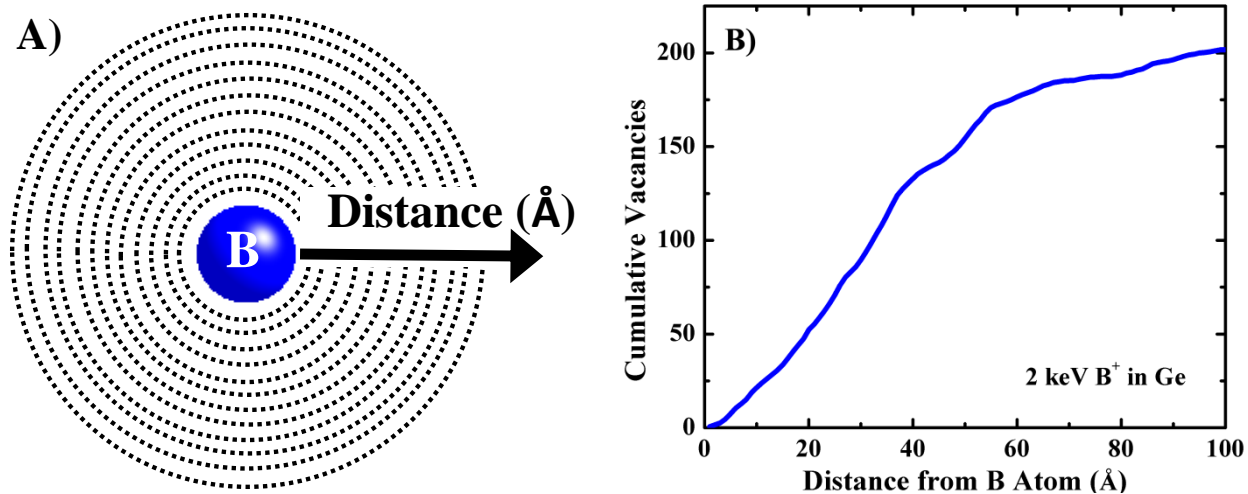


Figure 5-16. Simulation displaying the cumulative vacancy population as a function of radial distance from an implanted B ion at 2 keV.

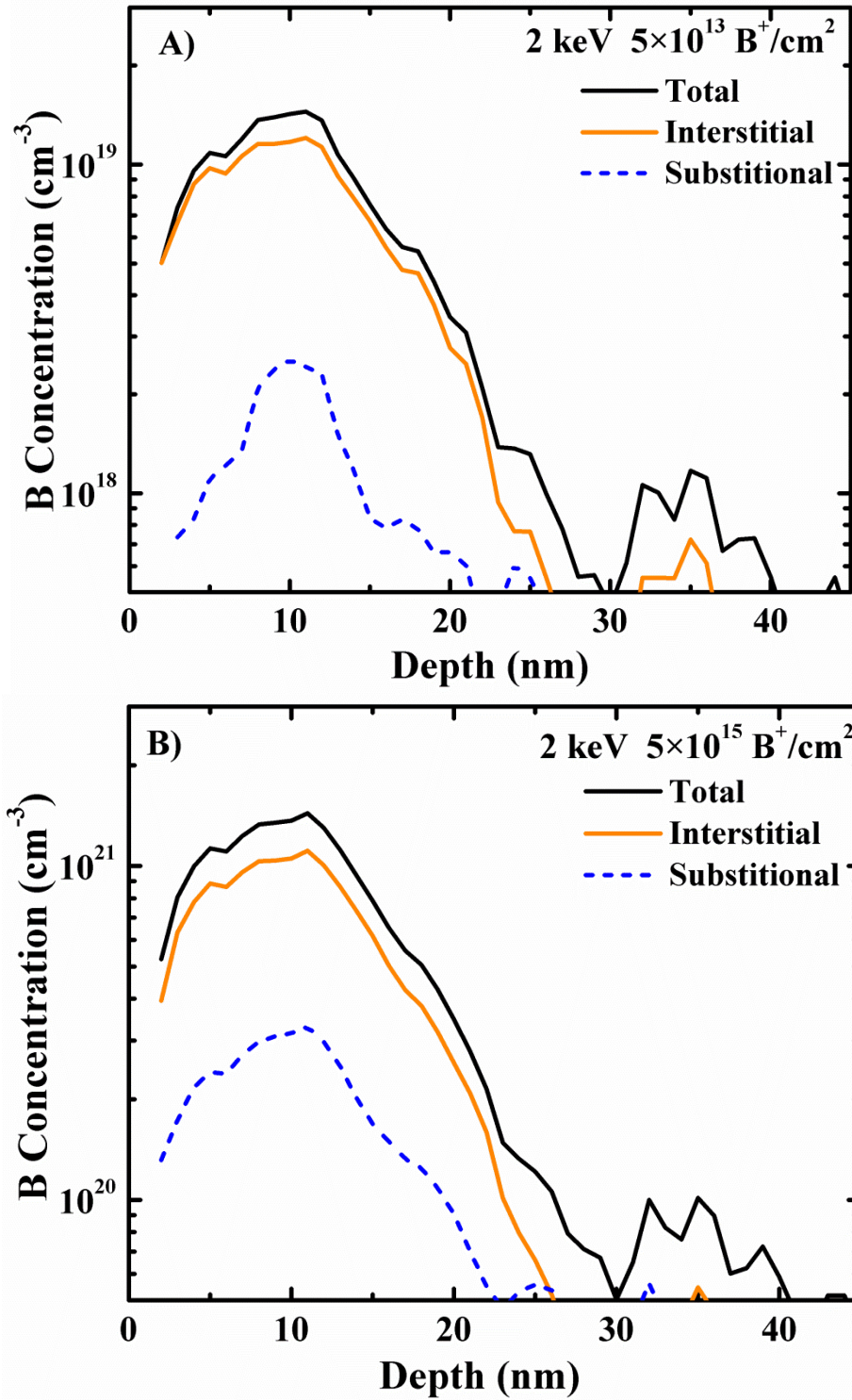


Figure 5-17. Kinetic Monte Carlo simulations displaying the substitutional and interstitial boron concentrations following annealing at 400°C for 60s for a 2 keV B⁺ implant to a fluence of A) $5.0 \times 10^{13} \text{ cm}^{-2}$ and B) $5.0 \times 10^{15} \text{ cm}^{-2}$.

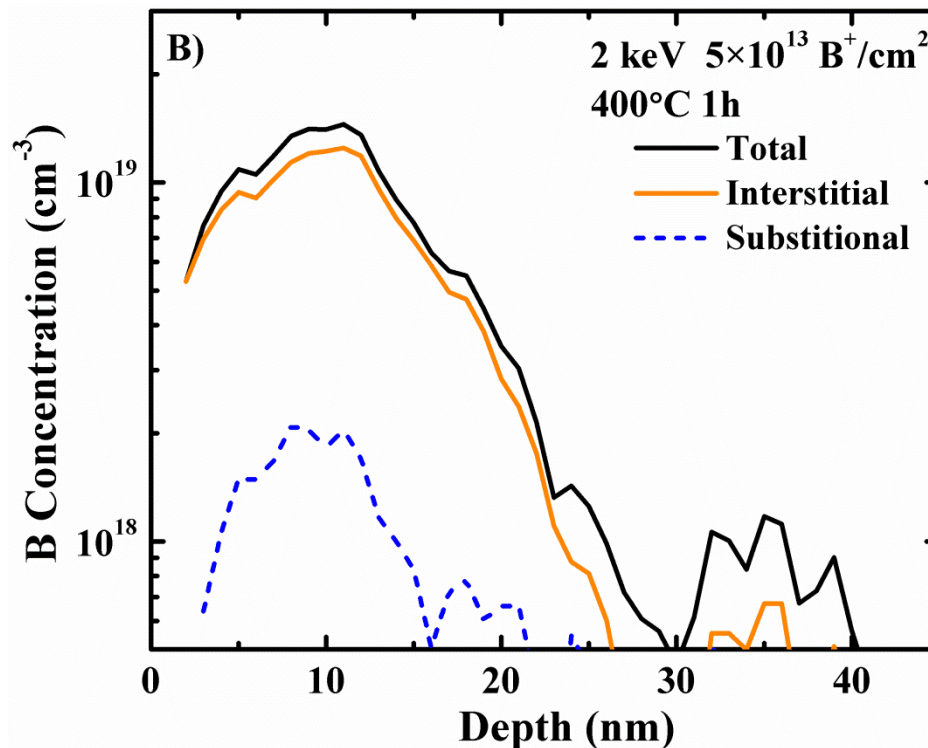
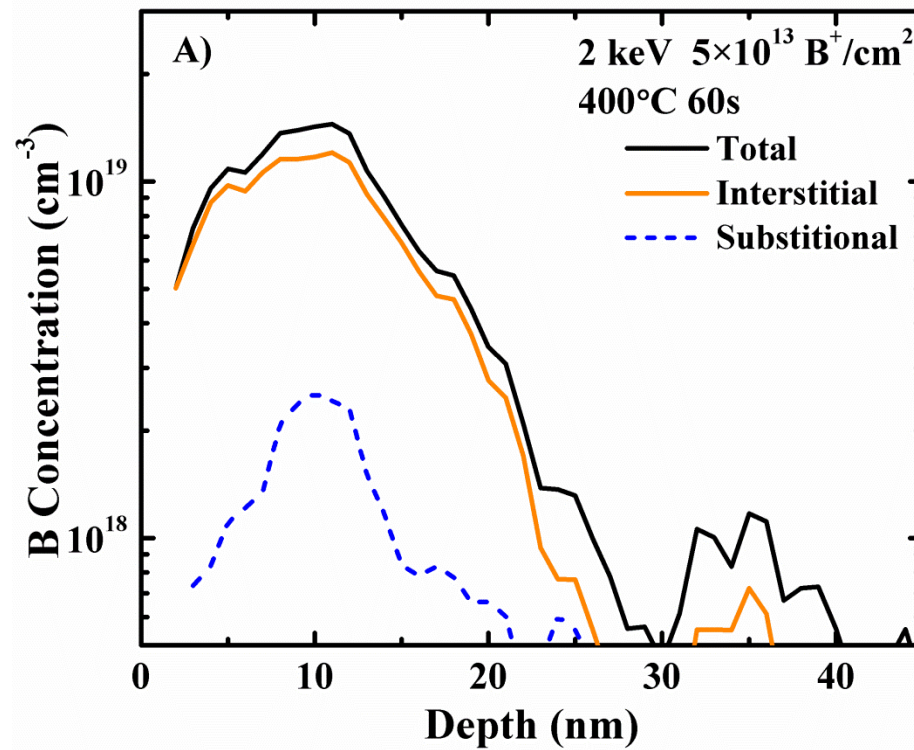


Figure 5-18. Kinetic Monte Carlo simulations displaying the substitutional and interstitial boron concentrations following B^+ implantation at 2 keV to a fluence of $5.0 \times 10^{13} \text{ cm}^{-2}$ and annealing at 400°C for A) 60s and B) 1h.

CHAPTER 6 IMPLANT-RELATED DAMAGE IN GE

6.1 Introduction

For the past half century, ion implantation has been used extensively in the semiconductor industry due to its ability to readily position high dopant concentrations accurately due to its self-aligning capabilities. Ion implantation has its drawbacks in that it creates lattice displacements which, given the correct conditions, can create extended defects during subsequent annealing. The formation and evolution of ion implantation related defects and their effects on semiconductors have been studied in depth for several decades. The understanding of these effects on dopant activation and diffusion are crucial for the scaling of semiconductor devices where with electrical activation needs to be high and junction depths are becoming increasingly shallow.

For Si, control of extended defects has proved invaluable for realizing dopant-defect interactions and their effects on dopant diffusion and activation. It is well known that the release of interstitials during defect dissolution allows for subsequent dopant kick out and diffusion in excess of equilibrium conditions.⁷⁻¹² This behavior allows for anomalous diffusion of dopants in Si and is known as transient enhanced diffusion (TED) which is characterized by a negative activation energy. The process can be inhibited through the implementation of a so-called vacancy engineering implant⁷⁴⁻⁷⁷ or with a co-implanted species to act as an interstitial trap to reduce the effects of excess interstitials.^{72,170} In addition, it is known that excess interstitials from extended defects can affect electrical activation as well.¹³⁻¹⁵

Recently, Ge has garnered research interests as a replacement material for Si in microelectronic applications.¹²⁷ Its advantageous electrical characteristics such as

increased hole mobility may allow for continued scaling of microelectronic devices.^{1,25}

The deviation from poly-Si/SiO₂ gate stacks has enabled the industry to avoid the issues of its unstable oxide.¹⁷¹ In addition, the relatively low melting point of Ge allows for reduced processing temperature which is advantageous for the implementation metal gate/high- κ dielectric gate stacks currently used in devices. In contrast to the expansive amount of knowledge regarding defect formation in Si, little is understood regarding implant-related extended defects in Ge.

Several authors have investigated the amorphization of Ge and subsequent defect formation at the amorphous-crystalline interface or end of range (EOR) with contrasting results. A few reports have shown that no EOR damage was observed,^{34,35,38,45,151} while other reports have observed the presence of small dislocation loops at the EOR and reported their properties in detail.^{20,150,172–174} Of note, it has been shown that the dissolution of these extended defects and the release of the contained interstitials has an effect on dopant activation.¹⁷⁵ These defects have been shown to be small dislocation loops which dissolve at temperatures $\leq 400^\circ\text{C}$.

Similarly, there have been mixed reports of projected range damage produced following sub-amorphizing implantations. It has been observed that projected range defects do not form following conventional implantation and annealing commonly used in semiconductor research.^{150,172,176} Although rod-like defects have been reported during H⁺, He⁺ and e⁻ irradiation at elevated temperature, it needs to be stressed that these defects were not formed using conventional dopant or self-implants, but rather high energy irradiations at increased temperature.^{177–183}

It has been observed that traditional project range defects form in Ge following ultra-shallow B⁺ implantation upon annealing. In this work, high-resolution cross-sectional transmission electron microscopy (HR-XTEM) and plan-view TEM (PTM) is used to characterize the formation and evolution of these defects.

6.2 Experimental Details

Experiments were performed on Czochralski-grown n-type Ge (001) wafers with resistivity greater than 50 Ω -cm. Samples were B⁺ implanted at 2 keV to a fluence of $1.0 \times 10^{15} \text{ cm}^{-2}$. The beam current was fixed at 1.1 mA for the B⁺ implants and the platen was held at 25°C to resist sample heating. For these conditions, the B⁺ implantation is non-amorphizing. Samples were annealed in an N₂ ambient at 400-600°C for 0.5 to 36h. HR-XTEM was completed using a JEOL 2010F to image the microstructure of specimens before and after annealing. HR-XTEM samples were prepared using a FEI DB235 focused ion beam. Final polishing was completed with a 7 kV Ga⁺ beam. PTM samples were prepared by mechanically thinning sample to ~5 μm prior to final thinning in a Fischione 1010 ion mill.

A second set of (001) Ge samples wafers were implanted with 1 MeV Ge⁺ to a fluence of $2.0 \times 10^{15} \text{ cm}^{-2}$. The implant created amorphous layer extending approximately 870 nm from the surface. Samples were annealed in an N₂ ambient at 330°C for 10 to 214 min. TEM samples were prepared using a FIB and subsequent characterization was completed on a JEOL 200CX. Weak beam dark field imaging was used with the $g_{400}(3g)$ diffracting condition.

Ge is highly susceptible to FIB damage during preparation.¹⁸⁴ The FIB ion damage is difficult to distinguish from Ge⁺ implant related defects which makes quantification difficult. To circumvent the issue of FIB damage introducing background

noise and skewing the quantification, an image processing program, ImageJ, was used for background removal. After the raw image was acquired, the image was converted to binary and the defects highlighted based on a minimum size of ~5 nm. After defects were highlighted, the defect size and population was tabulated as a function of annealing time.

6.3 Projected Range Damage

Figure 6-1 displays a bright field TEM image taken with $g_{220}(3g)$ diffraction conditions of a sample that was annealed at 500°C for 2h. From this image, small rod-like defects with an average width of approximately 3 nm are evident. These typical projected range defects¹⁶ are small in nature and are inclined with respect to the (001) Ge surface. Their general appearance is similar to that of {311}-type defects which has been observed previously in Ge following electron or light particle irradiation at elevated temperature.^{177–183} However, the observed defects in this present work are much smaller in width as those created during elevated temperature irradiations. This is the first reported observation of {311}-type defects in Ge following B⁺ implantation.

A few defects were observed to have a 'V' shape in which they are corrugated across their width. These so-called zig-zag defects were reported for ultra-low energy B⁺ implantation into Si for fluences that create a concentration of interstitials in excess of 1% of the number of atoms in the solid.⁹ In this work by Agarwal *et al.*, it was observed that zig zag defects evolve by unfauling onto additional (311) planes thereby creating the zig-zag morphology. It was also observed that the zig-zag defects were significantly more stable during annealing than traditional {311} defects which allowed them to grow to significantly larger lengths as compared to ordinary {311}-type defects.

Figure 6-2 displays a HR-XTEM image of a sample annealed for 24h at 500°C which displays several zig-zag defects in close proximity. The proximity of several zig-zag defects following a substantial anneal gives credence to the notion that zig-zag defects are also more thermally stable than ordinary {311} defects in Ge. However, the width of the defects does not appear to be substantially larger during annealing.

Further examination of the defects using HR-XTEM shows that not all defects are orientated on a {311} plane. However, a small fraction of defects are actually situated on what appears to be a {511} plane. The origin of this {511} defect is not known as it has not been reported before following implantation into Group IV materials. Indeed, the small defect width makes accurate measure of the angle of the habit plane difficult.

Figure 6-3 shows two HR-XTEM images of both {311} and {511}-type defects and the calculated misorientation with respect to the (001) plane. XTEM images from all anneals were analyzed and defect angle subsequently characterized. Defect angle quantification was aided by the use of computer software, namely ImageJ.¹⁸⁵ It is apparent that a large fraction of the observed defects lie on a plane that is oriented approximately 25° from the (001) plane while a smaller subset comprising approximately 20% of the total is oriented 16° from the (001) plane.

The spread of the measured defect angles can be attributed to a few factors. The minute dimensions of the defects inhibits the exact measurement as it is difficult to accurately mark the defect end points. In addition, the small length decreases the contrast of the defect observed in the TEM. For example, the defect are approximately 10nm in length while an XTEM sample is typically on the order of 50nm. A simple approximation yields that 20% of the through-plane thickness yields information

regarding the defect, while the other 80% of the sample masks information. However, the observed defect counts as a function of angle from the (001) plane gives confidence that the defects are a mixture of {311} and {511} defects in a 4:1 ratio. The presence of {511} defects was observed during the entire annealing sequence.

Figure 6-4 displays a series of select HR-XTEM images from samples annealed at 500°C for times ranging from 2 to 36 hr. It should be noted that XTEM images are not entirely representative of the defect concentration due to differences in sample thickness as well as the minute sampling volume. Images were chosen to represent the bulk of the sample. Additional annealing does not appear to create any coarsening of the defects. In opposition to what is observed for defect evolution in Si, the projected range damage in Ge does not evolve to form dislocation loops.⁸ In conjunction with what has been reported thus far for EOR damage in Ge, the defects appear to decrease in number and size with further annealing.^{20,172,174}

Figure 6-5 displays PTM images taken after annealing for 2 and 12h. The defects are approximately 10 ± 2 nm in length along $\langle 011 \rangle$ directions for both annealing conditions. A marginal increase in length is observed after annealing for 12h. The defects decrease in number with increasing annealing time. Defect quantification shows that there are approximately $8.07 \times 10^{10} \text{ cm}^{-2}$ and $1.24 \times 10^{10} \text{ cm}^{-2}$ defects following 2 h and 12 h at 500°C, respectively. Defect dissolution was observed for anneals in excess of 500°C for 36 hr.

Select samples were also annealed for various times for temperatures between 400 and 600°C. In conjunction with electrical data, it has been shown that {311} defect formation or dissolution does not have any substantial effect on B activation in Ge.

Therefore, it is assumed that the defects are not primarily composed of B atoms, but rather composed of Ge interstitials. Following dissolution and presumably a release of excess Ge interstitials, no change in the number of active B carriers is observed which suggests that there is minimal interaction between these excess interstitials and B atoms. However, the density and size of the defect is quite small which limits the total number of trapped Ge interstitial or B atoms that may be released during dissolution.

6.4 End of Range Damage

Figure 6-6 shows XTEM images taken with $g_{220}(3g)$ diffraction condition of EOR damage created by a 1 MeV Ge^+ implant to a fluence of $2.0 \times 10^{15} \text{ cm}^{-2}$ following annealing at 330°C for various times. The defects have formed just below the original amorphous-crystalline interface at a depth of approximately 870 nm from the surface. The defects show contrast in the form of approximately spherical white dots. Reports of EOR in Ge by Koffel *et al.* have shown that defects of similar contrast are composed of self-interstitials as determined by X-ray diffraction techniques.¹⁷⁴ Presumably, the observed defects in this work are composed of self-interstitials as well. The small nature of the defects makes direct identification of the defect difficult.

Figure 6-7 displays graphs of defect density and defect size as a function of annealing time at 330°C . The contrast created by the defects is comparable to the damage imparted by FIB preparation and makes absolute defect quantification difficult. Background noise was subtracted using ImageJ as described in previous sections. The defect size was determined by measuring the diameter and assuming the defects are spherical in nature.

In accordance with previous reports of EOR in Ge, the defects are small as they are no larger than approximately 10 nm in diameter at their largest.^{20,174} With

increasing annealing time, the defect density decreases with the average defect size increasing for times less than 50 min. For times greater than approximately 50 min, the defect size also decreases. The combination of decreasing defect size and density suggests a non-conservative evolution of defects where the overall population of trapped self-interstitials decreases with time. These findings are in agreement with previous reports of EOR evolution in Ge.^{20,174}

6.5 Discussion

Previous works have investigated high-fluence B⁺ implantations in pure Ge, but extended defects were not observed; rather only a disordered microstructure.³⁸ In addition, Crosby *et al.* studied the formation of extended defects in Si_xGe_(1-x) and found that {311} defects did not form for Ge concentrations greater than 25% which was attributed to the reduced bond strength of Ge.¹⁷⁶ The first observation of projected range damage may be attributed to the surface proximity of these shallow B⁺ implants. As has been discussed in previous chapters, the Ge surface is regarded as a vacancy sink while reflecting interstitials which would increase extended defect formation.⁵⁰

Similar to previous published results of implant-related damage in Ge, the observed projected range and EOR defects were much smaller in size than what is typically observed in Si. In addition, the defects were not observed to coarsen appreciably in during annealing. The results suggest that defect formation and evolution is not as significant in Ge as compared to Si where it has been shown to have a profound effect on B activation¹³ as well as on B diffusion⁶⁷.

A possible reason for this occurrence is due to the dominant point defect in Ge being the vacancy rather than the interstitial as it is in Si.¹⁶⁵ It has been shown in previous chapters that self-interstitials have limited mobility at the investigated

temperatures for this work. It can be concluded that this lack of mobility hinders the ability of interstitials to coalesce into extended defects. Likewise, it can also be concluded that interstitials may have a higher probability of recombining with a mobile vacancy prior to forming an extended defect. Further evidence that may show this to be true was produced by Boninelli *et al.* where they showed a dependence of EOR formation and dissolution on Ge implant energy.¹⁸⁶ The increase of EOR damage with increasing energy could be attributed to the separation of interstitial and vacancy profiles during implantation. For high energy implants, the forward momentum of the ion drives interstitials deeper into the solid while an excess vacancy population remains near the surface. This separation of point defects could allow for decreased recombination and increased EOR damage formation. Similar energy dependence on EOR results were found in this work, but were not reported.

The reduced amorphization threshold of Ge is likely a primary factor regarding the reduced number and size of EOR defects in Ge. For Ge, the number of vacancies required to produce an amorphous layer is reduced.^{20,21} Because of this, there are less self-interstitials remaining at the end of range following regrowth. The reduced number of self-interstitials available for extended defect formation has a direct influence on the size and number of EOR defects created.

6.6 Summary

The formation and evolution of projected range and end of range damage in Ge has been investigated. For both projected range and EOR defects in Ge, the damage evolution has been shown to be non-conservative where the total number of trapped interstitials decreases with annealing. The relatively low concentration of implant-related

defects in Ge has been attributed to the quick diffusion of vacancies and lack of mobile interstitials in Ge.

The first observation of rod-like defects were reported following a non-amorphizing 2 keV B⁺ implant at a fluence of $1.0 \times 10^{15} \text{ cm}^{-2}$. The defects were determined to be primarily of a {311}-type with a small subset occupying a {511} plane. Zig-zag defects were also observed across the annealing range. The rod-like defects were observed to not undergo an appreciable increase in length or width during annealing with the average length and width being approximately 10 nm and 3 nm, respectively. No dislocation loops were observed following the dissolution of rod-like defects. The dissolution of the rod-like defects did not have an appreciable effect on activation.

The formation and evolution of EOR damage in Ge was monitored as a function of annealing time at 330°C following a 1 MeV Ge⁺ implant to a fluence of $2.0 \times 10^{15} \text{ cm}^{-2}$. Defects were observed to initially increase in size for times less than approximately 50 min and decrease in size for longer anneals. The defect density was observed to decrease with increasing annealing time.

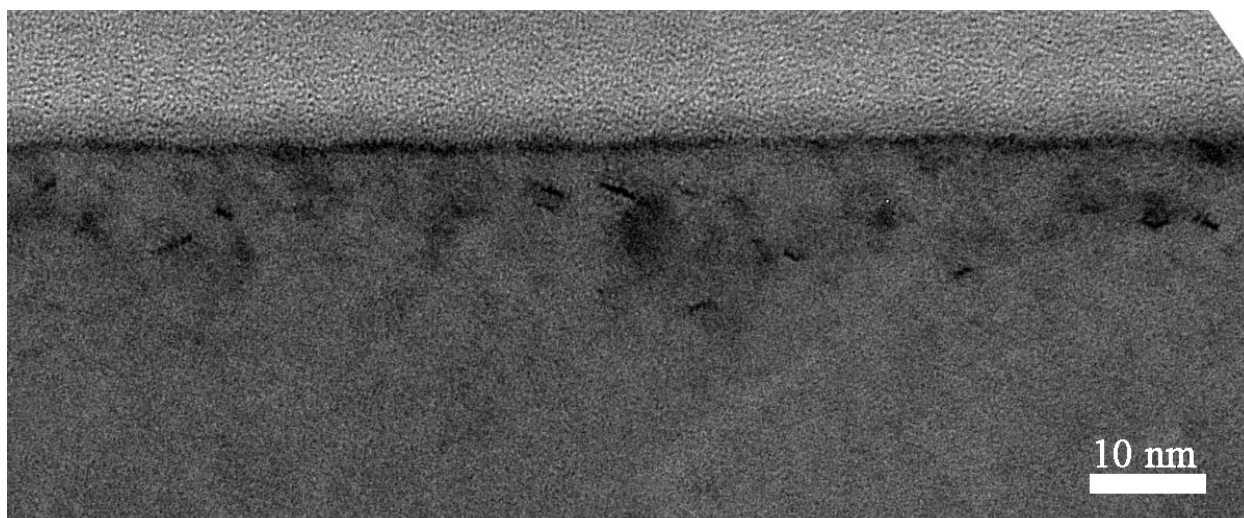


Figure 6-1. Bright field XTEM image taken with $g_{220}(3g)$ diffraction condition of projected range damage created by a 2 keV B^+ implant to a fluence of $1.0 \times 10^{15} \text{ cm}^{-2}$ following annealing at 500°C for 2 h times ranging from 2 to 36h.

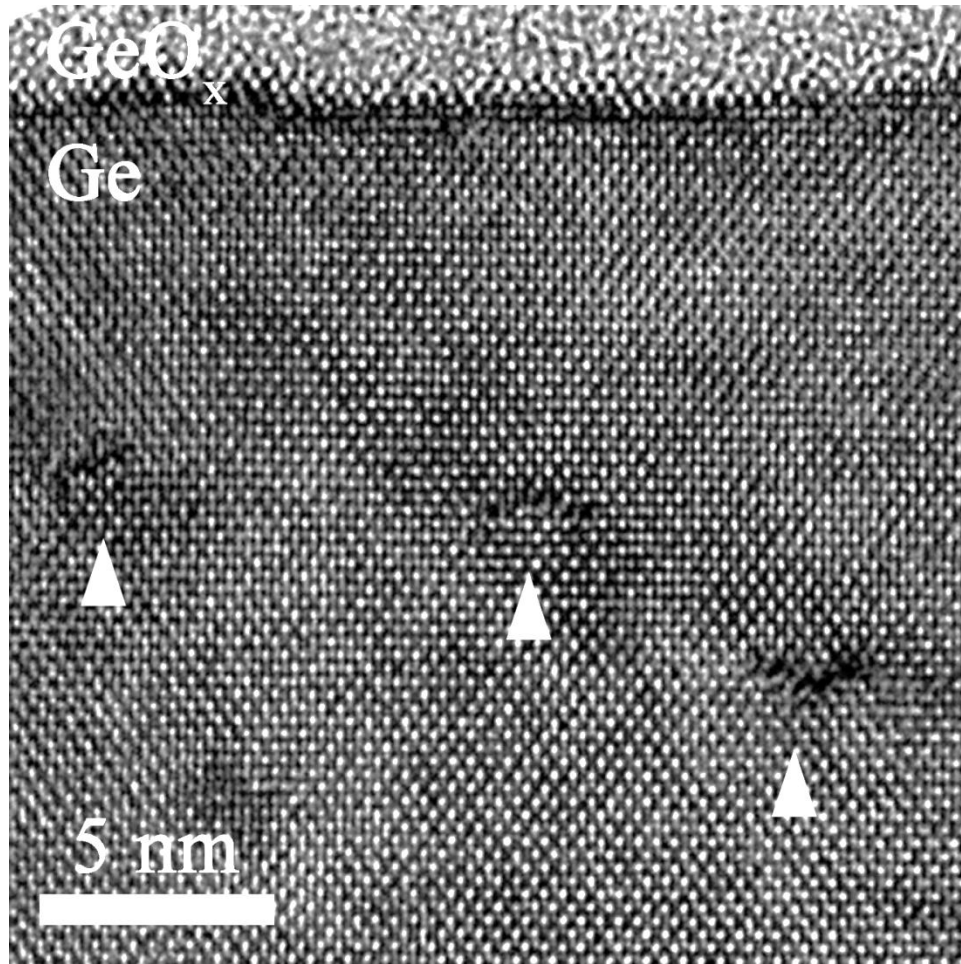


Figure 6-2. HR-XTEM image of projected range damage created by a 2 keV B^+ implant to a fluence of $1.0 \times 10^{15} \text{ cm}^{-2}$ following annealing at 500°C for 24 h. Several zig-zag defects are evident.

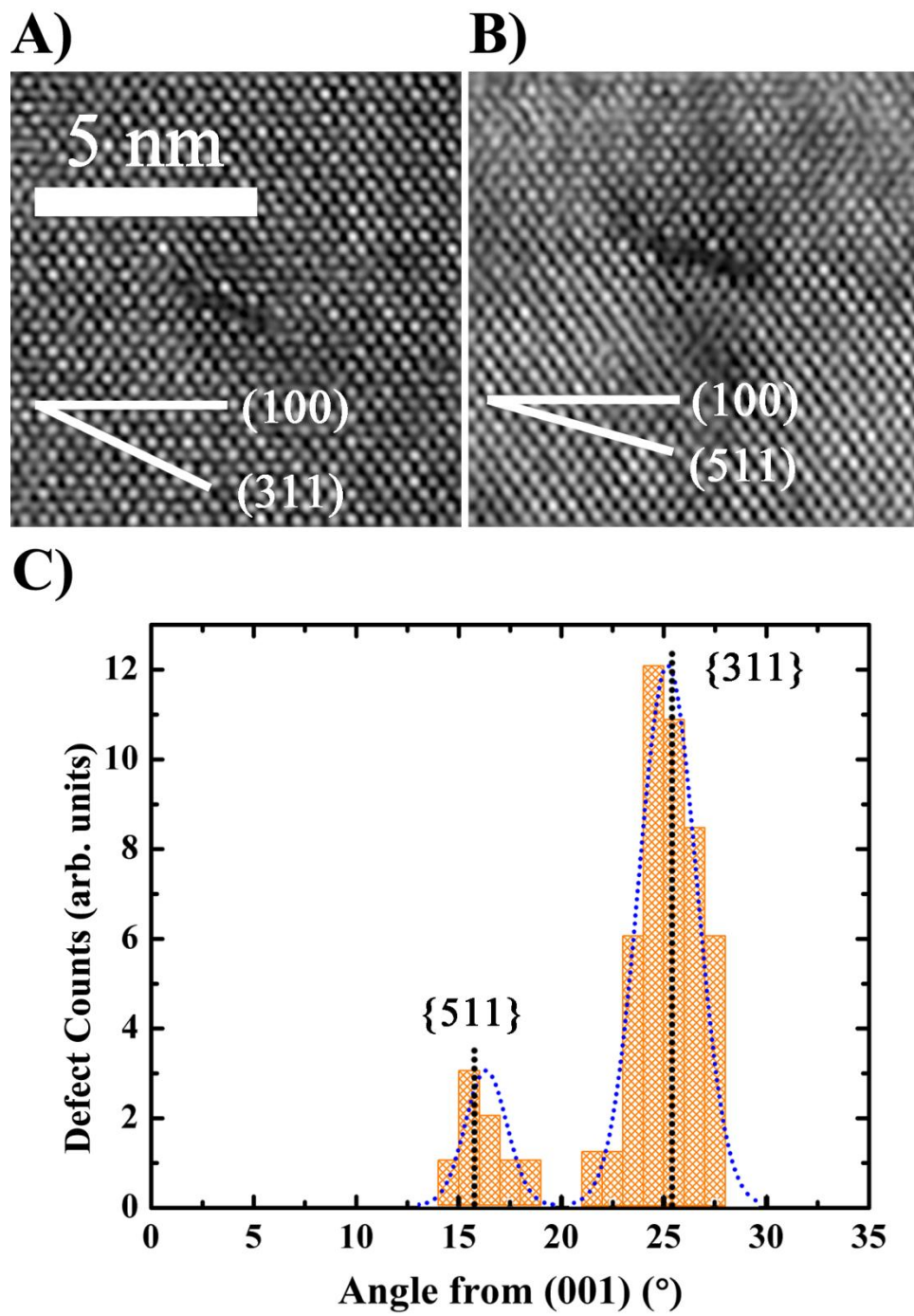


Figure 6-3. Defect orientations of projected range damage in Ge. HR-XTEM images of A) {311} and B) {511}-type defects. C) Histogram displaying their relative abundance.

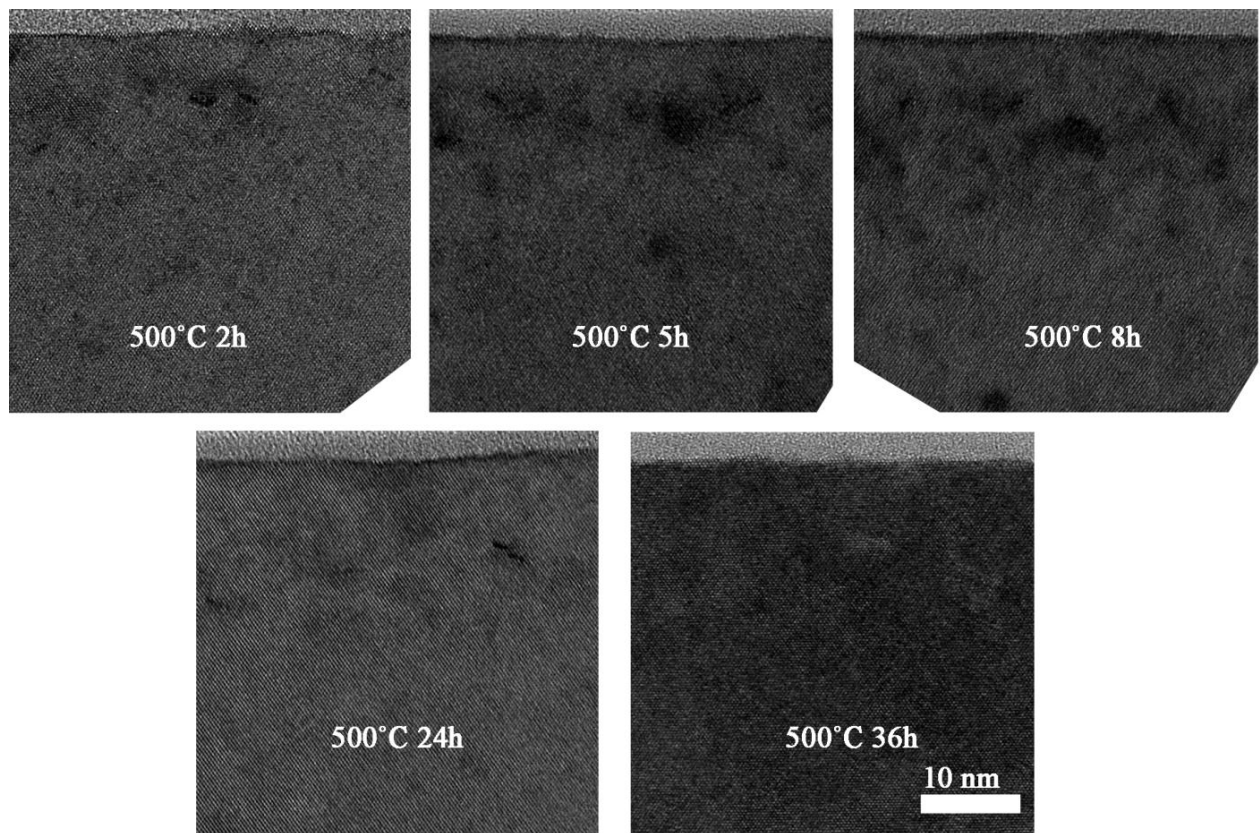


Figure 6-4. XTEM images of projected range damage created by a 2 keV B⁺ implant to a fluence of $1.0 \times 10^{15} \text{ cm}^{-2}$ following annealing at 500°C for times ranging from 2 to 36 h.

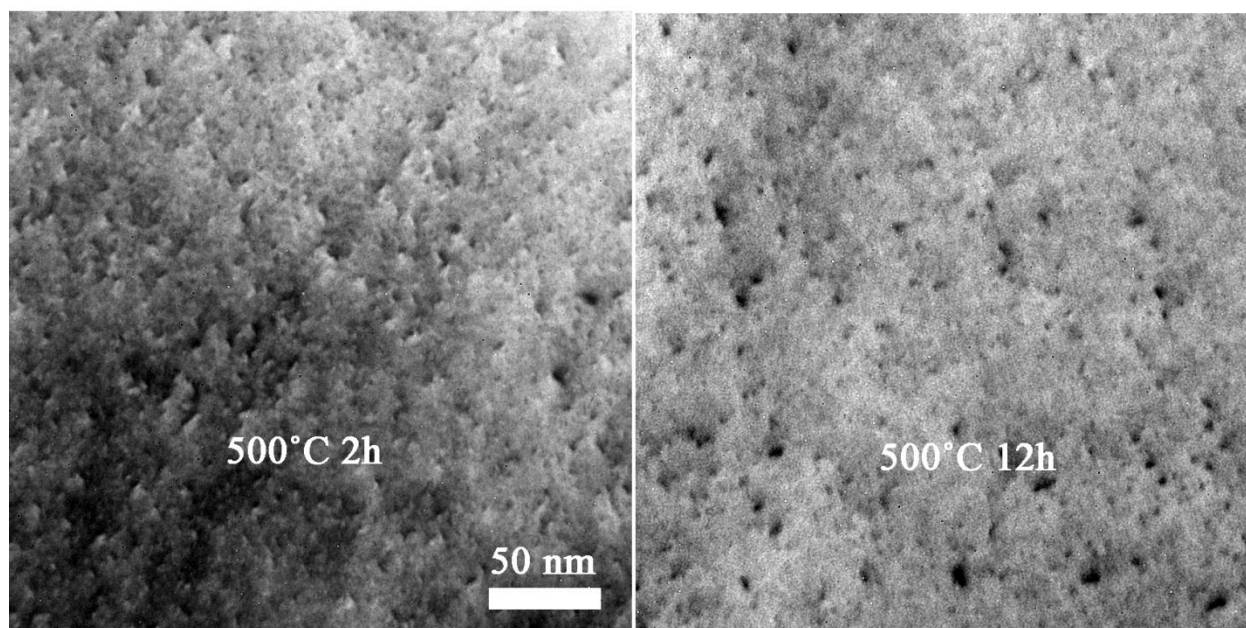


Figure 6-5. Bright field PTEM images taken with $g_{220}(3g)$ diffraction condition of projected range damage created by a 2 keV B^+ implant to a fluence of $1.0 \times 10^{15} \text{ cm}^{-2}$ following annealing at 500°C for 2 h and 12 h.

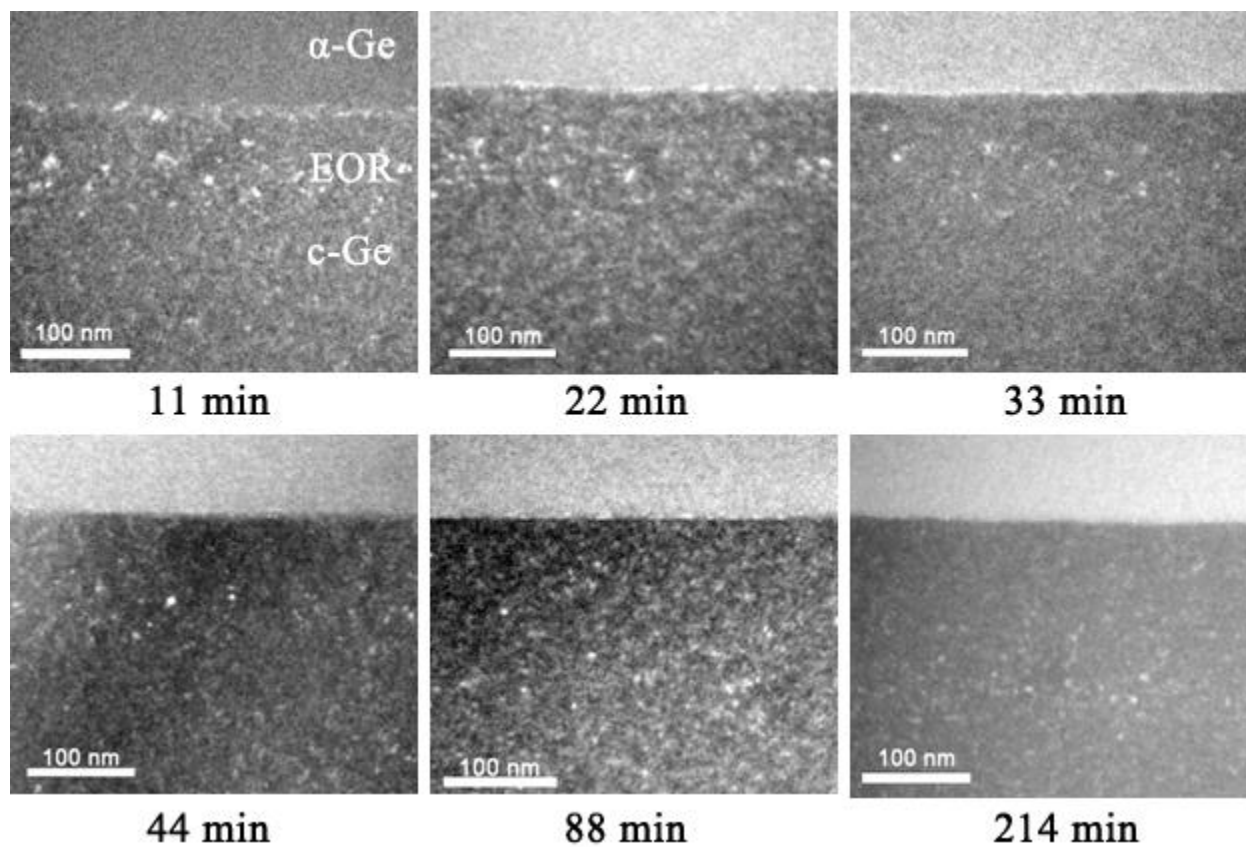


Figure 6-6. XTEM images taken with $g_{220}(3g)$ diffraction condition of EOR damage created by a 1 MeV Ge^+ implant to a fluence of $2.0 \times 10^{15} \text{ cm}^{-2}$ following annealing at 330°C for various times.

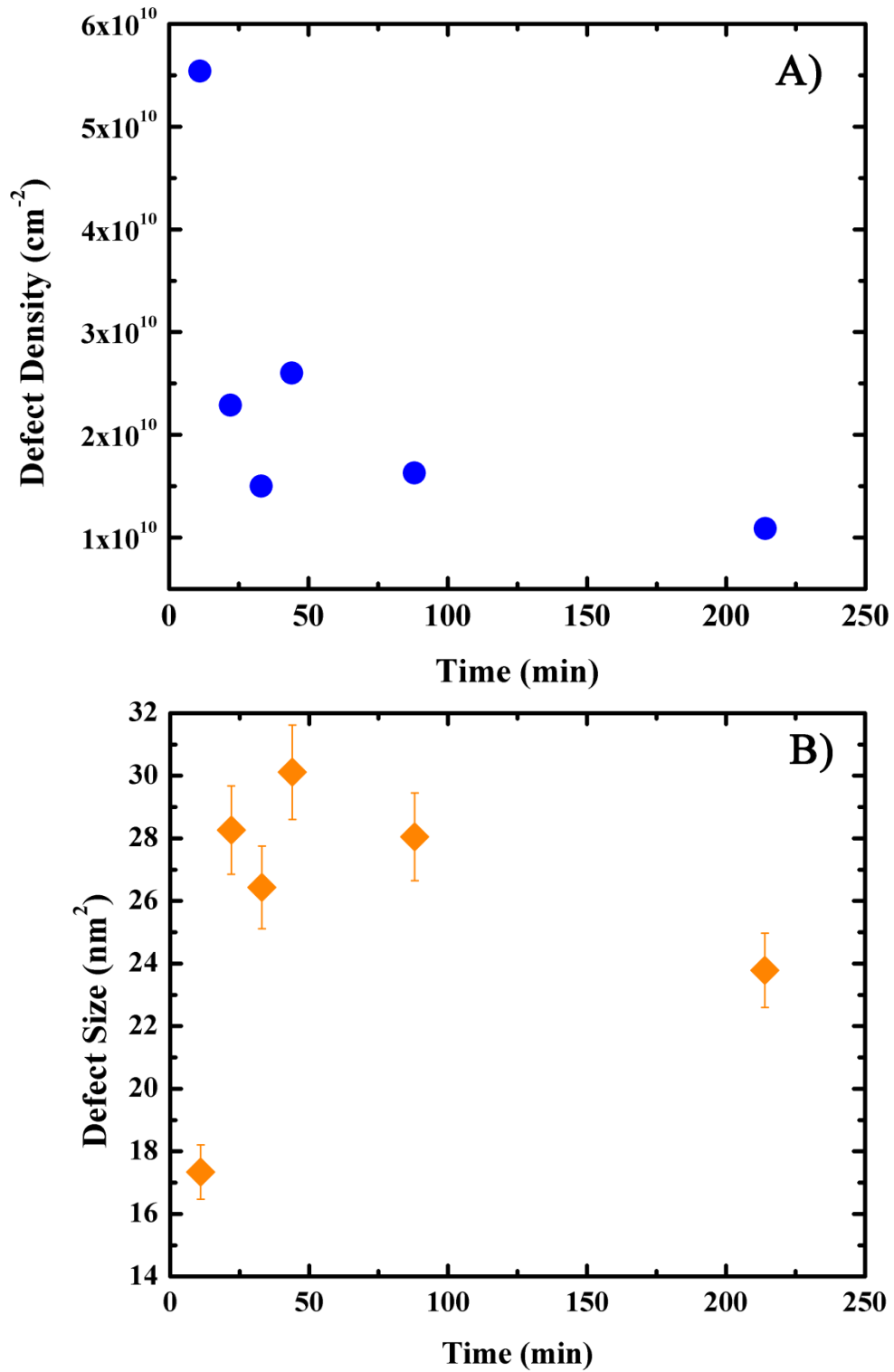


Figure 6-7. EOR damage created by a 1 MeV Ge⁺ implant to a fluence of $2.0 \times 10^{15} \text{ cm}^{-2}$ as a function of annealing time at 330°C. A) average defect density and B) average defect size.

CHAPTER 7

CONCLUSIONS AND FUTURE WORK

The implantation and activation of ultra-shallow B⁺ implants in Ge was thoroughly investigated. Prior to this work, very little research was conducted on these technologically relevant ion implants. It can be assumed that the dearth of information presently available prior to this work is related to the difficulty in measuring the electrical properties of these ultra-shallow layers as evidenced in this document. The advent of the micro Hall effect and micro four point probe techniques has pushed the scaling of the metrology tools used to characterize these layers in conjunction with the physical scaling of these implants which has allowed for their accurate characterization.

The activation behavior of ultra-shallow B⁺ implants in Ge has been determined to follow anomalous activation trends as compared to what has been previously published regarding higher energy implants in Ge as well as B activation in Si. It has been observed that independent of implanted fluence, a large fraction of the implanted B is rendered inactive for implants into both crystalline and preamorphized Ge. Ion beam analysis was used to verify the micro Hall effect results and it was determined that a large fraction of B is in fact situated in off-lattice positions following annealing. The results also suggest that a preferred site for inactive B does not exist.

The effect of annealing has been shown to have little effect in increasing or decreasing the fraction of activated dopant. Similar to results reported for higher energy B⁺ implants in Ge, slight changes in sheet resistance and activation were observed as a function of annealing temperature between 400 and 600°C; however, the changes did not significantly affect the activation values. High temperature isochronal anneals were shown to induce a strong deactivation at temperatures in excess of 650°C and 750°C for

preamorphized and crystalline samples, respectively. The deactivation is believed to be due to the B falling out of solution due to the concentration in excess of the chemical solubility limit. Across all investigated temperatures and times investigated, a large fraction of inactive B remained for both crystalline and preamorphized samples.

The activation behavior of B⁺ implants in Ge has been shown to be independent of the implanted fluence and as such does not exhibit a single electrical solubility across the investigated fluence range. With increasing fluence, the percent of activated dopant atoms remains fixed for a given energy which suggests that the activation behavior of B in Ge is related to the fluence-dependent damage imparted to the crystal. The anomalous activation behavior of ultra-shallow B⁺ implants is believed to be correlated with the relatively immobile B species in Ge and the relatively large population of Ge interstitials created during implantation. The low diffusivity of B in Ge restricts its ability to travel to and to combine with a vacant lattice site. The B⁺ implantation process creates far more interstitials per incoming ion which creates an atmosphere of excess interstitials in close proximity with the implanted B atom. The surface proximity is expected to further increase the interstitial super-saturation as the surface is known to act as a sink for vacancies. The competition between B atoms and interstitials decreases the probability that B atoms will be able to recombine with a vacant site.

For the first time, it has been shown that extended defects form in Ge following sub-amorphizing B⁺ implantation as confirmed by cross-sectional TEM analysis. The defects were observed to be predominately of the {311}-type with a small fraction having a {511} habit plane. In comparison to {311} defects in Si, the defects are smaller in stature and were not observed to coarsen or to evolve into dislocation loops. The

defects were observed to form following an anneal at 500°C for 0.5hr with dissolution occurring after 36 hr. Upon dissolution, no change in activation was observed which suggests that defects are not composed of B atoms.

End of range damage produced by amorphizing Ge⁺ implants was investigated. It was observed that end of range damage was formed following a high energy self-implantation and subsequent annealing for various times at 330°C. In contrast to Si, the defects were small in stature and not observed to coarsen appreciably, but rather the number of trapped interstitials appeared to decrease with annealing time. An increase in size was observed initially for short annealing times with a decrease in size for long anneals. The number of defects continually decreased with increasing annealing times.

In this work, the activation and implant-related damage results have shown that dopant-defect interactions for ultra-shallow B⁺ implants in Ge differs greatly from that of Si. With the vacancy being the dominant point defect, the associated physical models of dopant-defect interactions in Ge will need to be adjusted significantly for future experimentation.

The results published in this work have documented several new findings regarding the implantation and activation of ultra-shallow B⁺ implants in Ge. Although attempted for this work, but ultimately not to fruition, the use of vacancy engineering may yield important information regarding the activation of these technologically relevant implants. Vacancy engineering involves a high energy (a few MeV) implant to introduce an excess concentration of vacancies near the surface with excess interstitials driven further into the bulk due to forward momentum transfer. It has been used successfully to reduce TED of B in Si. The excess vacancies introduced should allow

for increased activation or decreased projected range damage and would be an interesting experiment to complete.

In addition, further implementation of ion beam analysis or positron annihilation spectroscopy could be employed to further analyze the resulting point defect populations following annealing and during subsequent processing. Understanding the evolution of the point defect population would prove fruitful in grasping the dopant-defect interactions present in Ge.

Lastly, the implementation of high-resolution x-ray diffraction (HRXRD) could be employed to understand the local changes in lattice constant following B⁺ implantation and processing. HRXRD has been employed for several material systems to understand the strain associated with dopants or dopant clusters. Monitoring the strain induced by B⁺ implantation and with subsequent processing could allow for the use of simulations to produce information regarding the inactive B concentration.

APPENDIX EFFECT OF IMPLANT CONDITIONS ON B ACTIVATION

A.1 Variable Implantation Conditions

It is well known that a variety of implantation parameters, such as ion mass and energy, target temperature, ion flux, etc. can have a profound effect on the resulting lattice damage and microstructure of the target.^{187,188} As evidenced in this document, very little research has been conducted regarding ultra-shallow B⁺ implants in Ge and this is especially true in terms of implant parameters. Thus, the effects of varying beam current on the clustering and electrical activation behavior of ultra-shallow B⁺ implants in Ge is investigated.

A.2 Experimental Methods

Experiments were performed on Czochralski-grown n-type Ge (001) wafers with resistivity greater than 50 Ω -cm. A set of samples were diced and B⁺-implanted at 2 keV to a fluence of 5.0×10^{14} cm⁻² with beam current varying from 0.4 to 6.4 mA. The beam size is estimated to be 180 cm² which yields an ion flux range of 1.38×10^{13} to 2.21×10^{14} ions/(s-cm²) for 0.4 mA and 6.4 mA, respectively. During B⁺ implantation, the platen was held at 25°C. Samples were processed in a Heatpulse 4100 rapid thermal annealer (RTA) in N₂ ambient at 400°C for 60s to activate the implanted B. High-resolution cross-sectional transmission electron microscopy (HR-XTEM) was completed using a JEOL 2010F to image the microstructure of specimens before and after annealing. TEM samples were prepared using a FEI DB235 focused ion beam.

Electrical characterization was completed using a CAPRES microRSP M-150 M4PP with Au-coated probes, a probe spacing of 20 μ m, and a permanent magnet with a magnetic flux density of 0.475 T. Hall sheet number (n_H) and mobility values (μ_H)

were adjusted to obtain the carrier sheet number (n_s) and drift mobility (μ_d) by using a scattering factor (r_H) of 1.21 as determined empirically by Mirabella *et al.*³¹ The carrier density and drift mobility are related to the Hall values by $n_s = n_H \times r_H$ and $\mu_d = \mu_H / r_H$, respectively.

A.3 Results and Discussion

In Figure A-1, the sheet resistance, R_s , is plotted as a function of beam current for 2 keV B⁺ implants to a dose of $5.0 \times 10^{14} \text{ cm}^{-2}$ after annealing 400°C for 60s. A trend of decreasing R_s with increasing beam current is observed across the investigated range. At 6.4 mA, the measured R_s value is 675.2 Ω/sq as compared to 931.5 Ω/sq at 0.4 mA. Interestingly, the decrease in R_s can be explained by an increase in activation as seen in Figure A-2. At 6.4 mA, the n_s was $4.55 \times 10^{13} \text{ cm}^{-2}$ which is an increase of 76% from the lowest current. In Figure A-3, the drift mobility as a function of beam current is shown. Due to the increase in ionized dopants, the drift mobility decreases with current to a minimum of 203.2 $\text{cm}^2/\text{V-s}$ which is in good agreement with other results in this doping regime.³¹

Despite the increase in carriers with increasing beam current, the overall activation of the samples is far from complete activated with the highest value achieved at 11.4%.. This finding is not surprising given the abundance of data garnered from various processing conditions that yielded similar values.

The microstructure of the samples was characterized using HR-XTEM both as-implanted and post anneal to ascertain the presence of any increased damage created by the high beam current implantation. Figure A-4 shows an image of the highest beam current sample implanted at 6.4 mA without any subsequent annealing. The samples implanted at 0.4 and 6.4 mA both appeared unremarkable with no discernible difference

between the samples as-implanted and post anneal. The presence of any amorphization was not observed in the as-implanted case and extended defects were not observed in the annealed case for any sample. Although not discernible via HR-XTEM, the presence of sub-microscopic damaged or amorphous regions is certainly possible. The presence of these sub-microscopic amorphous regions would allow for increased B activation upon annealing as is observed in this work. Previous studies have shown that B⁺ implantation into c-Ge can yield activation values comparable to PA-Ge if the fluence is great enough²⁴ or if the platen is held at reduced temperature.²³ In both cases, B⁺ implantation induces amorphization which yields increased activation upon annealing.

For Si, it is well-known that varying the beam current during implantation can significantly alter the resulting microstructure through ion beam induced recrystallization or amorphization.^{189,190} At elevated temperatures, a subtle change in the ion flux is capable of influencing the point defect environment surrounding the crystalline-amorphous interface in such a way that it may recrystallize or further amorphize the layer depending on an increase or decrease in beam current, respectively. However, it should be noted that the observed increase in active carriers is not believed to be due to any beam heating effects due to the platen being held at room temperature during the implantation. In addition, the relatively low implant energy and low fluence reduces the total power deposited into the sample.

Several studies regarding ion beam induced recrystallization and amorphization have been completed with Ge which have reported similar findings.^{191–193} Notably, Sigurd *et al.* have reported that for B⁺ ions in Ge, the lattice disorder produced is ten

times higher than what is observed in Si at room temperature.¹⁹¹ These results are likely explained through the lower amorphization threshold of Ge as compared to Si.²¹ However, for light ions such as B, the amorphous layer is not as thick nor is amorphization observed at the projected range of the ion as predicted by simulations for heavier ions, but rather occurs closer to the surface.²⁰

A.4 Summary

The reduced amorphization threshold of Ge with respect to Si likely explains the observed activation behavior following B⁺ implantation at variable beam currents. The dilute damage cascades created during B⁺ implantation does not allow for the formation of a distinct amorphous layer, but locally, it is assumed that amorphous pockets are formed during implantation. During annealing, these amorphous pockets allow for increased B activation.

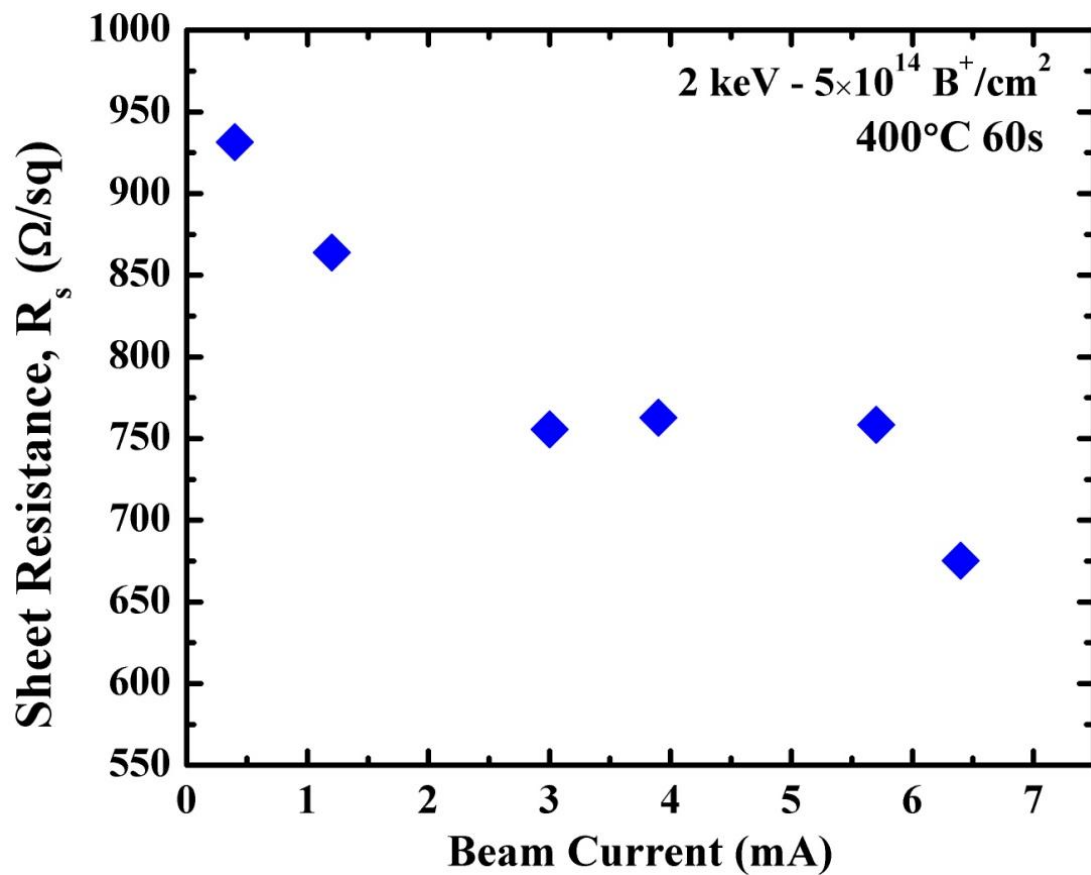


Figure A-1. Measured sheet resistance (R_s) after annealing at 400 °C for 60 s as a function of beam current implanted at 2 keV to a fluence of $5.0 \times 10^{14} \text{ cm}^{-2}$ into crystalline Ge.

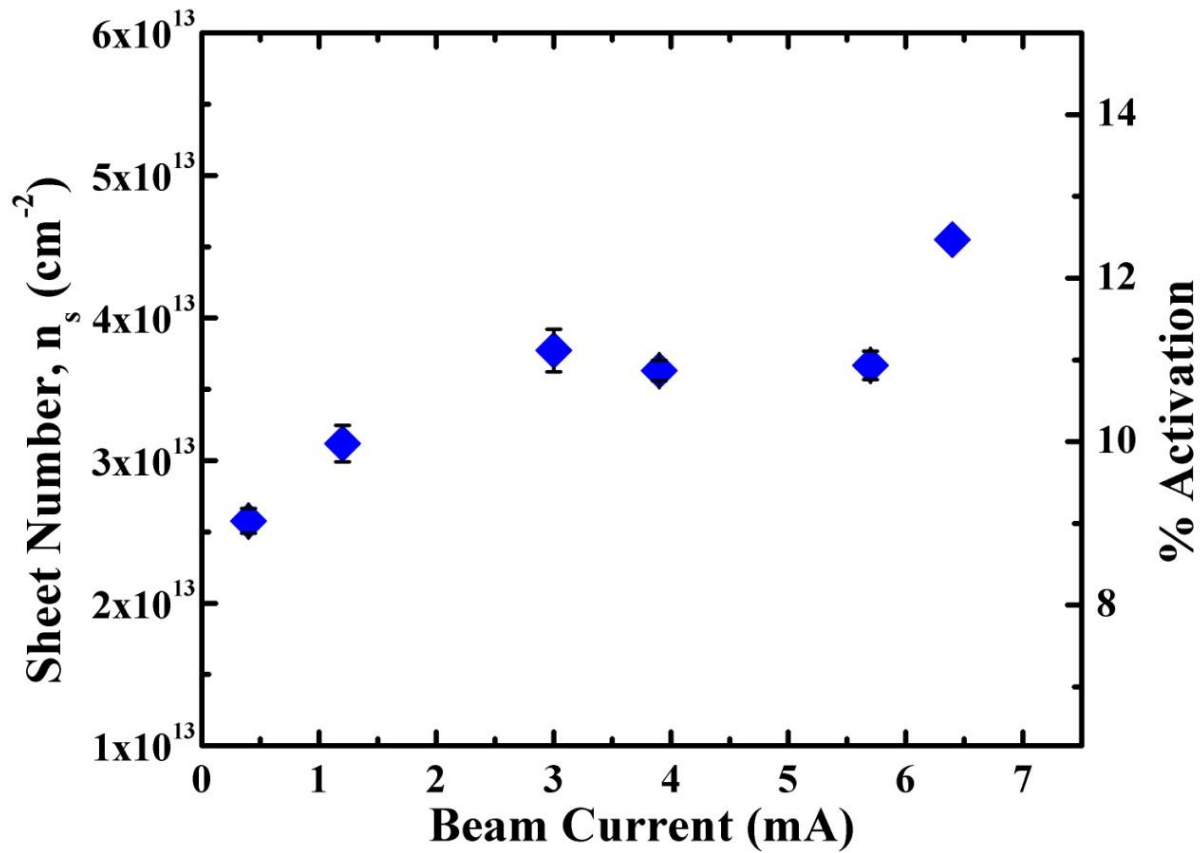


Figure A-2. Measured sheet number (n_s) and percent electrical activation as a function of beam current implanted at 2 keV to a fluence of $5.0 \times 10^{14} \text{ cm}^{-2}$ into crystalline Ge after annealing at 400 °C for 60s.

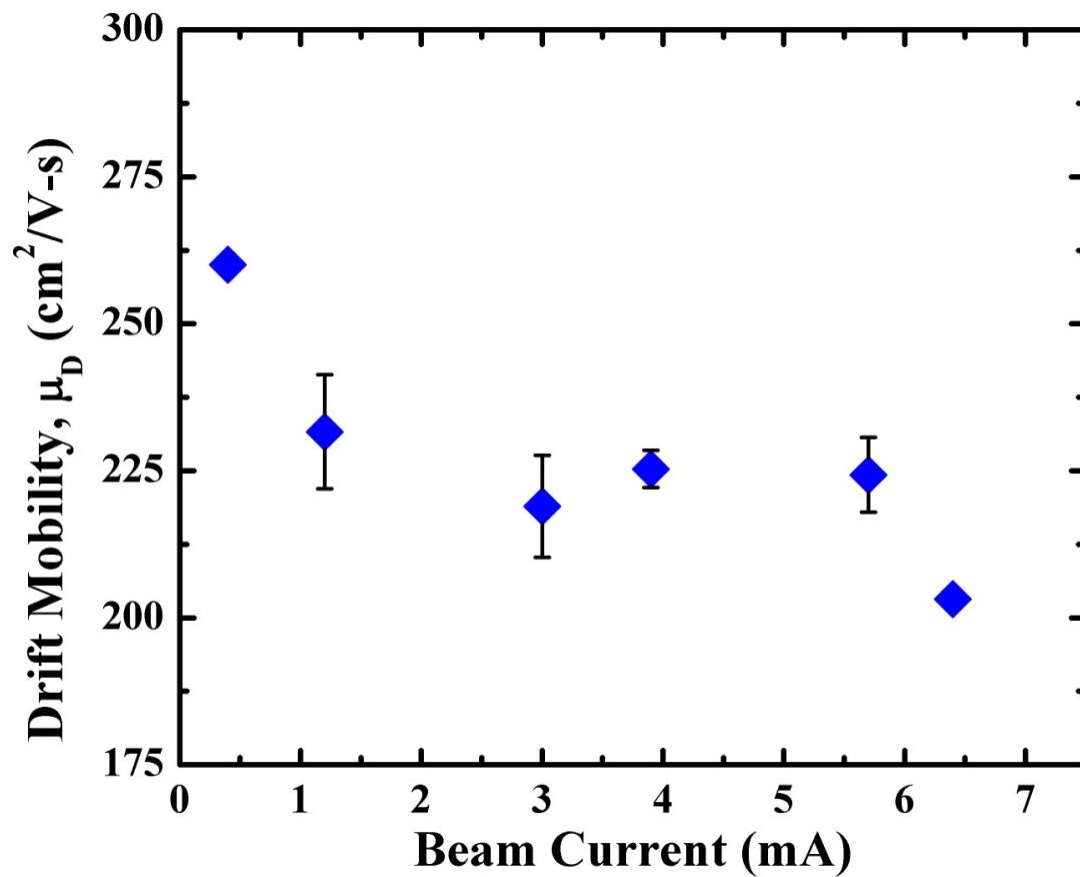


Figure A-3. Measured drift mobility (μ_D) as a function of beam current implanted at 2 keV to a fluence of $5.0 \times 10^{14} \text{ cm}^{-2}$ into crystalline Ge after annealing at 400 °C for 60s.

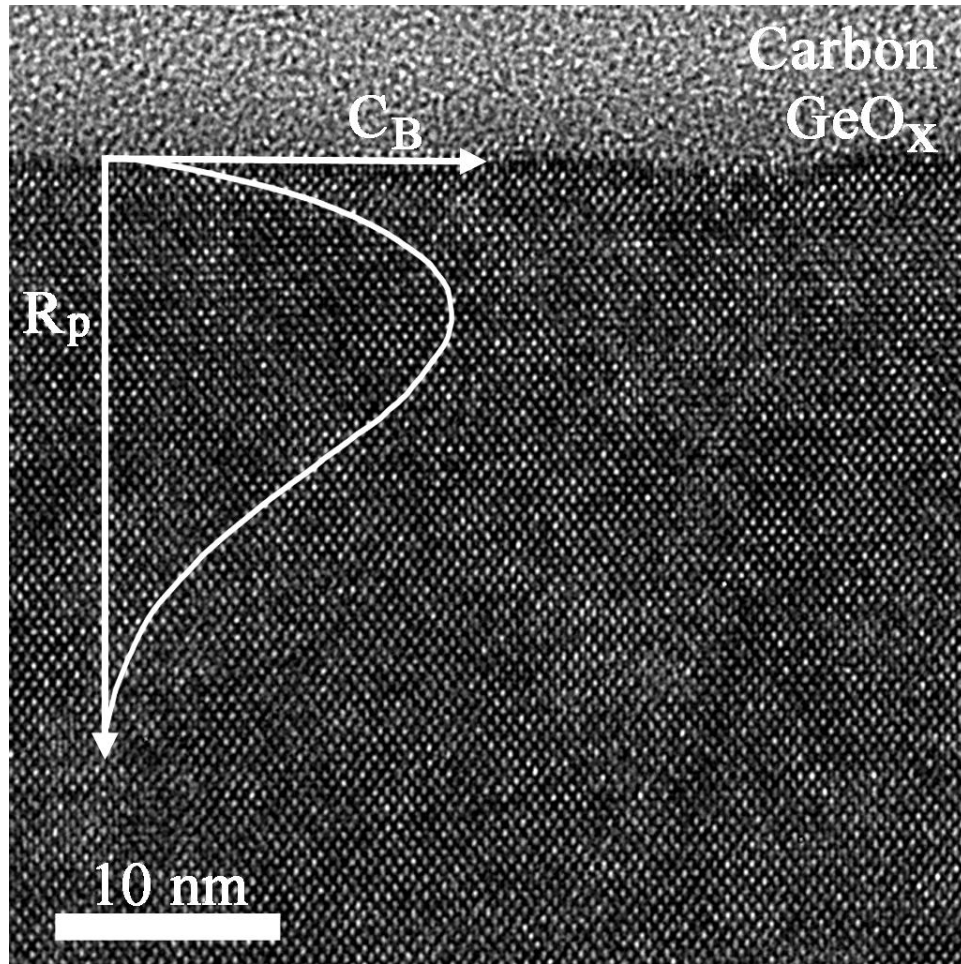


Figure A-4. HR-XTEM micrograph of an as-implanted crystalline Ge sample B^+ implanted at 2 keV to $5.0 \times 10^{14} \text{ cm}^{-2}$ at a beam current of 6.4 mA showing a $2.9 \pm 0.3 \text{ nm}$ surface GeO_x layer and no evident implant damage or amorphization present near the projected range, R_p . A simulation of the B profile is overlaid on the image.

LIST OF REFERENCES

- ¹ G.E. Moore, *Electronics* **38**, 114 (1965).
- ² S.M. Sze and K.K. Ng, *Physics of Semiconductor Devices* (John Wiley and Sons, 2007).
- ³ J.F. Gibbons, *Proceedings of the IEEE* **56**, 295 (1968).
- ⁴ J.F. Gibbons, *Proceedings of the IEEE* **60**, 1062 (1972).
- ⁵ E. Chason, S.T. Picraux, J.M. Poate, J.O. Borland, M.I. Current, T. Diaz de la Rubia, D.J. Eaglesham, O.W. Holland, M.E. Law, C.W. Magee, J.W. Mayer, J. Melngailis, and A.F. Tasch, *Appl. Phys. Rev.* **1997**, 2 (1997).
- ⁶ J.S. Williams, *Mater. Sci. and Eng.* **A253**, 8 (1998).
- ⁷ D.J. Eaglesham, P.A. Stolk, H.-J. Gossmann, and J.M. Poate, *Appl. Phys. Lett.* **65**, 2305 (1994).
- ⁸ D.J. Eaglesham, P.A. Stolk, H.-J. Gossmann, T.E. Haynes, and J.M. Poate, *Nucl. Instrum. Methods Phys. Res. B* **106**, 191 (1995).
- ⁹ A. Agarwal, T.E. Haynes, D.J. Eaglesham, H.-J. Gossmann, D.C. Jacobson, J.M. Poate, and Y.E. Erokhin, *Appl. Phys. Lett.* **70**, 3332 (1997).
- ¹⁰ A. Agarwal, H.-J. Gossmann, D.J. Eaglesham, L. Pelaz, D.C. Jacobson, T.E. Haynes, and Y.E. Erokhin, *Appl. Phys. Lett.* **71**, 3141 (1997).
- ¹¹ A. Agarwal, H.-J. Gossmann, D.. Eaglesham, L. Pelaz, S.. Herner, D.. Jacobson, T.. Haynes, and R. Simonton, *Mater. Sci. Semicond. Process.* **1**, 17 (1998).
- ¹² J. Li and K.S. Jones, *Appl. Phys. Lett.* **73**, 3748 (1998).
- ¹³ A.D. Lilak, M.E. Law, L. Radic, K.S. Jones, and M. Clark, *Appl. Phys. Lett.* **81**, 2244 (2002).
- ¹⁴ N.E.B. Covern, B. Colombeau, J. Benson, A.J. Smith, W. Lerch, S. Paul, T. Graf, F. Cristiano, X. Hebras, and D. Bolze, *Appl. Phys. Lett.* **86**, 101905 (2005).
- ¹⁵ L. Romano, A.M. Piro, V. Privitera, E. Rimini, G. Fortunato, B.G. Svensson, M. Foad, and M.G. Grimaldi, *Nucl. Instrum. Methods Phys. Res. B* **253**, 50 (2006).
- ¹⁶ K.S. Jones, S. Prussin, and E.R. Weber, *Appl. Phys. A* **45**, 1 (1988).

- ¹⁷ G. Hobler and G. Otto, *Mater. Sci. Semicond. Process.* **6**, 1 (2003).
- ¹⁸ U. Yarkulov, *Rad. Effect.* **100**, 11 (1986).
- ¹⁹ U. Yarkulov, *Rad. Effect.* **103**, 135 (1987).
- ²⁰ A. Claverie, S. Koffel, N. Cherkashin, G. Benassayag, and P. Scheiblin, *Thin Solid Films* **518**, 2307 (2010).
- ²¹ S. Koffel, P. Scheiblin, A. Claverie, and G. Benassayag, *J. Appl. Phys.* **105**, 013528 (2009).
- ²² D.P. Hickey, "Ion Implantation Induced Defect Formation and Amorphization in the Group IV Semiconductors: Diamond, Silicon and Germanium", University of Florida, 2007.
- ²³ E. Bruno, G. Impellizzeri, S. Mirabella, A.M. Piro, A. Irrera, and M.G. Grimaldi, *Mater. Sci. and Eng. B* **154-155**, 56 (2008).
- ²⁴ B.R. Yates, B.L. Darby, N.G. Rudawski, K.S. Jones, D.H. Petersen, O. Hansen, R. Lin, P.F. Nielsen, and A. Kontos, *Mater. Lett.* **65**, 3540 (2011).
- ²⁵ W. Martienssen and H. Warlimont, editors, *Springer Handbook of Condensed Matter and Materials Data* (Springer, Heidelberg ; New York, 2005).
- ²⁶ L. R. Bidwell, *J. of the Less Common Metals* **20**, 19 (1970).
- ²⁷ R. Olesinski and G. Abbaschian, *J. of Phase Equilibria* **5**, 476 (1984).
- ²⁸ S. Uppal, A.F.W. Willoughby, J.M. Bonar, A.G.R. Evans, N.E.B. Cower, R. Morris, and M.G. Dowsett, *J. Appl. Phys.* **90**, 4293 (2001).
- ²⁹ S. Uppal, A.F.W. Willoughby, J.M. Bonar, A.G.R. Evans, N.E.B. Cower, R. Morris, and M.G. Dowsett, *Physica B* **308-310**, 525 (2001).
- ³⁰ S. Uppal, A.F.W. Willoughby, J.M. Bonar, N.E.B. Cower, T. Grasby, R.J.H. Morris, and M.G. Dowsett, *J. Appl. Phys.* **96**, 1376 (2004).
- ³¹ S. Mirabella, G. Impellizzeri, A.M. Piro, E. Bruno, and M.G. Grimaldi, *Appl. Phys. Lett.* **92**, 251909 (2008).
- ³² V.M. Gusev, M.I. Guseva, E.S. Ionova, A.N. Mansurova, and C.V. Starinin, *Phys. Stat. Sol. A* **21**, 413 (1974).
- ³³ K.S. Jones and E.E. Haller, *J. Appl. Phys.* **61**, 7 (1987).

- ³⁴ A. Satta, E. Simoen, T. Clarysse, T. Janssens, A. Benedetti, B. De Jaeger, M. Meuris, and W. Vandervorst, *Appl. Phys. Lett.* **87**, 172109 (2005).
- ³⁵ Y.-L. Chao, S. Prussin, J.C.S. Woo, and R. Scholz, *Appl. Phys. Lett.* **87**, 142102 (2005).
- ³⁶ Yong Seok Suh, M.S. Carroll, R.A. Levy, G. Bisognin, D. De Salvador, M.A. Sahiner, and C.A. King, *Electron Devices, IEEE Transactions On* **52**, 2416 (2005).
- ³⁷ G. Impellizzeri, S. Mirabella, E. Bruno, A.M. Piro, and M.G. Grimaldi, *J. Appl. Phys.* **105**, 063533 (2009).
- ³⁸ A. Satta, E. Simoen, T. Janssens, T. Clarysse, B.D. Jaeger, A. Benedetti, I. Hoflijk, B. Brijs, M. Meuris, and W. Vandervorst, *J. Electrochem. Soc.* **153**, G229 (2006).
- ³⁹ G. Bisognin, S. Vangelista, M. Berti, G. Impellizzeri, and M.G. Grimaldi, *J. Appl. Phys.* **107**, 103512 (2010).
- ⁴⁰ E. Simoen, A. Satta, A. D'Amore, T. Janssens, T. Clarysse, K. Martens, B. De Jaeger, A. Benedetti, I. Hoflijk, B. Brijs, M. Meuris, and W. Vandervorst, *Mater. Sci. Semicond. Process.* **9**, 634 (2006).
- ⁴¹ N. Ioannou, D. Skarlatos, C. Tsamis, C.A. Krontiras, S.N. Georga, A. Christofi, and D.S. McPhail, *Appl. Phys. Lett.* **93**, 101910 (2008).
- ⁴² A. Satta, A. D'Amore, E. Simoen, W. Anwand, W. Skorupa, T. Clarysse, B. Van Daele, and T. Janssens, *Nucl. Instrum. Methods Phys. Res. B* **257**, 157 (2007).
- ⁴³ V.I. Fistul, M.I. Iglitsyn, and E.M. Omel'yanovskii, *Sov. Phys. Sol. State* **4**, 784 (1962).
- ⁴⁴ O.A. Golikova, *Sov. Phys. Sol. State* **3**, 2259 (1962).
- ⁴⁵ E. Simoen, G. Brouwers, A. Satta, M.-L. David, F. Pailloux, B. Parmentier, T. Clarysse, J. Goossens, W. Vandervorst, and M. Meuris, *Mater. Sci. Semicond. Process* **11**, 368 (2008).
- ⁴⁶ G. Hellings, E. Rosseel, T. Clarysse, D.H. Petersen, O. Hansen, P.F. Nielsen, E. Simoen, G. Eneman, B. De Jaeger, T. Hoffmann, K. De Meyer, and W. Vandervorst, *Microelectron. Eng.* **88**, 347 (2011).
- ⁴⁷ N.S. Bennett and N.E.B. Cowern, *Appl. Phys. Lett.* **100**, 172106 (2012).
- ⁴⁸ E. Napolitani, G. Bisognin, E. Bruno, M. Mastromatteo, G.G. Scapellato, S. Boninelli, D. De Salvador, S. Mirabella, C. Spinella, A. Carnera, and F. Priolo, *Appl. Phys. Lett.* **96**, 201906 (2010).

- ⁴⁹ M.I. Guseva and A.N. Mansurova, *Rad. Effect.* **20**, 207 (1973).
- ⁵⁰ H. Bracht, S. Schneider, J.N. Klug, C.Y. Liao, J.L. Hansen, E.E. Haller, A.N. Larsen, D. Bougeard, M. Posselt, and C. Wündisch, *Phys. Rev. Lett.* **103**, 255501 (2009).
- ⁵¹ E. Bruno, S. Mirabella, G. Scapellato, G. Impellizzeri, A. Terrasi, F. Priolo, E. Napolitani, D. De Salvador, M. Mastromatteo, and A. Carnera, *Thin Solid Films* **518**, 2386 (2010).
- ⁵² G.G. Scapellato, E. Bruno, A.J. Smith, E. Napolitani, D. De Salvador, S. Mirabella, M. Mastromatteo, A. Carnera, R. Gwilliam, and F. Priolo, *Nucl. Instrum. Methods Phys. Res. B* **282**, 8 (2012).
- ⁵³ L.A. Edelman, K.S. Jones, R.G. Elliman, L.M. Rubin, E.G. Seebauer, S.B. Felch, A. Jain, and Y.V. Kondratenko, *AIP Conf. Proc.* **1066**, 225 (2008).
- ⁵⁴ G.G. Scapellato, S. Boninelli, E. Napolitani, E. Bruno, A.J. Smith, S. Mirabella, M. Mastromatteo, D. De Salvador, R. Gwilliam, C. Spinella, A. Carnera, and F. Priolo, *Phys. Rev. B* **84**, 024104 (2011).
- ⁵⁵ F.A. Trumbore, *J. Bell Syst. Tech.* **39**, 205 (1960).
- ⁵⁶ P.M. Fahey, P.B. Griffin, and J.D. Plummer, *Rev. Mod. Phys.* **61**, 289 (1989).
- ⁵⁷ N.E.B. Cower, G.F.A. van de Walle, P.C. Zalm, and D.W.E. Vandenhoudt, *Appl. Phys. Lett.* **65**, 2981 (1994).
- ⁵⁸ L. Pelaz, M. Jaraiz, G.H. Gilmer, H.-J. Gossmann, C.S. Rafferty, D.J. Eaglesham, and J.M. Poate, *Appl. Phys. Lett.* **70**, 2285 (1997).
- ⁵⁹ M.J. Caturla, M.D. Johnson, and T. Diaz de la Rubia, *Appl. Phys. Lett.* **72**, 2736 (1998).
- ⁶⁰ L. Pelaz, V.C. Venezia, H.-J. Gossmann, G.H. Gilmer, A.T. Fiory, C.S. Rafferty, M. Jaraiz, and J. Barbolla, *Appl. Phys. Lett.* **75**, 662 (1999).
- ⁶¹ P.A. Stolk, H.-J. Gossmann, D.J. Eaglesham, D.C. Jacobson, J.M. Poate, and H.S. Luftman, *Appl. Phys. Lett.* **66**, 568 (1995).
- ⁶² G. Mannino, N.E.B. Cower, F. Roozeboom, and J.G.M. van Berkum, *Appl. Phys. Lett.* **76**, 855 (2000).
- ⁶³ J.-Y. Jin, J. Liu, U. Jeong, S. Mehta, and K. Jones, *J. Vacuum Sci. Technol. B* **20**, 422 (2002).

- ⁶⁴ A.E. Michel, W. Rausch, P.A. Ronsheim, and R.H. Kastl, *Appl. Phys. Lett.* **50**, 416 (1987).
- ⁶⁵ M. Miyake and S. Aoyama, *J. Appl. Phys.* **63**, 1754 (1988).
- ⁶⁶ S. Solmi, F. Baruffaldi, and R. Canteri, *J. Appl. Phys.* **69**, 2135 (1991).
- ⁶⁷ N.E.B. Cower, K.T.F. Janssen, and H.F.F. Jos, *J. Appl. Phys.* **68**, 6191 (1990).
- ⁶⁸ P.A. Stolk, H.-J. Gossmann, D.J. Eaglesham, and J.M. Poate, *Nucl. Instrum. Methods Phys. Res. B* **96**, 187 (1995).
- ⁶⁹ L.H. Zhang, K.S. Jones, P.H. Chi, and D.S. Simons, *Appl. Phys. Lett.* **67**, 2025 (1995).
- ⁷⁰ P.A. Stolk, H.-J. Gossmann, D.J. Eaglesham, D.C. Jacobson, C.S. Rafferty, G.H. Gilmer, M. Jaraíz, J.M. Poate, H.S. Luftman, and T.E. Haynes, *J. Appl. Phys.* **81**, 6031 (1997).
- ⁷¹ P.A. Stolk, D.J. Eaglesham, H.-J. Gossmann, and J.M. Poate, *Appl. Phys. Lett.* **66**, 1370 (1995).
- ⁷² G. Impellizzeri, J.H.R. dos Santos, S. Mirabella, F. Priolo, E. Napolitani, and A. Carnera, *Appl. Phys. Lett.* **84**, 1862 (2004).
- ⁷³ G. Impellizzeri, S. Mirabella, F. Priolo, E. Napolitani, and A. Carnera, *J. Appl. Phys.* **99**, 103510 (2006).
- ⁷⁴ A.J. Smith, N.E.B. Cower, R. Gwilliam, B.J. Sealy, B. Colombeau, E.J.H. Collart, S. Gennaro, D. Giubertoni, M. Bersani, and M. Barozzi, *Appl. Phys. Lett.* **88**, 082112 (2006).
- ⁷⁵ R. Gwilliam, N.E.B. Cower, B. Colombeau, B. Sealy, and A.J. Smith, *Nucl. Instrum. Methods Phys. Res. B* **261**, 600 (2007).
- ⁷⁶ N.S. Bennett, N.E. Cower, S. Paul, W. Lerch, H. Kheyrandish, A.J. Smith, R. Gwilliam, and B.J. Sealy, in *Solid-State Device Research Conference, 2008. ESSDERC 2008. 38th European* (IEEE, 2008), pp. 290–293.
- ⁷⁷ N.E.B. Cower, A.J. Smith, N. Bennett, B.J. Sealy, R. Gwilliam, R.P. Webb, B. Colombeau, S. Paul, W. Lerch, and A. Pakfar, *Mater. Sci. Forum* **573-574**, 295 (2008).
- ⁷⁸ J.F. Ziegler, *Nucl. Instrum. Methods Phys. Res. B* **219-220**, 1027 (2004).
- ⁷⁹ J. Narayan and O.W. Holland, *J. Appl. Phys.* **56**, 2913 (1984).

- ⁸⁰ N. Misra, L. Xu, M.S. Rogers, S.H. Ko, and C.P. Grigoropoulos, *Phys. Stat. Sol. C* **5**, (2008).
- ⁸¹ M.D. Giles, *J. Electrochem. Soc.* **138**, 1160 (1991).
- ⁸² E.H. Hall, *Amer. J. of Math.* **2**, 287 (1879).
- ⁸³ L.J. van der Pauw, *Philips Res. Rep.* **13**, (1958).
- ⁸⁴ L.J. van der Pauw, *Philips Tech. Rev.* **20**, (1958).
- ⁸⁵ D.W. Koon, A.A. Bahl, and E.O. Duncan, *Rev. Sci. Instrum.* **60**, 275 (1989).
- ⁸⁶ D.W. Koon, *Rev. Sci. Instrum.* **60**, 271 (1989).
- ⁸⁷ D.W. Koon, *Rev. Sci. Instrum.* **61**, 2430 (1990).
- ⁸⁸ D.W. Koon and C.J. Knickerbocker, *Rev. Sci. Instrum.* **63**, 207 (1992).
- ⁸⁹ D.W. Koon and C.J. Knickerbocker, *Rev. Sci. Instrum.* **64**, 510 (1993).
- ⁹⁰ D.W. Koon and C.J. Knickerbocker, *Rev. Sci. Instrum.* **67**, 4282 (1996).
- ⁹¹ F. Szmulowicz, W. Mitchel, F.L. Madarasz, and P.M. Hemenger, *Measurement and Theory of the Hall Scattering Factor and the Conductivity Mobility in Ultra Pure P-Type Silicon at Low Temperatures* (Defense Technical Information Center, 1983).
- ⁹² R.S. Popovic, *Hall Effect Devices, Second Edition* (CRC Press, 2003).
- ⁹³ F.J. Morin, *Phys. Rev.* **93**, 62 (1954).
- ⁹⁴ F.J. Morin and J.P. Maita, *Phys. Rev.* **94**, 1525 (1954).
- ⁹⁵ O.A. Golikova, B.Y. Moizhez, and L.S. Stilbans, *Sov. Phys. Sol. State* **3**, (1962).
- ⁹⁶ J.E. Dijkstra and W.T. Wenckebach, *Appl. Phys. Lett.* **70**, 2428 (1997).
- ⁹⁷ "International Technology Roadmap for Semiconductors" (2011).
- ⁹⁸ G. Eneman, M. Wiot, A. Brugere, O.S.I. Casain, S. Sonde, D.P. Brunco, B. De Jaeger, A. Satta, G. Hellings, K. De Meyer, C. Claeys, M. Meuris, M.M. Heyns, and E. Simoen, *Electron Devices, IEEE Transactions On* **55**, 2287 (2008).
- ⁹⁹ G. Eneman, B. De Jaeger, E. Simoen, D.P. Brunco, G. Hellings, J. Mitard, K. De Meyer, M. Meuris, and M.M. Heyns, *Electron Devices, IEEE Transactions On* **56**, 3115 (2009).

- ¹⁰⁰ G. Eneman, O. Sicart i Casain, E. Simoen, D.P. Brunco, B. De Jaeger, A. Satta, G. Nicholas, C. Claeys, M. Meuris, and M.M. Heyns, in *Solid State Device Research Conference, 2007. ESSDERC 2007. 37th European* (2007), pp. 454–457.
- ¹⁰¹ G. Eneman, M.B. Gonzalez, G. Hellings, B.D. Jaeger, G. Wang, J. Mitard, K. DeMeyer, C. Claeys, M. Meuris, M. Heyns, T. Hoffmann, and E. Simoen, *ECS Trans.* **28**, 143 (2010).
- ¹⁰² T. Krishnamohan, Z. Krivokapic, K. Uchida, Y. Nishi, and K.C. Saraswat, *Electron Devices, IEEE Transactions On* **53**, 990 (2006).
- ¹⁰³ M.B. Gonzalez, G. Eneman, G. Wang, B.D. Jaeger, E. Simoen, and C. Claeys, *ECS Trans.* **34**, 725 (2011).
- ¹⁰⁴ C.L. Petersen, Rong Lin, D.H. Petersen, and P.F. Nielsen, in *IEEE International Conference on Advanced Thermal Processing of Semiconductors, RTP.* (2006), p. 153.
- ¹⁰⁵ C.L. Petersen, T.M. Hansen, P. Bøggild, A. Boisen, O. Hansen, T. Hassenkam, and F. Grey, *Sens. and Act. A* **96**, 53 (2002).
- ¹⁰⁶ D.H. Petersen, O. Hansen, T.M. Hansen, P.R.E. Petersen, and P. Bøggild, *Microelectron. Eng.* **85**, 1092 (2008).
- ¹⁰⁷ S. Thorsteinsson, F. Wang, D.H. Petersen, T.M. Hansen, D. Kjær, R. Lin, J.-Y. Kim, P.F. Nielsen, and O. Hansen, *Rev. Sci. Instrum.* **80**, 053902 (2009).
- ¹⁰⁸ D.H. Petersen, O. Hansen, R. Lin, P.F. Nielsen, T. Clarysse, J. Goossens, E. Rosseel, and W. Vandervorst, in *IEEE International Conference on Advanced Thermal Processing of Semiconductors, RTP.* (2008), p. 251.
- ¹⁰⁹ J.W. Edington, *Practical Electron Microscopy in Materials Science* (Techbooks, 1991).
- ¹¹⁰ D.B. Williams and C.B. Carter, *Transmission Electron Microscopy: A Textbook for Materials Science* (Springer, 2009).
- ¹¹¹ L. de Broglie, *Nature* **112**, (1923).
- ¹¹² B. Fultz and J. Howe, *Transmission Electron Microscopy and Diffractometry of Materials*, 3rd ed. (Springer, 2009).
- ¹¹³ P. Williams, *Ann. Rev. of Mater. Sci.* **15**, 517 (1985).

- ¹¹⁴ A. Benninghoven, F.G. Rudenauer, and H.W. Werner, *Secondary Ion Mass Spectrometry: Basic Concepts, Instrumental Aspects, Applications and Trends* (1987).
- ¹¹⁵ C.W. Magee and M.R. Frost, *J. of Mass Spectromet. Ion Process.* **143**, (1995).
- ¹¹⁶ R.P. Gittins, D.V. Morgan, and G. Dearnaley, *J. Phys. D* **5**, (1972).
- ¹¹⁷ P. Williams and J.E. Baker, *Appl. Phys. Lett.* **36**, 842 (1980).
- ¹¹⁸ P. Williams, J.E. Baker, J.A. Davies, and T.E. Jackman, *Nucl. Instrum. Methods Phys. Res. B* **191**, 318 (1981).
- ¹¹⁹ Y. Wang and M. Nastasi, editors, *Handbook of Modern Ion Beam Materials Analysis 2 Volume Set*, 2nd ed. (Cambridge University Press, 2010).
- ¹²⁰ C. Jeynes, Z.H. Jafri, R.P. Webb, A.C. Kimber, and M.J. Ashwin, *Surf. and Interface Anal.* **25**, 254 (1997).
- ¹²¹ B.L. Doyle and D.K. Brice, *Nucl. Instrum. Methods Phys. Res. B* **35**, 301 (1988).
- ¹²² V.E. Borisenko and S.G. Yudin, *Phys. Stat. Sol.* **101**, 123 (1987).
- ¹²³ Yu-Lin Chao and J.C.S. Woo, *Electron Devices, IEEE Transactions On* **54**, 2750 (2007).
- ¹²⁴ M.Y. Tsai and B.G. Streetman, *J. Appl. Phys.* **50**, 183 (1979).
- ¹²⁵ T. Clarysse, D. Vanhaeren, I. Hofliijk, and W. Vandervorst, *Mater. Sci. and Engineer. R* **47**, 123 (2004).
- ¹²⁶ T. Clarysse, J. Bogdanowicz, J. Goossens, A. Moussa, E. Rosseel, W. Vandervorst, D.H. Petersen, R. Lin, P.F. Nielsen, O. Hansen, G. Merklin, N.S. Bennett, and N.E.B. Cown, *Mater. Sci. and Engineer. B* **154-155**, 24 (2008).
- ¹²⁷ C. Claeys, J. Mitard, G. Eneman, M. Meuris, and E. Simoen, *Thin Solid Films* **518**, 2301 (2010).
- ¹²⁸ D.H. Petersen, O. Hansen, R. Lin, and P.F. Nielsen, *J. Appl. Phys.* **104**, 013710 (2008).
- ¹²⁹ G. Hellings, E. Rosseel, E. Simoen, D. Radisic, D.H. Petersen, O. Hansen, P.F. Nielsen, G. Zschatzsch, A. Nazir, T. Clarysse, W. Vandervorst, T.Y. Hoffmann, and K. De Meyer, *Electrochem. Solid-State Lett.* **14**, H39 (2011).
- ¹³⁰ R. Wittmann and S. Selberherr, *Solid-State Electronics* **51**, 982 (2007).

- ¹³¹ L. Romano, A.M. Piro, S. Mirabella, M.G. Grimaldi, and E. Rimini, *Appl. Phys. Lett.* **87**, 201905 (2005).
- ¹³² A.M. Piro, L. Romano, S. Mirabella, and M.G. Grimaldi, *Mater. Sci. and Eng. B* **124–125**, 249 (2005).
- ¹³³ L. Romano, A.M. Piro, M.G. Grimaldi, and E. Rimini, *Nucl. Instrum. Methods Phys. Res. B* **249**, 181 (2006).
- ¹³⁴ L. Romano, A.M. Piro, S. Mirabella, and M.G. Grimaldi, *Phys. Rev. B* **81**, 075210 (2010).
- ¹³⁵ R.J. Kaiser, S. Koffel, P. Pichler, A.J. Bauer, B. Amon, L. Frey, and H. Ryssel, *Microelectron. Engineer.* **88**, 499 (2011).
- ¹³⁶ A. Agarwal, H.-J. Gossmann, D.J. Eaglesham, L. Pelaz, D.C. Jacobson, J.M. Poate, and T.E. Haynes, *Mater. Sci. and Engineer. A* **253**, 269 (1998).
- ¹³⁷ F. Priolo, G. Mannino, M. Micciché, V. Privitera, E. Napolitani, and A. Carnera, *Appl. Phys. Lett.* **72**, 3011 (1998).
- ¹³⁸ B.R. Appleton, O.W. Holland, J. Narayan, O.E. Schow, J.S. Williams, K.T. Short, and E. Lawson, *Appl. Phys. Lett.* **41**, 711 (1982).
- ¹³⁹ O.W. Holland, B.R. Appleton, and J. Narayan, *J. Appl. Phys.* **54**, 2295 (1983).
- ¹⁴⁰ H. Huber, W. Assmann, S.A. Karamian, A. Mücklich, W. Prusseit, E. Gazis, R. Grötzschel, M. Kokkoris, E. Kossionidis, H.D. Mieskes, and R. Vlastou, *Nucl. Instrum. Methods Phys. Res. B* **122**, 542 (1997).
- ¹⁴¹ L. Romano, G. Impellizzeri, M.V. Tomasello, F. Giannazzo, C. Spinella, and M.G. Grimaldi, *J. Appl. Phys.* **107**, 084314 (2010).
- ¹⁴² B.R. Yates, B.L. Darby, R.G. Elliman, and K.S. Jones, *Appl. Phys. Lett.* **101**, 131907 (2012).
- ¹⁴³ G. Impellizzeri, L. Romano, B. Fraboni, E. Scavetta, F. Ruffino, C. Bongiorno, V. Privitera, and M.G. Grimaldi, *Nanotech.* **23**, 395604 (2012).
- ¹⁴⁴ B.L. Darby, B.R. Yates, N.G. Rudawski, K.S. Jones, and A. Kontos, *Nucl. Instrum. Methods Phys. Res. B* **269**, 20 (2011).
- ¹⁴⁵ C.O. Chui, K. Gopalakrishnan, P.B. Griffin, J.D. Plummer, and K.C. Saraswat, *Appl. Phys. Lett.* **83**, 3275 (2003).

- ¹⁴⁶ F. Panciera, P.F. Fazzini, M. Collet, J. Boucher, E. Bedel, and F. Cristiano, *Appl. Phys. Lett.* **97**, 012105 (2010).
- ¹⁴⁷ D.H. Petersen, O. Hansen, R. Lin, and P.F. Nielsen, *J. Appl. Phys.* **104**, 013710 (2008).
- ¹⁴⁸ D.H. Petersen, O. Hansen, T.M. Hansen, P. Boggild, R. Lin, D. Kjaer, P.F. Nielsen, T. Clarysse, W. Vandervorst, E. Rosseel, N.S. Bennett, and N.E.B. Cowern, *J. Vacuum Sci. Technol. B* **28**, C1C27 (2010).
- ¹⁴⁹ A.F. Saavedra, K.S. Jones, M.E. Law, K.K. Chan, and E.C. Jones, *J. Appl. Phys.* **96**, 1891 (2004).
- ¹⁵⁰ D.P. Hickey, Z.L. Bryan, K.S. Jones, R.G. Elliman, and E.E. Haller, *J. Vacuum Sci. Technol. B* **26**, 425 (2008).
- ¹⁵¹ A. Satta, T. Janssens, T. Clarysse, E. Simoen, M. Meuris, A. Benedetti, I. Hofliijk, B.D. Jaeger, C. Demeurisse, and W. Vandervorst, *J. Vacuum Sci. Technol. B* **24**, 494 (2006).
- ¹⁵² J. Oh and J.C. Campbell, *J. of Electron. Mater.* **33**, 364 (2004).
- ¹⁵³ A. Chroneos, *J. Appl. Phys.* **105**, 056101 (2009).
- ¹⁵⁴ Fei Wang, D.H. Petersen, F.W. Osterberg, and O. Hansen, in *Advanced Thermal Processing of Semiconductors, 2009. RTP '09. 17th International Conference On* (2009), pp. 1–6.
- ¹⁵⁵ S. Mirabella, E. Bruno, F. Priolo, D. De Salvador, E. Napolitani, A.V. Drigo, and A. Carnera, *Appl. Phys. Lett.* **83**, 680 (2003).
- ¹⁵⁶ F. Cristiano, X. Hebras, N. Cherkashin, A. Claverie, W. Lerch, and S. Paul, *Appl. Phys. Lett.* **83**, 5407 (2003).
- ¹⁵⁷ S. Boninelli, S. Mirabella, E. Bruno, F. Priolo, F. Cristiano, A. Claverie, D. De Salvador, G. Bisognin, and E. Napolitani, *Appl. Phys. Lett.* **91**, 031905 (2007).
- ¹⁵⁸ M. Ngamo, S. Duguay, F. Cristiano, K. Daoud-Ketata, and P. Pareige, *J. Appl. Phys.* **105**, 104904 (2009).
- ¹⁵⁹ P. López, L. Pelaz, I. Santos, L.A. Marqués, and M. Aboy, *J. Appl. Phys.* **111**, 033519 (2012).
- ¹⁶⁰ M.-J. Caturla, T. Díaz de la Rubia, L.A. Marqués, and G.H. Gilmer, *Phys. Rev. B* **54**, 16683 (1996).
- ¹⁶¹ P. Delugas and V. Fiorentini, *Phys. Rev. B* **69**, 085203 (2004).

- ¹⁶² K. Sueoka and J. Vanhellemont, *Mater. Sci. Semicond. Process.* **9**, 494 (2006).
- ¹⁶³ J. Vanhellemont, P. Śpiwak, and K. Sueoka, *J. Appl. Phys.* **101**, 036103 (2007).
- ¹⁶⁴ A. Giese, N.A. Stolwijk, and H. Bracht, *Appl. Phys. Lett.* **77**, 642 (2000).
- ¹⁶⁵ J. Vanhellemont and E. Simoen, *J. Electrochem. Soc.* **154**, H572 (2007).
- ¹⁶⁶ M. Werner, H. Mehrer, and H.D. Hochheimer, *Phys. Rev. B* **32**, 3930 (1985).
- ¹⁶⁷ H.D. Fuchs, W. Walukiewicz, E.E. Haller, W. Dondl, R. Schorer, G. Abstreiter, A.I. Rudnev, A.V. Tikhomirov, and V.I. Ozhogin, *Phys. Rev. B* **51**, 16817 (1995).
- ¹⁶⁸ E. Silveira, W. Dondl, G. Abstreiter, and E.E. Haller, *Phys. Rev. B* **56**, 2062 (1997).
- ¹⁶⁹ P. Lopez, Personal Communication, University of Valladolid, 2012.
- ¹⁷⁰ D.F. Downey, J.W. Chow, E. Ishida, and K.S. Jones, *Appl. Phys. Lett.* **73**, 1263 (1998).
- ¹⁷¹ P.W. Loscutoff and S.F. Bent, *Ann. Rev. of Phys. Chem.* **57**, 467 (2006).
- ¹⁷² D.P. Hickey, Z.L. Bryan, K.S. Jones, R.G. Elliman, and E.E. Haller, *Appl. Phys. Lett.* **90**, 132114 (2007).
- ¹⁷³ G. Bisognin, S. Vangelista, and E. Bruno, *Mater. Sci. and Eng. B* **154–155**, 64 (2008).
- ¹⁷⁴ S. Koffel, N. Cherkashin, F. Houdellier, M.J. Hytch, G. Benassayag, P. Scheiblin, and A. Claverie, *J. Appl. Phys.* **105**, 126110 (2009).
- ¹⁷⁵ F. Panciera, P.F. Fazzini, M. Collet, J. Boucher, E. Bedel, and F. *Appl. Phys. Lett.* **97**, 012105 (2010).
- ¹⁷⁶ R. Crosby, K.S. Jones, M.E. Law, A.N. Larsen, and J.L. Hansen, *J. Vacuum Sci. Technol. B* **22**, 468 (2004).
- ¹⁷⁷ C.A. Ferreira Lima and A. Howie, *Phil. Mag.* **34**, 1057 (1976).
- ¹⁷⁸ S. Furuno, K. Izui, and H. Otsu, *Japanese J. Appl. Phys.* **15**, 889 (1976).
- ¹⁷⁹ M. Pasemann, D. Hoehl, A.L. Aseev, and O.P. Pchelyakov, *Phys. Stat. Sol. A* **80**, 135 (1983).

- ¹⁸⁰ A.L. Aseev, V.M. Ivakhnishin, V.F. Stas, and L.S. Smirnov, *Sov. Phys. Sol. State* **25**, 1786 (1983).
- ¹⁸¹ H. Bartsch, D. Hoehl, and G. Kästner, *Phys. Stat. Sol. A* **83**, 543 (1984).
- ¹⁸² J.L. Hutchinson, A.L. Aseev, and L.I. Fedina, in *Microscopy of Semiconducting Materials* (1993), pp. 41–46.
- ¹⁸³ T. Akatsu, K.K. Bourdelle, C. Richtarch, B. Faure, and F. Letertre, *Appl. Phys. Lett.* **86**, 181910 (2005).
- ¹⁸⁴ S. Rubanov and P.R. Munroe, *Micron* **35**, 549 (2004).
- ¹⁸⁵ C.A. Schneider, W.S. Rasband, and K.W. Eliceiri, *Nat.Meth.* **9**, 671 (2012).
- ¹⁸⁶ S. Boninelli, G. Impellizzeri, A. Alberti, F. Priolo, F. Cristiano, and C. Spinella, *Appl. Phys. Lett.* **101**, (2012).
- ¹⁸⁷ F.F. Morehead and B.L. Crowder, *Rad. Effect.* **6**, 27 (1970).
- ¹⁸⁸ L.A. Christel, J.F. Gibbons, and T.W. Sigmon, *J. Appl. Phys.* **52**, 7143 (1981).
- ¹⁸⁹ R.G. Elliman, J.S. Williams, W.L. Brown, A. Leiberich, D.M. Maher, and R.V. Knoell, *Nucl. Instrum. Methods Phys. Res. B* **19–20, Part 2**, 435 (1987).
- ¹⁹⁰ R.G. Elliman, S.T. Johnson, A.P. Pogany, and J.S. Williams, *Nucl. Instrum. Methods Phys. Res. B* **7–8, Part 1**, 310 (1985).
- ¹⁹¹ D. Sigurd, G. Fladda, L. Eriksson, and K. Björkqvist, *Rad. Effect.* **3**, 145 (1970).
- ¹⁹² G. Holmén, S. Peterström, A. Burén, and E. Bøgh, *Rad. Effect.* **24**, 45 (1975).
- ¹⁹³ J. Linnros and G. Holmén, *J. Appl. Phys.* **62**, 4737 (1987).

BIOGRAPHICAL SKETCH

Bradley Robert Yates is the son of Charlene Leyda and James Yates. He was born in Pittsburgh, Pennsylvania. He was raised in a small town located about an hour south of Pittsburgh called Belle Vernon. He attended Belle Vernon Area High School where he played football and graduated in June 2004. He attended Carnegie Mellon University in Pittsburgh, Pennsylvania where he double-majored in Materials Science and Biomedical Engineering in addition to playing defensive end for the Tartans for two years. His professional football hopes were dashed by concussion issues which steered him to attend graduate school following the culmination of his undergraduate career in May 2008. He attended the University of Florida in Gainesville, Florida in August 2008 where he began working for Dr. Kevin Jones on the work discussed herein in addition to work on Group IV anode materials for lithium ion batteries, the formation of nanoporous Ge, and electroless etching of silicon among other side projects. Upon completion of his Ph. D. degree, he will be joining Intel in Hillsboro, Oregon as an engineer within Portland Technology Development. In the future, he plans to retire young and purchase a large, fuel efficient boat to cruise around the Caribbean Sea.